Tracing galaxy evolution through resolved stellar populations and star clusters

ISBN 978 90 393 5611 1

Printed by Wöhrmann Print Service, Zutphen

Cover image: Second Palomar Sky Survey images of NGC 4395 combined using Aladin software.

Cover designed by Juan Agüera.

Tracing galaxy evolution through resolved stellar populations and star clusters

De reconstructie van de evolutie van sterrenstelsels met behulp van opgeloste sterpopulaties en sterrenhopen

(met een samenvatting in het Nederlands)

Proefschrift

ter verkrijging van de graad van doctor aan de Universiteit Utrecht op gezag van de rector magnificus, prof. dr. G. J. van der Zwaan, ingevolge het besluit van het college voor promoties in het openbaar te verdedigen op vrijdag 2 september 2011 des ochtends te 10.30 uur

door

Esteban Silva Villa

geboren op 3 april 1979 te Medellín, Colombia

Promotor: Prof. dr. C. U. Keller

Co-promotor: Dr. S. S. Larsen

No es cierto que la gente deje de perseguir sus sueños porque envejece,
se hacen viejos porque dejan de perseguirlos.

– Gabriel García Márquez

Dedicated to my family.

Contents

Astronomy is the supreme example of the observational, as opposed to experimental, sciences in which the wit of the observer has to be pitted against the difficulties, and in particular the ambiguities, imposed by the need to interpret remotely sensed data.

Craig & Brown (1986)

Chapter 1

Introduction

1.1. General overview

Galaxies are islands in the universe, said Alexander von Humboldt in his book *Kosmos*. Among the millions that exist, the Greek mythology called our own the Milky Way[1]. Humanity has been always interested in that particular and constant appearance that can be observed easily with naked eyes in a clear night. But it was not until Galileo pointed his telescope to the sky that we started to study it in more detail.

The structure of the Milky Way is often probed through the study of the distribution of the stars and the star clusters. Pioneer observations began with Messier, Herschel, Shapley, who are just some in a long list of astronomers that devoted their studies to understand our galaxy. We can now confidently say that the Milky Way is a barred spiral galaxy, with the sun located at roughly $\sim$ 8 Kpc from its center[2], inbetween the Sagittarius and Perseus arms. It is a rather normal galaxy, but being inside of it allows us to have a better understanding of its structure. However, this same location inside the disc of the Milky Way limits our studies, and because of that we perform studies of external galaxies, trying to get a more general overview of the process of galaxy formation and evolution.

In order to understand the processes of formation and evolution of a galaxy, and its particular shape (e.g. spiral, elliptical, etc), the study of its parts at present times is the only indication of the past activity. It is then our task to take the parts and employ them to trace back in time the processes that shaped a galaxy. The two main components of a galaxy are the stars and the gas[3]. In the early 50's, observations of OB stars in the Sagittarius arm by Morgan et al. (1953) suggested that in the arms of spiral galaxies the star formation activity was higher than in the inter arm regions

[1] The word *Milky Way* comes from ancient Greek history, and refers to the river of milk flowing from the breast of Hera, the wife of Zeus.

[2] 1 kiloparsec is equal to 3.09×10^{16} kilometers.

[3] Dark matter is the other key component of a galaxy, however we do not attempt to discuss any implication related with dark matter in any sense over this thesis.

(see also e.g. Kaltcheva 2009). Spiral arms, as observed in the Milky Way, thus contain a wealth of information regarding the process of the formation of stars across the galaxies. In the same manner, the spatial distribution of star clusters have been used in the past to study the structure of our galaxy. For example, Shapley (1916, and references therein) noted that young star clusters (known also as open clusters) were concentrated in the disc of the Milky Way, while their old counter part (known also as globular clusters) were distributed in the halo. Shapley also noted that open clusters were less massive than the globular clusters. The importance (or insightful) information regarding galaxy evolution is thus encoded in the observations of the stellar components.

Due to the observational constrains in the study of stars in the Milky Way (e.g. large amount of extinction in the direction of the galactic center), it became of major importance to study resolved stellar populations in external galaxies. Moreover, the use of resolved stellar populations to estimate the star formation histories of galaxies has shown to be a powerful tool to understand galaxy formation and evolution in the local and nearby universe (see e.g. Dohm-Palmer et al. (1997) for Sextant A, Harris & Zaritsky (2001) for Large Magellanic Cloud -LMC-, among many others). The main problem of this method will be the observational constrains experienced when increasing the distance to the target galaxy. The use of resolved stellar populations (and their formation history) can be achieve only up to few megaparsec with the existing instruments. But the information retrieved from the resolved stellar populations would not be complete without the knowledge we have on the evolution of individual stars, so we have to rely on the use of different stellar evolutionary models (e.g. Padova models, Marigo et al. 2008). Regardless of the large amount of uncertainties (observational and theoretical), the use of stars at different stages of their evolution has been largely proved to be an important tool to the study the evolution of galaxies (see Gallart et al. 2005, for a review).

A direct link between the stars and the gas was first indentified by Schmidt (1959). He assumed that the star formation rate is related to the gas volume density across a galaxy, following a power-law distribution with an index of ~ 2. This relation observed by Schmidt was further studied and corroborated by Kennicutt (1998) using surface densities of the same two parameters. Kennicutt found that there is in fact a power-law relation between the surface star formation rate density and the surface gas density ($\Sigma_{SFR} \propto \Sigma_{gas}^{\alpha}$), with an index $\alpha \sim 1.4$. Today we know this relation as the "Schmidt-Kennicutt law" (SK law). This powerful relation connects two main parameters of a galaxy, although only at large scale (~kiloparsecs). However, the relation at smaller scales (~parsecs) does not apply (see e.g. Elmegreen 2011b, for a further discussion), and new studies are needed to understand the processes at these small scales.

As important as it is, the SK law cannot explain the physical appearance of a galaxy. Since the late 1960's, theoretical predictions were able to reproduce the arms of spiral galaxies, a theory known today as the density wave theory (DWT, Lin & Shu 1964, Roberts 1969). The observational study of the physical structure of the galaxies is not trivial, and new observational studies are still needed to understand

the process of galaxy formation. With that in mind, it is clear that understanding the relations between the arms of a galaxy (in the case of spirals), their gas and their stellar population is of key importance. Recent simulations of morphologically different galaxies started to indicate the spatial location of star clusters at different ages during galaxy evolution (e.g. Dobbs & Pringle 2010). On the observational side, predictions from the DWT have been studied by Martínez-García et al. (2009), who observed the variation of the color gradient in the arms of a sample of 13 spiral galaxies, finding good agreement between observations and theory.

In general, the studies related to the SK law and the DWT are based on the distribution of the different gas components (e.g. HI, HII, CO, etc) and the distribution of the stars (mainly through the studies of their integrated light). This is solely due to the limitations of the observations (such as distance, extinction, inclinations along the line of sight, etc), which constrain the study of resolved populations. In the last two decades, new telescopes and instruments have become available (e.g. Hubble Space Telescope -HST-, Very Large Telescope -VLT-, and the respective instruments), allowing us to get direct measurements of resolved stellar populations in different galaxies (i.e. in their different environments) for distances not reached before (up to few Mpc). Nevertheless, only few authors have pursued studies based on resolved stellar populations in the local and nearby universe.

In nearby galaxies, the study of UV, Hα and B-band luminosities has shown that most of the light comes from the young star clusters (Meurer et al. 1995, Zepf et al. 1999, Fall et al. 2005). Also, It has been widely assumed that most of the stars are formed in clusters (e.g. Lada & Lada 2003, Porras et al. 2003). For these reasons, star clusters are viewed as ideal objects to trace the star formation histories of distant galaxies where resolved stars are below the detection limits. However, the low cluster formation efficiency (e.g. Gieles & Bastian 2008, Gieles 2010, Goddard et al. 2010, Adamo et al. 2011, Silva-Villa & Larsen 2011), the discrepancy among results from different models of cluster disruption (e.g. Lamers et al. 2005, Whitmore 2007) and the apparent lack of different modes of star formation (i.e. field stars vs. clusters, Bressert et al. 2010) are challenging our common ideas regarding the fraction of stars actually formed in clusters. Due to dynamical and stellar evolution clusters disrupt (Spitzer 1987), enriching the field population of galaxies. However, many questions remain open about the process of clusters formation and disruption. What fraction of clusters is disrupted at very early stages ($\leq$ few megayears)? Which processes guide the disruption? What fraction of star formation is happening in clusters and what fraction of the clusters remains bound for a long time? Many studies tried to answer to all these questions (e.g. Larsen & Richtler 2000, Boutloukos & Lamers 2003, Fall et al. 2005, Whitmore 2007, Bastian 2008, Gieles 2010, Bressert et al. 2010, for some recent work). Moreover, if we assumed that star clusters can trace (major) episodes of star formation, a relation between star clusters and field stars must be seen across galaxies, where environmental dependences must play a crucial factor (see e.g. Larsen et al. 2007, Kruijssen & Lamers 2008, Silva-Villa & Larsen 2011, for examples of studies that connect star formation histories with cluster formation histories).

Different authors during the last decade suggested that there is a direct connection

between the (number of) star clusters and its parent galaxy (e.g. Larsen & Richtler 2000, Bastian 2008). The relation found indicates that the amount of light in young clusters is directly connected with the star formation rate (Larsen & Richtler 2000). Bastian (2008) used the relation between the most luminous cluster and the star formation rate to derive the cluster formation efficiency (CFE). However, neither of the previous studies have made a direct comparison between the cluster formation and star formation rates. Moreover, these authors have based their results on information retrieved from integrated light observations. Measurements of the CFE are not a straightforward task and, in general, are affected by different assumptions, such as constant internal extinction in the target galaxies. Different attempts to measure the CFE have been done in the past years (e.g. Meurer et al. 1995, Bastian 2008, Gieles 2010, Goddard et al. 2010, Adamo et al. 2011, Silva-Villa & Larsen 2011) over morphologically different galaxies. In the nominal work by Lada & Lada (2003), the authors studied embedded star clusters in the Milky Way and found that a large fraction of stars (∼90%) is born there, but due to dynamical processes clusters disrupt in few megayears. The studies by Meurer et al. (1995) showed that the fraction (∼20%) of the blue and ultraviolet light in starburst galaxies comes from the star clusters. Meurer et al. concluded that a large fraction of star formation is actually happening in the clusters. Following this idea, Bastian (2008) estimated that the fraction of star formation happening in (bound) clusters is close to 8%. However, recent results on the young stellar objects in the solar neighborhood done by Bressert et al. (2010) could not find differences in the modes of star formation (i.e. field vs. cluster formation). Also, Goddard et al. (2010) using a heterogeneous set of morphologically different galaxies suggested a relation between the CFE and the Σ_{SFR}. The power law relation found by Goddard et al. has been tested by other authors, reaching different results (e.g. Gieles 2010, Adamo et al. 2011, Silva-Villa & Larsen 2011). However, the estimates of the CFEs are affected by many uncertainties. To measure CFE a complete sample of cluster is needed. Nevertheless, a large number of clusters are disrupted at very early stages due to gas expulsion (phase also known as "infant mortality", which is defined in different age ranges depending on the models assumed). In addition, a number of clusters is bellow our detection limits. Assuming a constant cluster formation rate (CFR) it is expected to observe a homogeneous distribution of clusters at different ages and masses. However, observations do not show this. Degeneracies (e.g. age-metallicity degeneracy) affect our estimations, and in many cases, ages and masses are over- (or under-) estimated, altering the position of the clusters over the parameter space. It is important to account for the problems that are affecting these estimates of the CFE and take care of the interpretations of the values obtained.

In our search for a better understanding of galaxy formation and evolution, it becomes of uttermost importance to use the information held by the resolved populations of stars and the star clusters of a particular galaxy, making them the special tools that will guide us to unveil the different phenomena observed in spiral galaxies.

1.2. The tools

1.2.1. Field stars

As an observational science, astronomy relies on the information retrieved from every single photon that arrives to our detector (either ground or space based). As a theoretical science, astronomy relies on physics to explain how the stars (or galaxies) produce light in the way we observe.

Galaxies are composed of a very large number of stars with different masses and ages, at different stages of their evolution. These parameters combined with their spatial distribution, either inside clusters or belonging to the field population, are close related with their parent galaxy. The relevance of these objects to understand galaxy formation and evolution becomes clear, as stars are holding information regarding past events.

Observational astrophysics uses photometry as a tool to convert the collected light that arrives to a detector (from a star or any object) into magnitudes. Through the use of different wavelengths over the electromagnetic spectrum, astronomers can asses specific properties of the stars and the gas. For example, stars have different colors at different stages of their evolution (i.e. a relation with mass and age); if a region in a galaxy is experiencing recent (or active) star formation, there will be enhanced emission in Hα (i.e. a relation with temperature and age). The observed characteristics of the stars are then interpreted as physical stages of their evolution and astronomers use this knowledge to study stellar populations (see bottom panel of Fig. 1.1 for different phases of stellar evolution). All these processes can be observed and linked with different physical phases of their parent galaxy (i.e. different events of star formation across time). Knowing this, astronomers created stellar evolutionary models that can predict relations among different properties of a star. Figure 1.1 presents a relation between the luminosity and the effective temperature of stars at different ages (upper left panel). In practice, these two properties can be observed combining different bands. In the same figure (upper right panel) the magnitudes V and I are use to determine the positions that stars will have assuming different ages. This diagram is known as the color-magnitude diagram (CMD). To trace galaxy evolution through the use of the resolved stellar populations, it is of paramount importance to understand the different phases across the CMDs. If we assume a constant star formation rate during the entire evolution of a galaxy, stars on the main sequence can be found at all epochs. The main sequence turn-off point (MSTO), where the stars leave the main sequence, can be used to estimate ages of populations that formed at the same epoch (e.g. star clusters are assumed to form at roughly the same time), sub-giant and horizontal branches and red clumps can indicate particular epochs of star formation due to the different ages that are represented by these stars (see lower panel in Fig. 1.1), allowing us to use them to trace back the history of a galaxy. A full review on how stellar models can be used to trace and interpret the resolved stellar populations can be found in Gallart et al. (2005). However, astronomical observations are limited by different factors, such as distance,

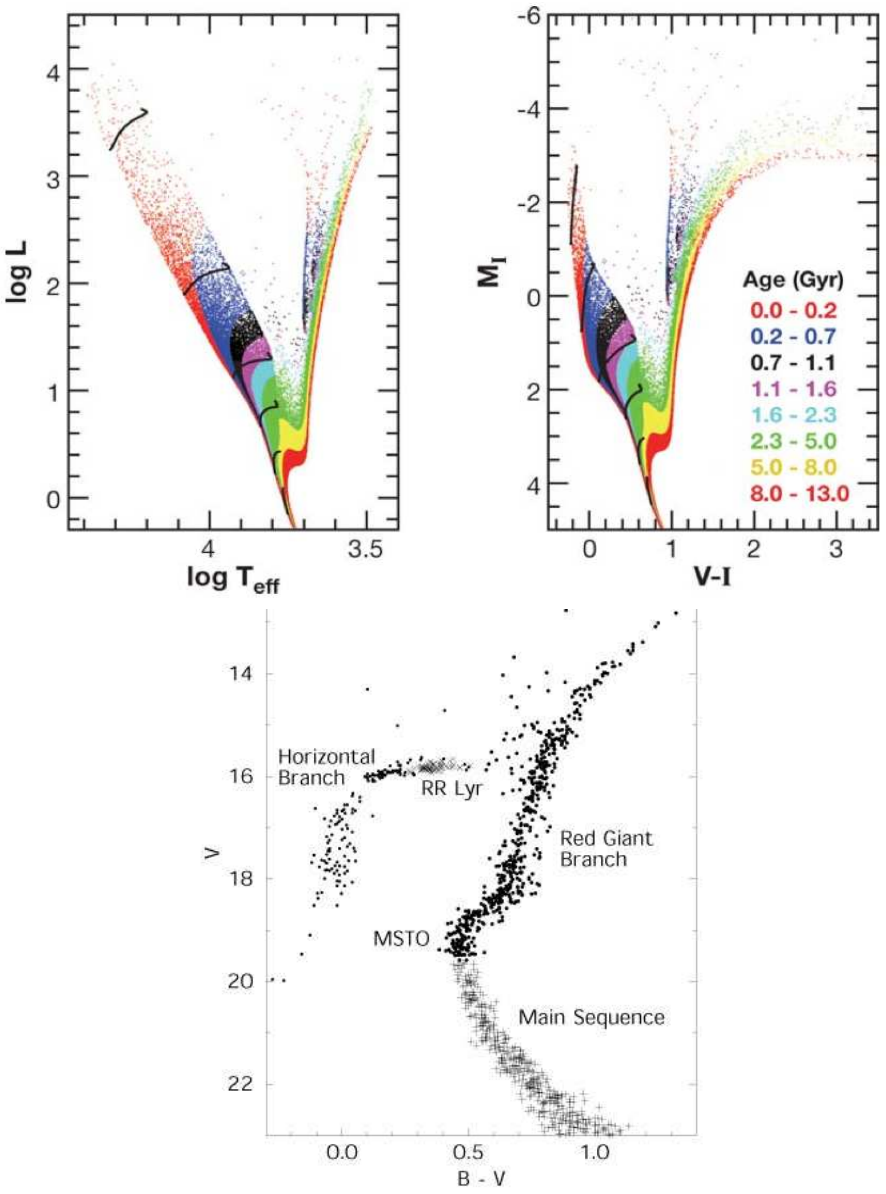

Figure 1.1: *Upper panels*: Color-magnitude diagrams for a synthetic population. Different colors represent different ages for the stars. Image taken from Gallart et al. (2005). *Lower panel*: Color-magnitude diagram indicating different phases of the star's life, image taken from Carroll & Ostlie (2006).

extinction due to gas and dust, power resolution of the instruments, etc.

Trying to alleviate the constrains imposed by the observations, Tosi et al. (1991) developed a new method known as the synthetic CMD method. The Tosi et al. method takes into account all the observational uncertainties mentioned above and tries to create a theoretical CMD, using stellar evolutionary models (e.g. Padova 2008 isochrones, Marigo et al. 2008) and theoretical assumptions regarding parameters like the stellar initial mass function, the binary fraction, metallicity, etc. The main goal of this method is to reconstruct the star formation history of a galaxy, through the direct comparison of the theoretical CMD with the observed one. The synthetic CMD method has been implemented by different authors and for different galaxies: Brown et al. (2008, M31), Harris & Zaritsky (2004, LMC), Harris & Zaritsky (2009, SMC), and Larsen et al. (2007, NGC 1313). Throughout this thesis, the synthetic CMD method is implemented using an IDL-based code created to obtain the star formation histories of various galaxies. Although there are programs available online that perform the same task (Dolphin 1997, Harris & Zaritsky 2001, see Skillman & Gallart (2002) for a review and test of different codes), we noted that there is not a preferred one in the literature, and creating our own program allowed us to use, modify and optimize the variables to our needs.

1.2.2. Star clusters

Star clusters are associations of stars that are gravitationally bound. These stars were formed from a giant molecular cloud roughly at the same time and with the same chemical composition (i.e. the one from the mother-cloud). Because clusters can shine proportionally more than individual stars, they play a major role when used to characterize star formation histories at far distances (farther than few tends of megaparsec), where individual stars can not longer be resolved.

Stellar evolution, dynamics and environment act over the life time of a cluster. These three phenomena are able to destroy a star cluster, releasing the stars to the field of the galaxy (e.g. Spitzer 1987, Lamers et al. 2005, Fall et al. 2005, Gieles et al. 2006, Whitmore 2007, Elmegreen & Hunter 2010, Kruijssen et al. 2011). If we assumed that most stars are formed in clusters (e.g. Lada & Lada 2003), it becomes important to understand the disruption processes during cluster evolution. A natural question will arises: How well cluster formation history can trace star formation histories?

The first step is to understand how the clusters are disrupted. The main tool to estimate cluster disruption has been through the use of the age distribution of a cluster system in an individual galaxy ($dN/d\tau$, number of clusters per age interval). The mass distributions are commonly used as well. The age distribution is indicative of the amount of clusters that are being disrupted in age intervals, where it is generally assumed a constant cluster formation rate. Two main models are nowadays use to understand the age distributions of clusters (i.e. the cluster disruption scenarios), being both fundamentally different in their assumptions. These two models are referred as a *mass independent disruption* and a *mass dependent disruption* model. Figure 1.2 illustrates how these two models (mass independent in the left column, mass

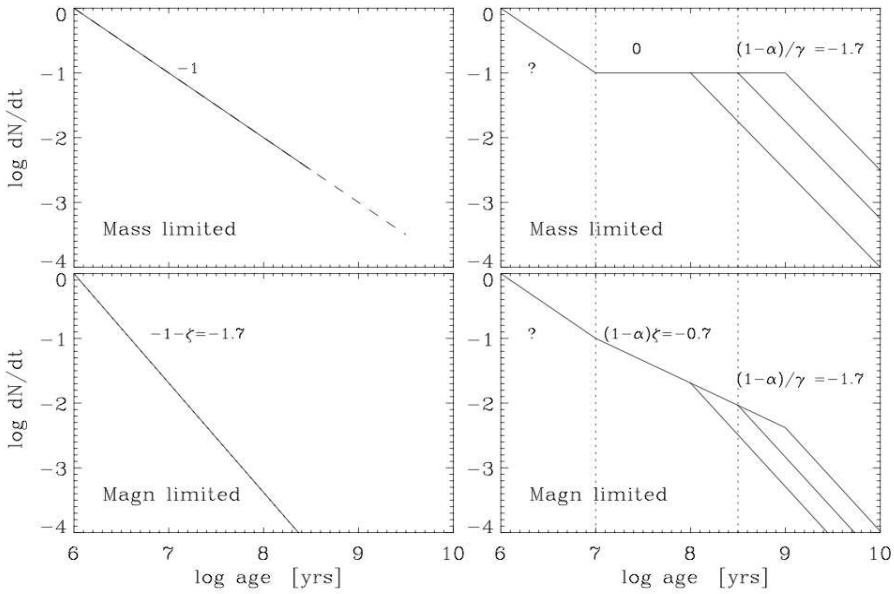

Figure 1.2: Age distributions for MID and MDD models (left and right columns respectively) for a mass and magnitude limit sample. Image taken from Lamers (2009). See text for a short explanation of the variables α, ζ and γ.

dependent in the right column) are interpreting the age distributions of a cluster system. The variables α, ζ and γ over the different time ranges seen in the figure represent three indices: the index of the cluster initial mass function (generally assumed to be -2 in a power-law relation), the index of evolutionary fading due to stellar evolution with time ($F_\lambda(\tau) \propto \tau^{-\zeta}$, where λ represents the wavelength and $F_\lambda(\tau)$ its respective flux at time τ), and the index of a mass dependent dissolution model (only applies for the mass dependent model), respectively. For a further explanation see Boutloukos & Lamers (2003), Fall et al. (2005), Lamers et al. (2005), Whitmore (2007), Lamers (2009).

- *Mass Dependent Disruption model* (MDD)
  Originally described by Boutloukos & Lamers (2003) (further improved by Lamers et al. 2005), this model uses a magnitude or mass limited sample of star clusters to understand how age and mass distributions change with time. Two main regimes where identified by Boutloukos & Lamers: one that is (mainly) dominated by the stellar evolution, showing a decrease in the age distribution due to fading; and one which combines the fading with the disruption cause by environment, creating a more steep decrease on the number of clusters. On its very basis, this method follows a law that dissolves clusters on a time scale depending on their (initial) mass: $t_{dis} = t_4 \times (M/10^4 M_\odot)^\gamma$, where t_4 is the

disruption time for a cluster with initial mass of 10^4 $M_\odot$.

- *Mass Independent Disruption model* (MID)
  Originally described by Fall et al. (2005) (further improved by Whitmore 2007), this model was created to explain the observed age distributions of clusters in the Antennae galaxy. The observed age distribution of this galaxy follow a power-law with an index -1. The interpretation of this index suggests that the Antennae system is disrupting 90% of clusters per dex in age, being a mass and environmentally independent process. Further studies in the solar neighborhood and other galaxies like SMC and M83 have suggested similar results (Chandar et al. 2006, Whitmore 2007, Chandar et al. 2010).

For a more detailed description of these two models, we refer the reader to Lamers (2009, and references therein).

Most of the debate related with the MDD and MID is based on differences observed in the sample of clusters used to study the age distributions. As we will show in Chapter 3, selection effects and incomplete samples are a *large* source of uncertainties (see also e.g. Fouesneau & Lançon 2010, Konstantopoulos et al. 2010). As an example, Mora et al. (2007, 2009) found steeper slopes in the age distributions when compare with the results observed by Silva-Villa & Larsen (2011), although both studies used the same data. Nevertheless, neither Mora et al., nor Silva-Villa & Larsen could make any conclusions regarding these two models based on the observations. But not only selection effects and incomplete samples are affecting the results. Anders et al. (2004) show that it is necessary to have at least four-band photometry to be able to break degeneracies (e.g. age-metallicity). Also, estimations of cluster parameters based on observations are affected by stochastic effects. Different observational and theoretical studies showed that the random sampling of the stellar initial mass function can severely compromise the results for low mass clusers ($\leq 10^4 M_\odot$, e.g. Maíz Apellániz 2009, Popescu & Hanson 2010b, Fouesneau & Lançon 2010, Silva-Villa & Larsen 2011). For high mass clusters ($\geq 10^5 M_\odot$) this problem decreases. Using Monte Carlo simulations, Maíz Apellániz (2009) showed how stochastic effects are influencing the determination of cluster ages and masses, which are derived from broadband photometry. Piskunov et al. (2009) show how different considerations of the stellar initial mass function can explain features observed in the color-age relation. Silva-Villa & Larsen (2011) created artificial clusters and added them to science images of different galaxies and observed how young star clusters ($\leq$10 Myr) can be missed when automatic selection criteria are implemented to observe unresolved star clusters.

Theoretical approaches are starting to give light on the discussion between MDD and MID (e.g. Elmegreen & Hunter 2010, Kruijssen et al. 2011), while on the observational side many challenges remain unresolved.

1.3. Outline of this thesis

Based on *Hubble Space Telescope* (HST) observations, we present a study of the five nearby, face-on spiral galaxies: NGC 45, NGC 1313, NGC 4395, NGC 5236, and NGC 7793, depicted in Fig. 1.3. The parameters for the set of galaxies is presented in table 3.1.

Throughout this thesis, we will see how resolved stellar populations contain a lot of the information on the galaxy evolution. The stellar population is complemented with the unresolved star clusters, showing the power of these two systems when used as a tool to understand and trace back the formation of a galaxy.

Here we summarize the content of the following chapters:

- ***In chapter 2***: With the idea in mind that star clusters and resolved stellar populations can provide insightful information about galaxy formation and evolution, we devoted this chapter to create and test our programs to estimate the necessary parameters for our studies. We tested our programs over the galaxy NGC 4395, which showed to have a low cluster and star formation rate compare to studies made by Gieles (2010) over M51, M74, and M101, but similar values to the SMC, as studied by Gieles & Bastian (2008).

- ***In chapter 3***: To understand cluster formation efficiencies, we used in this chapter a sample of five nearby, face-on, spiral galaxies, where we estimated star and cluster formation histories for each galaxy, having then a homogeneous sample. We compared our results with estimates of Goddard et al. (2010), who suggested a power-law relation between the cluster formation efficiency and the surface star formation rate density of morphologically different galaxies. The results showed to be smaller in comparison with the suggested power-law.

- ***In chapter 4***: The structure of the grand-design galaxy M83 is studied, trying to understand the processes in the arms and in the inter-arm regions in spiral galaxies. Through the use of the resolved stellar population in this galaxy, we estimated surface star formation rate densities at different locations in the galaxy, and found that inside the arms the star formation present higher values compare to the inter arm regions. Inside the observational limits, we observed the distribution of the surface star formation rate across a fraction of one of the arms of the galaxy, trying to test predictions from the DWT.

- ***In chapter 5***: Resolved stellar populations hold insightful information of past processes in the evolution of a galaxy. We studied the galaxy NGC 1313, which is classified as a Magellanic-like galaxy, regardless of the observed barred spiral morphology. We found evidence for a recent interaction between this galaxy and a satellite disrupted companion in the south-west region. The use of the resolved stellar populations showed to be an important tool to study such kind of process.

Figure 1.3: The sample. *NGC 45 upper left*: Credits James R. Foster, *NGC 1313 upper right*: Credits Henri Boffin, *NGC 4395 middle left*: Credits Bob Franke, *NGC 5236 middle right*: Credits Robert Glender, and *NGC 7793 bottom*: Credits European Souther Observatory (ESO).

1.4. Outlook

Throughout this thesis we have approached to different aspects of galaxy evolution. These studies have used one of the main components of a galaxy, its stars. We base our analysis on the observations of resolved stellar populations combining them with star cluster systems.

Many questions regarding how to deal with the stochastic effects induced by the sampling of the stellar initial mass function when estimating cluster masses and ages remain unanswered. These two parameters are of key importance if we aim a full understanding of the evolution of galaxies. To keep using star clusters as tools to trace galaxy evolution, the problems arising from the stochastic effects induced by the stellar initial mass function must be accounted for. Also, state-of-art theoretical models are not including any treatment on binary evolution, and predictions of the spectral energy distributions are compromised, so a reliable comparison is limited, and it should be interpreted with caution.

It is important to note that previous studies are based on samples of clusters that have shown to be affected by selection criteria, incompleteness and stochastic effects, and we are not an exception. We tried a new approach in our studies, where we showed how important is to understand the automatic selection of clusters (i.e. based on programs like SExtractor or Daofind), which in turn increases the possibility to obtain a better estimation of the age and mass distribution of a cluster system. The stochastic effects are influencing the age and mass estimates of star clusters, particularly at young ages ($\leq 10^8$yr) and low masses ($\leq 10^4 M_\odot$). These two ranges for ages and masses are essential in extragalactic works. Visual inspections over the clusters detected are just a first approach to clean the sample, although it is not a solution to the problem.

During the past years we have been following the idea that most stars are being formed in clusters. It is not clear if this idea still holds. A direct comparison between cluster and star surface formation rates over 5 different galaxies have shown that cluster formation efficiencies are below 10%. However, age distributions estimated (using a mass limited sample) over different galaxies suggests that the fraction of clusters being disrupted reaches average values of 60%. If this large number of clusters are being disrupted, then a large fraction of stars are then release to the field of a galaxy. Nevertheless, more observations of a large sample of clusters, reaching lower masses, are necessary.

On a broader view of galaxy evolution, we used the resolved stellar population to analyze different aspects. On one hand, the observations were compared with the density wave theory and its predictions, regarding the increase of the star formation in the arms, compared to the inter-arm regions. On the other hand, we observed an increase in the star formation history possibly due to an interaction between two galaxies.

The use of resolved stellar populations and star clusters has been shown to be a powerful tool to understand different galaxies, and to observe a variety of different phenomena that are occurring among different spiral galaxies in the local universe. With these results in mind, the necessity of new observations becomes clear, i.e. stellar populations are holding insightful information of galaxy formation and evolution, and studying closer galaxies can reveal more details on hidden processes.

The limits of the possible can only be defined by going beyond them into the impossible.
–Arthur C. Clarke

Chapter 2

The star cluster - field star connection in nearby spiral galaxies. I. Data analysis techniques and application to NGC 4395

E. Silva-Villa & S. S. Larsen
Published in *Astronomy & Astrophysics*, 516, A10 (2010)[1]

Abstract

It is generally assumed that a large fraction of stars are initially born in clusters. However, a large fraction of these disrupt on short timescales and the stars end up belonging to the field. Understanding this process is of paramount importance if we wish to constrain the star formation histories of external galaxies using star clusters. We attempt to understand the relation between field stars and star clusters by simultaneously studying both in a number of nearby galaxies. As a pilot study, we present results for the late-type spiral NGC 4395 using HST/ACS and HST/WFPC2 images. Different detection criteria were used to distinguish point sources (star candidates) and extended objects (star cluster candidates). Using a synthetic CMD method, we estimated the star formation history. Using simple stellar population model fitting, we calculated the mass and age of the cluster candidates. The field star formation rate appears to have been roughly constant, or to have possibly increased by up to about a factor of two, for ages younger than ~300 Myr within the fields covered by our data. Our data do not allow us to constrain the star formation histories at older ages. We identify a small number of clusters in both fields. Neither massive ($> 10^5$ $M_\odot$) clusters nor clusters with ages ≥ 1 Gyr were found in the galaxy and we found few clusters older than 100 Myr. Based on our direct comparison of field stars and clusters in NGC 4395, we estimate the ratio of star formation rate in clusters that survive for 10^7 to 10^8 years to the total star formation to be $\Gamma \sim 0.03$. We suggest that this relatively low Γ value is caused by the low star formation rate of NGC 4395.

[1]Reproduced with permission © ESO

2.1. Introduction

It is commonly assumed that most (if not all) stars are formed in clusters. Clusters, due to dynamical and stellar evolution, dissolve (Spitzer 1987) and the stars that belong to them become part of the field stellar population of the galaxy. To use clusters as effective tools to constrain the formation and evolution of galaxies, it is necessary to improve our understanding of what fraction of stars end up as members of bound clusters and in the field, respectively.

Both field stars and star clusters have been studied extensively in the Milky Way and nearby galaxies. In principle, field stars hold information about star formation histories over the entire Hubble time and can therefore provide important information about galaxy formation and evolution, e.g., Edvardsson et al. (1993). Main sequence stars are present at all ages, and observations of the main sequence turn-off can constrain epochs of stellar formation especially in dwarf galaxies where relatively distinct bursts are often observed (Mateo 1998). Other features of the color-magnitude diagram (CMD), such as the sub-giant and horizontal branches, giant and asymptotic branches, red clump stars, and red and blue supergiants can provide information about specific epochs of star formation. However, it is necessary to apply a more sophisticated modeling of the CMD to reconstruct star formation histories, taking into account different effects, e.g., incompleteness, resolution, depth of the observations, extinction and chemical composition. Tosi et al. (1991) developed a method that takes these effects into account and attempts to use all the information available in a CMD to reconstruct the field star formation history of a galaxy. The synthetic CMD method creates a synthetic population that is compared to the observed CMD to constrain the star formation history (SFH) of the field stars in a galaxy. Many subsequent studies have refined this method (Dolphin 1997, Harris & Zaritsky 2001, Skillman & Gallart 2002). The SFHs of many galaxies in the Local Group and nearby have been studied using the synthetic CMD method: Brown et al. (2008) for M31, Harris & Zaritsky (2009) for the LMC, Harris & Zaritsky (2004) for the SMC, Barker et al. (2007) for the M33, Cole et al. (2007) for Leo A, Young et al. (2007) for Phoenix, Annibali et al. (2009) for NGC 1705, Williams et al. (2009) for M81, Larsen et al. (2007) for NGC1313 and Rejkuba et al. (2004) for NGC 5128, among many others.

On the other hand, the study of cluster systems and disruption processes can provide important insight into the origin of field stars in a galaxy. Clusters disrupt by means of a variety of mechanisms, including "infant mortality", stellar evolution, two-body relaxation, and tidal shocks that have been extensively studied by Boutloukos & Lamers (2003), Lada & Lada (2003), Lamers et al. (2005), Baumgardt (2009), Fall (2006), Elmegreen (2008), Whitmore (2007), and Bastian & Gieles (2008) among others. The analysis of star clusters is often based on a comparison between the observed spectral energy distribution and theoretical models, which provides information about the ages and masses of the studied clusters and, in turn, their dissolution. However, the comparison of models with observations also remains affected by many uncertainties, e.g., binarity, completeness effects.

Some studies have started to address the relation between field stars and clusters

more explicitly. The number of stars that were formed in clusters has been estimated to be 70% – 90% in the solar neighbourhood, while 50% – 95% of these embedded clusters dissolve in a few Myrs (Lada & Lada 2003, Lamers & Gieles 2008). Gieles & Bastian (2008) estimated that only 2-4% of the global star formation rate in the SMC happened in bound star clusters. It is currently unknown what fraction of stars are initially born in clusters in SMC, but if this fraction were as large as in the Solar neighbourhood this would imply that there is also a large infant mortality rate in the SMC. Bastian (2008) studied the relation between the cluster formation rate and the star formation rate ($\Gamma = \frac{CFR}{SFR}$) using archival Hubble images for high star formation rate galaxies and additional galaxies/clusters from literature. He found this fraction to be $\Gamma \sim 0.08$ and thus concluded that the fraction of stars formed in (bound) clusters represents 8% of the total star formation. On the other hand, Gieles (2010) found that Γ is given by $0.05 \leq \Gamma \leq 0.18$ in the galaxies M74, M101, and M51. In most of these cases, however, it is difficult to tell whether there is a genuine "field" mode of cluster formation, or whether *all* stars form initially in clusters of which a large fraction dissolves rapidly.

We aim to analyze the relation between field stars and star clusters in different environments and address the question of whether or not there is a constant cluster formation "efficiency". To this end, we use *Hubble Space Telescope* (HST) images of a set of five galaxies (NGC 4395, NGC 1313, NGC 45, NGC 5236, and NGC 7793), which are nearby, face-on, spirals that differ in their morphologies, star, and cluster formation histories. The cluster systems of these galaxies were studied by Mora et al. (2009) using the same Hubble images analyzed in this work. Mora et al. observed significant variations in the cluster age distributions of these galaxies. The galaxies are sufficiently nearby (~ 4 Mpc) for the brighter field stars to be well resolved in HST images, so that (recent) field star formation histories can be constrained by means of the synthetic CMD method. We can therefore take advantage of the superb spatial resolution of HST images to study field stars and clusters simultaneously within specific regions of these galaxies.

As a pilot work, this paper is devoted to presenting and testing all the analysis procedures, such as detection of stars and cluster candidates, completeness tests and photometry, and derivation of field star and cluster age distributions. We discuss our implementation of the synthetic CMD method as an IDL program and carry out tests of this program. To test our procedures we use the galaxy NGC 4395. The methods described in this paper will be used in our study of the rest of the galaxy sample (see Silva-Villa & Larsen 2011, or chapter 3).

This article has the following structure. In Sect. 2.2, we provide general information about NGC 4395. We present the observations, data reduction, and photometry, where we differentiate the point sources (star candidates) from the extended objects (cluster candidates) in Sects. 2.3 and 2.4. Section 2.5 is devoted to the analysis of the star and cluster properties. Finally, in Sect. 2.6 we present the discussion and conclusions.

Table 2.1: Journal of HST/ACS and HST/WFPC2 observations for both fields (F1 and F2) in NGC 4395.

Proposal ID	Date	Filter	Total exp. time (s)
NGC 4395 (J2000.0) $\alpha : 12^h26^m00^s$ $\delta : +33^o31'04''$			
9774	2004 Jun 12	F435W (B)	680
9774	2004 Jun 12	F555W (V)	680
9774	2004 Jun12	F814W (I)	430
NGC 4395 (J2000.0) $\alpha : 12^h26^m00^s.50$ $\delta : +33^o30'58''.3$			
9774	2004 Jun 12	F336W (U)	2400
NGC 4395 (J2000.0) $\alpha : 12^h25^m45^s.20$ $\delta : +33^o34'28''$			
9774	2004 Jun 18	F435W (B)	680
9774	2004 Jun 18	F555W (V)	680
9774	2004 Jun 18	F814W (I)	430
NGC 4395 (J2000.0) $\alpha : 12^h25^m42^s.72$ $\delta : +33^o34'22''.6$			
9774	2004 Jun 18	F336W (U)	2400

2.2. NGC 4395

According to the NASA/IPAC Extragalactic Database (NED), NGC 4395 is a late-type spiral classified as type SA(s)m. It harbours the closest and least luminous known example of a Seyfert 1 nucleus (Filippenko & Sargent 1989). Following Larsen & Richtler (1999), we adopt a distance modulus of $(m - M) = 28.1$ ($D \approx 4.2$ Mpc) and an absolute magnitude $M_B = -17.47$, intermediate between the Small and Large Magellanic Cloud. We assume a Galactic foreground extinction for NGC 4395 of $A_B = 0.074$ (Schlegel et al. 1998).

The cluster system of NGC 4395 was first studied by Larsen & Richtler (1999), using ground-based imaging. Using multiband ($UBVRIH\alpha$) photometry, Larsen & Richtler identified 2 young clusters in this galaxy, although their observations were limited to objects with $M_V \leq -8.5$. In their work, NGC 4395 is part of a sample of 21 galaxies. Compared to the remaining sample, NGC 4395 exhibits an exceptionally small number of star clusters and a low specific luminosity (ratio of cluster- to total galaxy light; Larsen & Richtler 2000). Using HST images, Mora et al. (2009) could detect clusters based on their sizes and found a total of 44 clusters in NGC 4395 to a magnitude limit of $M_B = -3.3$. Compared to the other 4 galaxies in their sample, Mora et al. reached the same conclusions as Larsen & Richtler, i.e., NGC 4395 has a small number of star clusters. Mora et al. estimated the ages and masses of the clusters detected, showing that the star cluster system contains no objects with ages older than 10^9 yr and includes clusters with masses ranging from 200 to $\sim 3 \times 10^4$ $M_\odot$.

Until now, no study of resolved field stars has been performed in this galaxy. However, Larsen & Richtler (2000) found that NGC 4395 has one of the lowest area-normalised star formation rates of all objects in their sample.

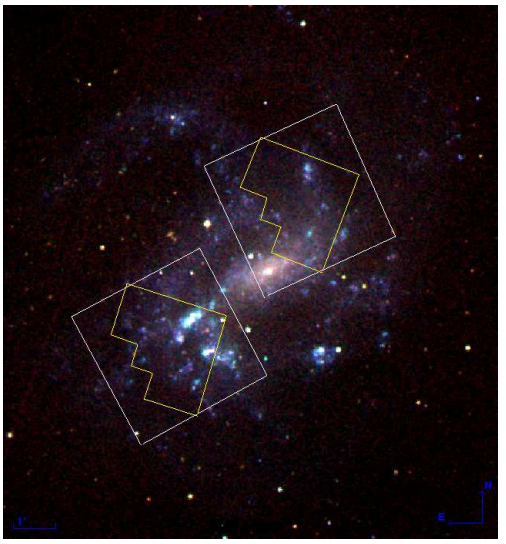

Figure 2.1: Second Palomar Sky Survey images of NGC 4395 combined using Aladin software. HST/ACS (white lines) and HST/WFPC2 (yellow lines) fields covered by our observations are indicated.

2.3. Observation and data reduction

Images of NGC 4395 were taken using the Wide Field Channel on the *Advanced Camera for Surveys* (ACS/WFC) and the *Wide Field Planetary Camera 2* (WFPC2), both on board the *Hubble Space Telescope* (HST). The resolution of the detectors are 0″05, 0″046, and 0″1 per pixel for ACS/WFC, WFPC2/PC, and WFPC2/WF, respectively. At the distance of NGC 4395, 0″05 corresponds to a linear scale of ∼ 1 pc.

Two different fields of the galaxy were observed, covering the two spiral arms (see Fig. 2.1). The images were taken using the filters F336W (∼ U) using WFPC2 and F435W (∼ B), F555W (∼ V) and F814W (∼ I) using ACS, for each field. Each exposure was divided into two sub-exposures to eliminate cosmic-ray hits. For the ACS images, these sub-exposures were also dithered to allow removal of cosmetic defects. Table 2.1 summarizes the observations.

The data were processed with the standard STScI pipeline. The raw ACS images were drizzled using the *multidrizzle* task (Koekemoer et al. 2002) in the STSDAS package of IRAF[2]. The default parameters were used, but automatic sky subtraction was disabled. The WFPC2 images were combined and corrected for cosmic rays using the *crrej* task with the default parameters.

[2]IRAF is distributed by the National Optical Astronomical Observatory (NOAO), which is operated by the Association of Universities for Research in Astronomy, Inc, under cooperative agreement with the National Science Foundation

2.3.1. Object detection

At the distance of NGC 4395, the spatial resolution of the HST images allows us to distinguish field stars (point sources with typical $FWHM \sim 2$ pixels) and star clusters (extended sources with typically $FWHM \sim 3$ pixels or greater) in the images. We analyzed the two separately and applied different detection criteria optimised for each type of object:

- *Field star candidates (point sources)*
  To detect field stars, we created an averaged image (using the bands B, V, and I) for each field. We ran the *daofind* task in IRAF for the detection of stars using a 4σ detection threshold and a background standard deviation of ~ 0.02 in units of counts per second.

- *Star cluster candidates (extended sources)*
  Cluster detection was also performed on the averaged image. The object detection was performed using SExtractor V2.5.0 (Bertin & Arnouts 1996). The parameters used as input for this program were 6 connected pixels, all of them with 10σ over the background, to remove point- and spurious sources as much as possible. From the output file of SExtractor, we kept the coordinates of the objects detected and the FWHM calculated by this program. The coordinates found with SExtractor were then passed to *ishape* in BAOLab (Larsen 1999). *Ishape* models star clusters as analytical King (1962) profiles (with concentration parameter $t_{tidal}/r_{core} = 30$) and takes the instrument's PSF, created over the average image during the photometry, into account (see Sect. 2.4 for details on the creation of the PSF). By minimization of a χ^2-like function, *ishape* calculates the best-fit cluster coordinates, size, i.e., FWHM, signal-to-noise ratio, and the χ^2 of the best fit. From the output of *ishape* we saved the coordinate of the objects, the FWHM, the χ^2 of the fit, and the signal-to-noise ratio (calculated within the fitting radius of 4 pixels).

  For each WFPC2 chip, between five and seven common stars were visually selected and used to convert the coordinate list from ACS to WFPC2 frames using the task *geomap* in IRAF. The transformations had an *rms* of ~ 0.15 pixels.

2.4. Photometry

The photometry of NGC 4395 was performed following standard aperture and PSF fitting photometry procedures as described in the following.

2.4.1. Field stars

Because of the crowding in our fields, we performed PSF fitting photometry to study the field stars. A set of bona fide stars were selected by eye to construct the PSF (for each band a different group of stars were used because the same stars might

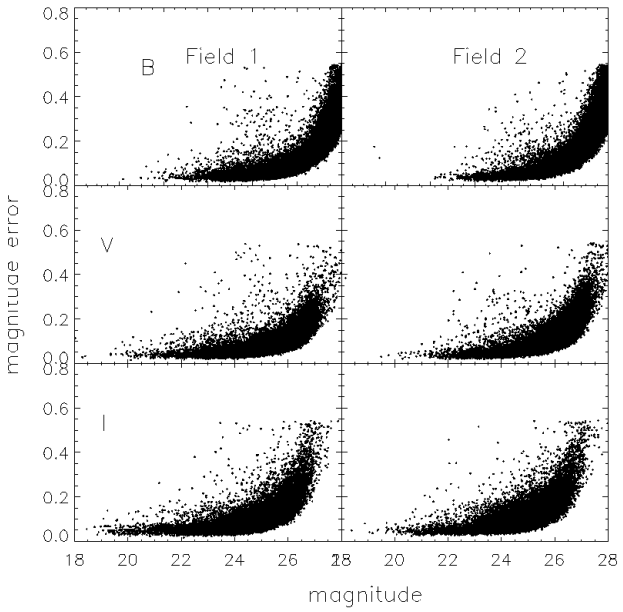

Figure 2.2: Magnitude errors for the stars detected using PSF fitting photometry over the two fields for the bands B, V, and I

have different brightnesses in different bands). The PSF photometry was performed with DAOPHOT in IRAF. We selected the PSF stars by measuring the FWHM (using *imexamine*) and selecting point sources smaller than $FWHM \approx 2.2$ pixels. As far as possible, we tried to include isolated stars distributed over the whole image.

The raw magnitudes were converted to the Vega magnitude system using the HST zero-points taken from HST webpages[3] after applying aperture corrections to a nominal 0″5 aperture (see Sect. 2.4.4 for a more detailed description of how aperture corrections were determined). The zero-points used were $ZP_B = 25.767$, $ZP_V = 25.727$, and $ZP_I = 25.520$ magnitudes.

Figure 2.2 shows the errors in our PSF photometry (1σ error) versus magnitude. The errors increase strongly below magnitudes of ~ 26 in each band, corresponding to absolute limits of ~ -2 mag at the distance of NGC 4395.

A total of ∼30 000 stars were found in each field. A combined Hess diagram for both fields is shown in Fig. 2.3 (a Hess diagram plots the relative frequency of stars at different color-magnitude positions). Various phases of stellar evolution can be recognised in the Hess diagram:

1. Main sequence and possible blue He-core burning stars at $V - I \sim 0$ and $-2 \leq$

[3] http://www.stsci.edu/hst/acs/analysis/zeropoints/#tablestart

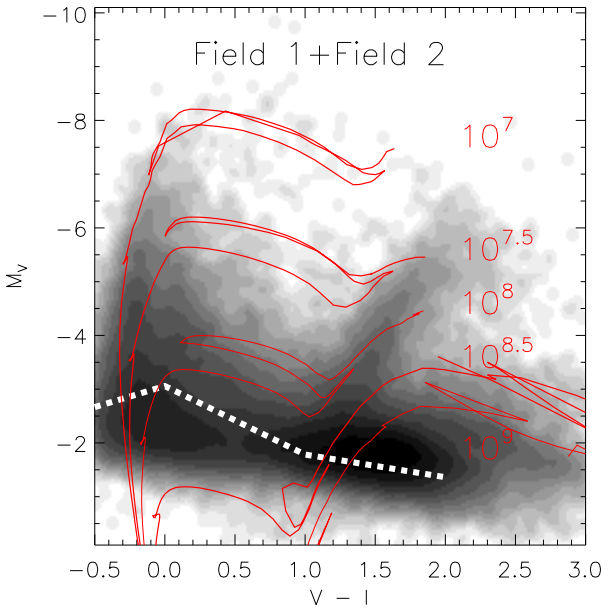

Figure 2.3: Hess diagram for the field stars in both fields. The dashed white line represents the 50% completeness for the first field. Red lines are Padova 2008 theoretical isochrones for the ages 10^7,$10^{7.5}$,10^8,$10^{8.5}$, and 10^9 yr using LMC metallicity.

$V \leq -8$;

2. Red He core burning stars at $1.2 \leq V - I \leq 2.5$ and $-2.5 \leq V \leq -6.5$;
3. RGB/AGB stars at $1 \leq V - I \leq 3$ and $-0.5 \leq V \leq -2.5$.

Overplotted in Fig. 3.2 are theoretical isochrones from the Padova group (Marigo et al. 2008) for five different ages using metallicity $Z = 0.008$ (red lines). The O abundance of HII regions in NGC 4395 was measured by Roy et al. (1996) to be $12 + \log O/H = 8.33 \pm 0.25$, or about 1/3 solar (Grevesse & Sauval 1998), suggesting an overall metallicity similar to that of the LMC. This is consistent with our analysis in Sect. 2.5, which shows that isochrones of LMC metallicity reproduce our data more closely. The white line indicates the 50% completeness limit (see Sect. 2.4.3).

2.4.2. Star clusters

Our detection criteria is met by 16 463 objects, i.e., 6 connected pixels with 10σ above the local background level. For the clusters, we carried out aperture photometry. An aperture radius of 6 pixels was used for the ACS images. At the distance of

NGC 4395, 1 ACS/WFC pixel corresponds to $\sim$ 1 pc, hence the chosen source aperture contains about 2 half-light radii for a typical star cluster. Our sky annulus had an inner radius of 8 pixels and a width of 5 pixels. For the WFPC2 images, apertures covering the same area were used (source aperture = 3 pixel radius, sky annulus = 4 pixel inner radius and 2.5 pixels width).

Of the 16 463 objects detected with SExtractor/*ishape*, a total of 4 472 candidates have measured four band photometry.

ACS magnitudes were converted to vega magnitude system using the same tables as for the field stars. WFPC2 magnitudes were converted to the Vega magnitude system using the zero-points taken from the webpages[4] of HST. Charge transfer efficiency (CTE) corrections were applied following the equations from Dolphin (2000)[5].

To select star cluster candidates, we used 3 criteria:

- Size:
  We measured the sizes of the objects. Figure 2.4 shows the FWHM distributions for SExtractor and *ishape*. The SExtractor histogram peaks at $\sim$ 2.2 pixels, corresponding to the stellar PSF. The *ishape* histogram peaks at 0 pixels, as *ishape* takes the PSF directly into account. Based on the FWHM distributions, we decided to use a criteria of $FWHM_{SExtractor} \geq 2.7$ pixels and $FWHM_{ishape} \geq 0.7$ pixels as a first selection of extended sources. These two limits correspond to a physical cluster half-light radius of $\sim$ 1 pc or greater at the distance of NGC 4395. Many of the candidate clusters we detect are low-mass and have irregular profiles often dominated by a few stars, so we chose to rely on both SExtractor and Ishape size measurements to achieve a more robust rejection of unresolved sources.

- Magnitude:
  Mora et al. (2009) ran a completeness analysis of artificial star clusters of different FWHMs in five nearby galaxies, including NGC 4395. The results presented in their work establish a 50% limit between $25 \leq m_B \leq 26$ magnitudes for objects with $FWHM$ = [0.1(point sources), 1.8] (see Mora et al. (2007, 2009) and Sect. 2.4.3 for more details).

  By performing four band photometry, we set a magnitude cut-off at $m_V \leq 23$, which represents objects brighter than $M_V \sim -5$ at the distance of the galaxy. This limit is brighter than that found by Mora et al. (2007) by $\sim$ 2 magnitudes.

  The main difference between the selection criteria of Mora et al. (2007) and this work is in the size limits of *ishape*, of half of a pixel (Mora et al. used $FWHM_{ishape} \geq 0.2$), hence we expect our data not to be significantly affected by incompleteness to our magnitude cutoff. However, even at our limit of $M_V = -5$, there is a risk that a few stars may dominate the light originating in

[4] www.stsci.edu/instruments/wfpc2/Wfpc2_ch52#1933986

[5] Last update May 12,2008:
http://purcell.as.arizona.edu/wfpc2_calib/

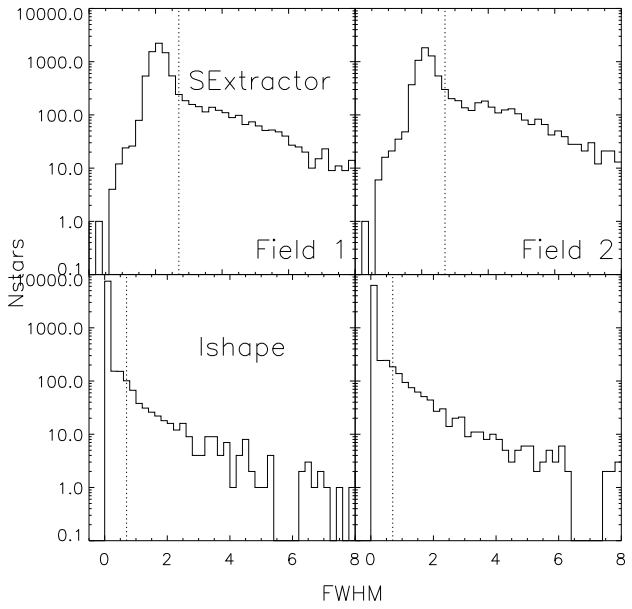

Figure 2.4: Histograms of the FWHM of the objects detected with SExtractor (top panel) and *ishape* (bottom panel). The vertical dotted lines represent the limits used to select the extended objects ($FWHM_{SExtractor} \geq 2.7$ and $FWHM_{ishape} \geq 0.7$ pixels)

a cluster, making it difficult to differentiate a real cluster from a couple of stars that, by chance, could be in the same line of sight.

- Color:
  Without taking into account any significant reddening, all clusters, including globulars, will have colors bluer than $V - I \sim 1.5$, e.g., Forbes et al. (1997), Larsen et al. (2001). We therefore make a color cut at $V - I = 1.5$.

We wish to emphasise that there is probably no unique combination of criteria that will lead to the detection of all bona-fide clusters in the image and at the same time produce no false detections. At low masses and young ages in particular, the light profiles may be dominated by individual bright stars. Out of 4 472 candidate objects, a total of 22 objects fulfill the three criteria stated above and will be considerate in the remain of this study to be star clusters. These 22 clusters were visually inspected in our images to determine whether they resemble a cluster. An example of the clusters detected is presented in Fig. 2.5. We investigated the large number of rejected objects and found that they were rejected for many reasons: (1) the area covered by the two detectors differs by a factor of ~ 2; (2) many of the objects are too faint in the U band; (3) the magnitude cut-off removes many objects, e.g., from a total of 4 475 detected

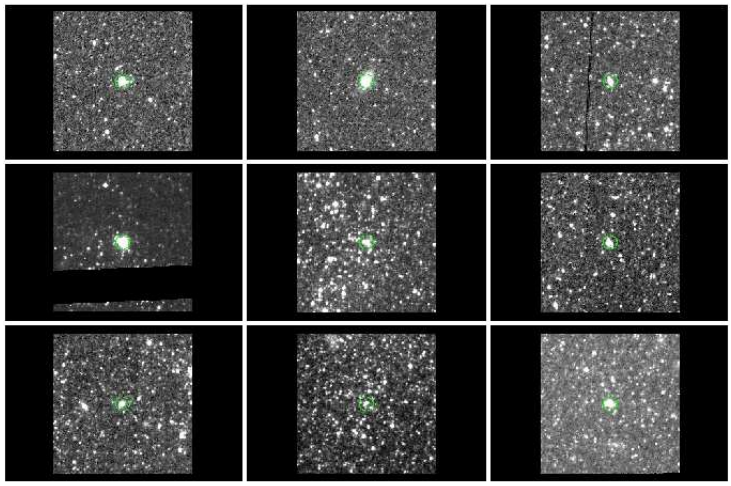

Figure 2.5: Example stamps of the clusters that satisfy the criteria stated in this work. Each cluster image has a dimension of 100×100 pixels ($\sim 100 \times 100$ pc).

objects, only 1 351 satisfy the magnitude limit, leading to the loss of $\sim 70\%$ detections; and (4) a large fraction of the objects have FWHMs smaller than our limits.

For the extended objects, a two-color diagram, based on the photometry in all of the available 4 passbands, is presented in Fig. 2.6. Clusters in both fields are depicted with their respective photometric errors and corrected for foreground extinction ($A_B = 0.074$). Using GALEV models (Anders & Fritze-v. Alvensleben 2003), Padova isochrones (Bertelli et al. 1994), a Salpeter's IMF (Salpeter 1955), and LMC (dashed line) or solar (dash-dotted line) metallicities, we overplotted the track that a cluster follows from ages between $6.6 \leq Log(\tau) \leq 10.2$ yr (each $\Delta \log(\tau) = 0.5$ dex age in log units being indicated). We observe considerable scatter in the two-color diagram. For these relatively low-mass clusters, the discreteness of the initial mass function will be important and might contribute significantly to the scatter (Girardi et al. 1995, Cerviño & Luridiana 2006, Maíz Apellániz 2009). A more detailed study of stochastic effects will be presented in a forthcoming paper (Silva-Villa et al. 2010, in prep.) This scatter was previously observed by Mora et al. (2009) (see their Fig. 6). Considering this scatter, it is clear that ages derived by a comparing observed and model colors should be treated with some caution.

2.4.3. Completeness test

To determine the completeness limits of our field-star photometry, we generated synthetic images with artificial stars. From 20 to 28 magnitudes, in steps of 0.5 mag, five images per step were created and analyzed with exactly the same parameters

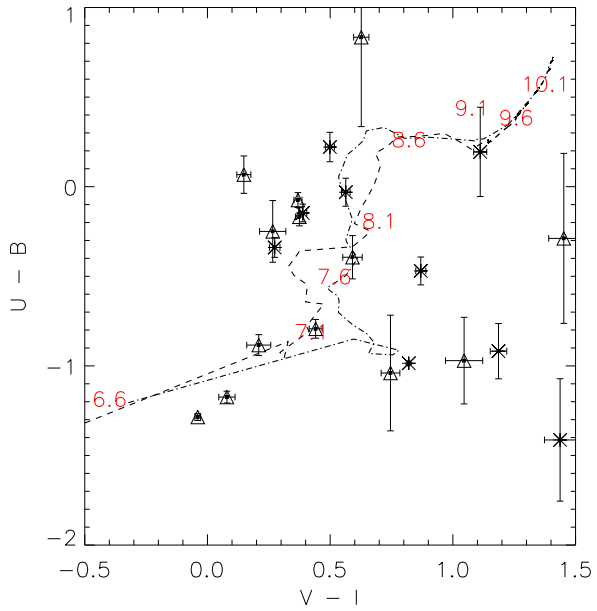

Figure 2.6: Two-color diagram for the star clusters detected in both fields, × represents the first field and △ the second field. The lines represent the theoretical GALEV track for a cluster with LMC (dashed line) or solar (dash-dotted line) metallicity, adopting Padova isochrones, a Salpeter IMF, and ages between $6.6 \leq log(\tau/\mathrm{yr}) \leq 10.1$

.

used in the original photometry. For each combination of color and magnitude, 528 artificial stars were added using 4 different regions over the image to cover crowded and uncrowded areas. These test images were created using the task *mksynth* in BAOLab (Larsen 1999) and using the original PSF images created during the photometry procedures (see Sect. 2.4.1). The separation between two consecutive stars was 100 pixels (without any sub-pixel variations), avoiding possible overlaping among the stars. The resulting test images were added to the science images using the task *imarith* in IRAF. As an example, a subsection of an image, both test and science, is presented in Fig. 2.7, where the fake stars have magnitudes $m_V = 21$.

To performe a realistic completeness analysis it is in principle necessary to sample the three-dimensional (B, V, I) color space. However, since different colors are tightly correlated with each other, the problem can be reduced to a two-dimensional one. Figure 2.8 was generated using Padova 2008 isochrones (Marigo et al. 2008), assuming solar metallicity, in the color range from -1 to 2, for $B - V$ and $V - I$ and shows that there is a nearly 1:1 relation between these two colors (the red line in Fig. 2.8 represents a 1:1 relation, but not an accurate fit to the data). We created the images

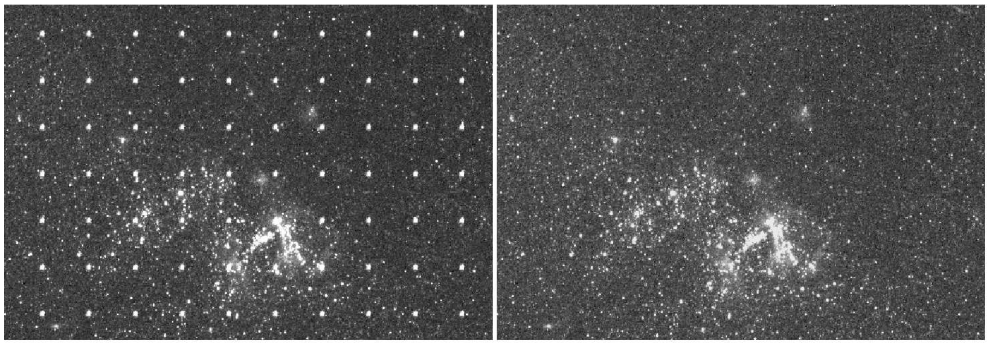

Figure 2.7: Subsection of the original image (right) and completeness image (left).

for the completeness test described above using this approximation between the three bands, i.e., if a B image has stars with $m_B = 21$ and $B - V = 1$, then the V and I images will have stars of $m_V = 20$ and $m_I = 19$, respectively, allowing us to perform a study of magnitudes and color variations over the images.

Based on these tests, we found an average of 50% completeness limits for the whole color range at $m_B = 26.69$, $m_V = 26.55$, and $m_I = 26.42$ for the first field and $m_B = 26.71$, $m_V = 26.49$, and $m_I = 26.39$ for the second field. Figure 2.9 shows the completeness diagram obtained from this analysis for the first field (for the second field, the figure is similar) and each magnitude.

The color-dependent 50% completeness limit is shown as a white dashed line in the Hess diagram (see Fig. 3.2). Since the completeness functions are very similar for the two fields, we can combine the photometry for both fields and use just one set of completeness tests in the following analysis.

We did not performe a completeness test for star clusters but refer to the tests performed by Mora et al. (2007, 2009), who used the same data and very similar cluster detection procedures. These authors created artificial star clusters using different FWHMs from 0.1pixels (stars) to 1.8 pixels and a range of magnitudes from 16 to 26 for three square grids in different positions over the image, trying to cover crowded and non-crowded areas. To create the fake clusters, they assumed a King (1962) profile with $r_{tidal}/r_{core} = 30$. Using the *mkcmppsf* task on BAOLab, fake extended objects were added to an empty image and then added to the science image to performe measurements. The selection criteria in Mora et al. (2007, 2009) is a $FWHM \geq (2.7, 0.2)$ pixels for SExtractor and *ishape*, respectively. For high background levels, Mora at al. found a shallower detection limit; nevertheless, all the limits correspond a 50% completeness limit between $m_B \approx 25$ and $m_B \approx 26$, 2-3 magnitudes fainter than the cut at V=23 that we apply for the selection of cluster candidates.

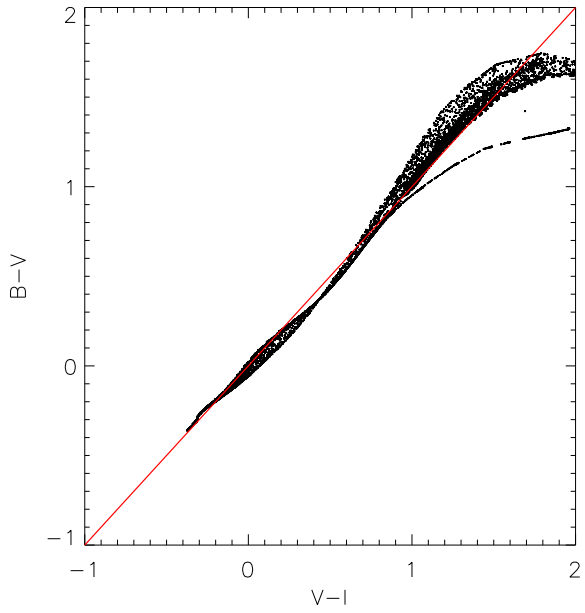

Figure 2.8: Two color diagram for theoretical values of B, V and I bands from Padova 2008 isochrones adopting LMC metallicity for ages between $10^{6.6}$ to 10^{10} yr. The red line represents a 1 : 1 relation between the colors B-V and V-I.

2.4.4. Aperture corrections

The aperture corrections were determined separately for field stars and star clusters. The aperture corrections for the field stars were derived following standard procedures, while for extended objects we adopted the relations found by Mora et al. (2009).

- Field stars:
  By "aperture corrections", we here mean corrections from the PSF-fitted instrumental magnitudes to aperture photometry for nominal radii of 0″5. These were measured using a set of isolated visually selected stars across the images. From 0″5 to infinity, we applied the Sirianni et al. (2005) values. The corrections obtained are of the order ~ 0.1 mag (see table 2.2).

- Star clusters:
  Mora et al. (2009) estimated a relation between the aperture corrections and the sizes (FWHM) of star clusters using the same data set used in this paper. Photometric parameters in both Mora et al. (2009, and ours) work are the same, allowing us to assume the relations found in their work and apply these

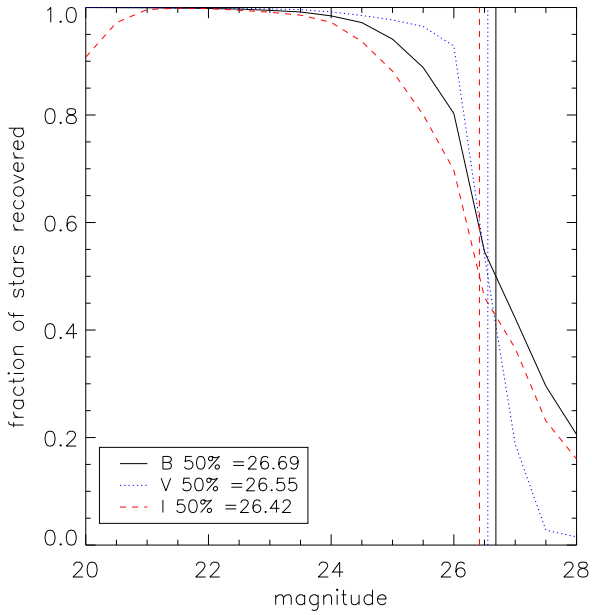

Figure 2.9: Completeness diagrams for the bands B,V, and I studied over the first field. Vertical lines represent the 50% completeness.

Table 2.2: For point source. B, V, and I aperture corrections to a nominal aperture of 0.″5, estimated in this study.

	B_{F435W} [mag]	V_{F555W} [mag]	I_{F814W} [mag]
Field 1	0.07	0.03	0.08
Field 2	0.05	0.08	0.06

aperture corrections (size-dependent) to our data, following eq. 1 in Mora et al. (2009). This set of equations is also band-dependent, although we used the sizes of the objects measured on an average image.

The aperture corrections by Mora et al. (2009) correspond to a nominal aperture of 1″45. From this nominal aperture to infinity, we adopted the values presented by Sirianni et al. (2005), although these corrections are $\sim$ 0.03 magnitudes for the bands B, V, and I (within 1″5 about 97% of the total energy is encircled).

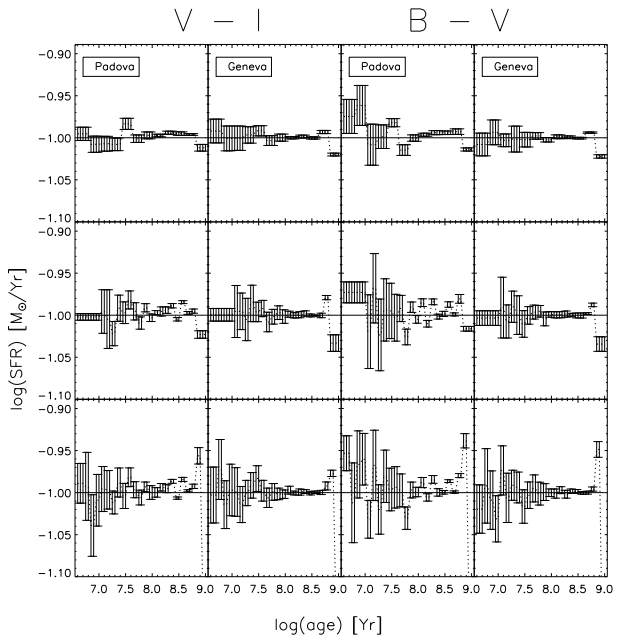

Figure 2.10: SFH test using the bands B, V, and I. Artificial populations were created using Padova and Geneva isochrones and then passed to the program. The procedure was performed 10 times and the mean SFH (dashed line) and the respective standard deviation is shown, relative to the input assumed SFH of 0.1 $M_{\odot}yr^{-1}$ (straight line). Each row represents a different binning used for the study, which decreases in size from top to bottom.

2.5. Star formation histories, ages, and masses

Our main goal in this paper is to compare the field stars with the star cluster populations in NGC 4395. In the following section, we describe how we derive the star formation histories (SFHs) of the field stars and the ages and masses of the clusters. We then proceed to compare the two.

2.5.1. Deriving star formation histories: approach and its testing

To estimate the SFH of the field stars, we have used the synthetic CMD method. The synthetic CMD method consists of creating an artificial photometric distribution of stars taking into account photometric errors, distance modulus, IMF, binarity, and interstellar extinction. The relative weights of the stellar isochrones used in generating the synthetic CMD are adjusted until the closest possible match of the synthetic CMD to the observed one is obtained. These weights can then be translated to a SFH.

Following the work of Tosi et al. (1991), Dolphin (1997), and Aparicio et al. (1997), many authors have implemented this technique. Some examples are STARFISH by Harris & Zaritsky (2002), IAC-Star by Aparicio & Gallart (2004), IAC-pop by Aparicio & Hidalgo (2009), among others. Skillman & Gallart (2002) presented the results of a workshop (The Coimbra Experiment) devoted to comparing different methods and interpretations of the results from various groups using a homogeneous data set and physical inputs. The results showed a large scatter at young ages, but good agreement at old ages.

We implemented the synthetic CMD technique ourselves as an IDL program. We chose to develop our own code to include any features that we might wish (or need), and there is no clear preference in the literature for any of the other codes. The IDL code used in this work was based on our previous experience with the synthetic CMD technique (Larsen et al. 2002). The program searches for the best-fit synthetic Hess diagram using a maximum-likelihood technique. We assume that the likelihood of observing k_i stars in the ith pixel of the Hess diagram is given by the Poisson distribution $\mathcal{P}(k_i; \mu_i)$, where μ_i is the number of stars expected in this pixel according to a given model Hess diagram. The program then searches for the linear combination of input isochrones that maximises the total likelihood $\mathcal{L}$ over the entire Hess diagram

$$\log \mathcal{L} = \sum_i \log \mathcal{P}(k_i; \mu_i). \tag{2.1}$$

In practice, we assign a low (non-zero) probability of having a star even in pixels where $\mu_i = 0$. This is essentially equivalent to allowing a constant "background level" of stars that are not fitted by any isochrone. This is necessary since any star in a pixel with $\mu_i = 0$ would otherwise immediately drive the total likelihood to zero. Since no combination of existing isochrones provides a perfect match to the observed CMDs, and one may in any case always expect some contamination of the CMD by foreground stars, background galaxies, etc., this would be overly restrictive. We also experimented with other criteria, e.g., minimum r.m.s. difference between observed and model Hess diagrams, but tests similar to those described in Sect. 2.5.2 below indicated that the maximum-likelihood method gave the most reliable results.

To create the synthetic CMD, the program uses theoretical isochrones either from Padova (Marigo et al. 2008) or Geneva (Lejeune & Schaerer 2001) or any other set of isochrones, as long as they tabulate the relevant color versus mass. If the weight of each isochrone were fitted independently, this would lead to a very large number of free parameters, due to the small difference in age between individual isochrones, e.g., $\Delta \log \tau = 0.05$ for the Padova isochrones. We therefore group the isochrones together in age bins that can be defined by the user, typically using a bin size of $\Delta \log \tau = 0.15$ dex.

The program allows us to assign different weights to different rectangular regions of the CMD, selected by the user. This is useful because some phases of stellar evolution are more uncertain than others, e.g., the blue loop stars, and thus should carry less weight in the overall determination of the SFH. The use of completeness limits

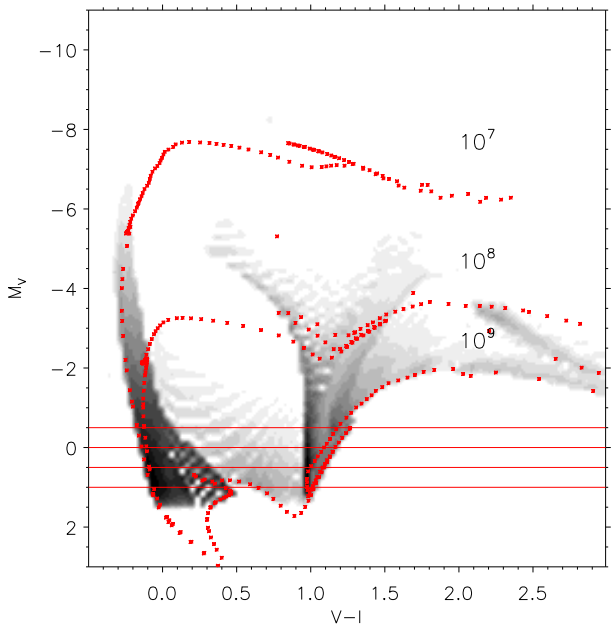

Figure 2.11: Hess diagram for the 4 possible completeness limit studied in Fig. 2.12.

(if known) can be applied before the creation of the synthetic models, interpolating the completeness limits over the whole area of the CMD. The option of applying the completeness correction after the creation of the synthetic model is simply a multiplication of each pixel in the synthetic CMD with a number between 0 and 1. We also include a simplified treatment of binaries, in which binary evolution is ignored but the effect of unresolved binaries on the CMD are modeled. The program currently allows three different assumptions about the mass ratios in binary systems, namely a delta function, an IMF sampling and a flat distribution. The metallicity, (a range of) extinction values, and distance modulus must also be specified. We allow the extinction to be age-dependent, by providing a list of ages and a range of extinction values for each age. The program then interpolates in this list for each isochrone.

Isochrones are populated by assuming a Salpeter (1955) IMF with SFHs normalised to a mass range specify by the user (M = [0.15, 100] $M_\odot$ is the default range). Since we use Hess diagrams, each point in the CMD is a density function. To construct them, different kernels, namely square, Gaussian, disc, or delta function, can be used. The kernels are of adjustable resolution and dimension. In the test presented below, we adopted a resolution for the Hess diagrams of 100×100 pixels and used a delta function kernel. Each isochrone is broadened by the assumed photometric errors and binarity, and shifted and broadened by the (range of) specified extinction values. To

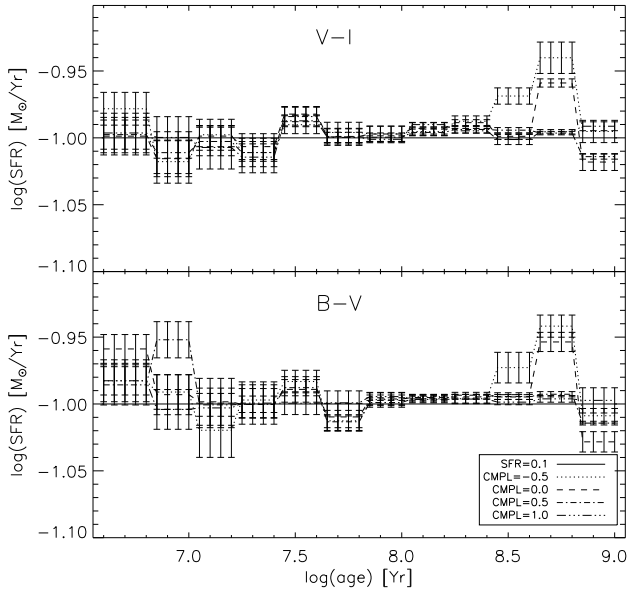

Figure 2.12: Test of the SFH using different completeness limits.

ensure a smooth coverage of the CMD, the program interpolates the isochrones by a factor of 10. After creating of the Hess diagram for each individual isochrone, the program linearly combines them and a synthetic CMD Hess diagram is obtained.

We performed a number of tests to check the internal consistency of the program, as well as the sensitivity of the derived SFHs to the various parameters involved.

2.5.2. Internal consistency check of the code

We created artificial stellar populations, passed them to the program, and then checked how the output compared to the input. The populations were constructed assuming a constant SFR of 0.1 $M_{\odot}yr^{-1}$, Padova or Geneva theoretical isochrones, a Salpeter's IMF, and solar metallicity. The mass of each star was randomly chosen using Salpeter's prescription for masses between 1 and 100 $M_{\odot}$ (low-mass stars ($\leq$ 1 $M_{\odot}$) are too faint to appear in the Hess diagram, especially after applying a completeness limit). Because we restricted the mass range in our analysis, we then extrapolated to the default mass range used by the code ($M = [0.15, 100]\,M_{\odot}$). The age of each star was assigned randomly (from a uniform distribution) for ages between 4 Myr to 1 Gyr. Having the mass and the age of each star, magnitudes were obtained by interpolating the theoretical isochrones. The magnitude limit used in these tests was

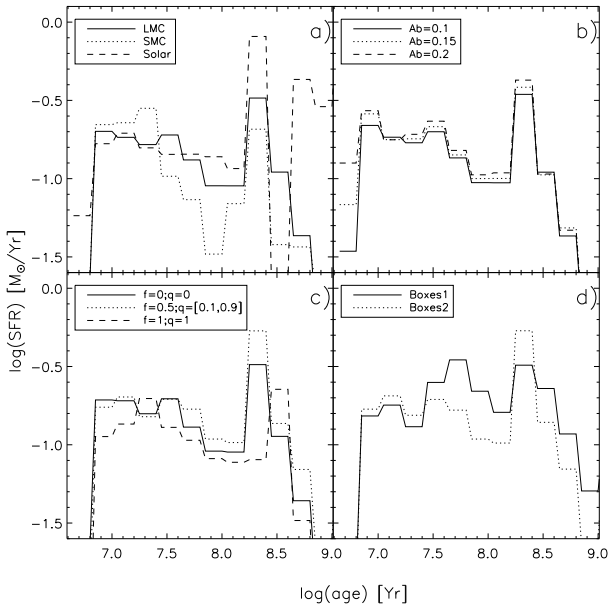

Figure 2.13: Padova theoretical isochrones were used to test the SFH program developed using the photometric data obtained in Sect. 2.4. Panel *a)*: Test for different metallicities (solar, LMC, SMC) without binarity or extinction assumed. Panel *b)*: Test for different extinctions assuming LMC metallicity and no binarity. Panel *c)*: Test for different binarity assuming LMC metallicity and no extinction. Panel *d)*: Test for different boxes used over the fitting data assuming LMC metallicity, no extinction, and no binarity.

$M_V = 0$. We did not include binaries or extinction in this initial internal consistency check of the code.

Figure 2.10 presents the results of this analysis. In all the panels, the input SFH is shown as a horizontal straight line and the average reconstructed SFH of the output after 10 different runs as dashed lines. Each run had a new population, i.e., different random realization, for the bands B, V, and I. The error bars illustrate the standard deviation in the reconstructed SFHs. We studied the variations in these results based on the different assumptions of binning. Three different bins were used in this test corresponding to each row of Fig. 2.10.

We see that the reconstructed star formation histories generally agree fairly well with the input values regardless of the binning, color, or isochrones used. It is observed that the error bars are larger for smaller bins, although good agreement with the input SFH is maintained. The maximum difference is $\Delta \log(SFR) \sim 0.05$ dex, and generally far less.

We performed a test to see how completeness affects our SFH estimation. Figure

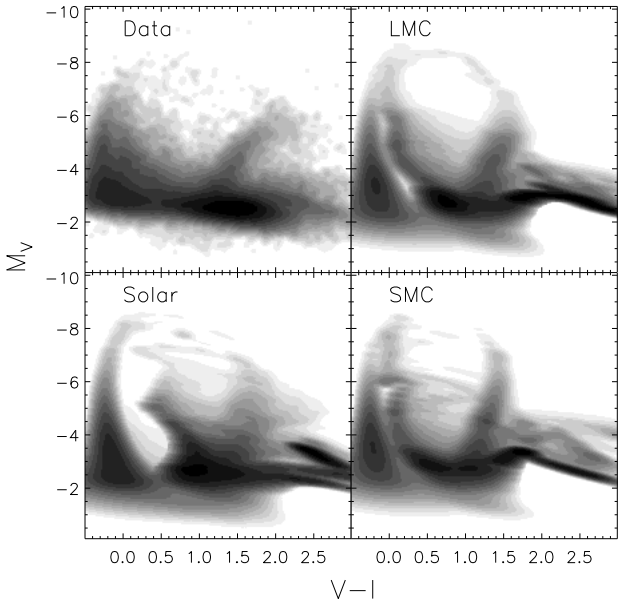

Figure 2.14: Comparison of the fit for different metallicities (solar, LMC, and SMC).

2.11 shows the Hess diagram of a stellar population with ages between 10^6 to 10^9 yr using the mass range from above. Overplotted are 3 Padova 2008 isochrones for ages $10^7, 10^8$, and 10^9 yr and four completeness limits at $M_V = [-0.5, 0.0, 0.5,$ and 1.0] magnitudes. Figure 2.12 shows that the SFHs can be recovered reliably to progressively older ages as the completeness limit becomes fainter. In particular, the "burst" at $10^{8.8}$ years disappears when fainter stars are included in the fit.

Cignoni & Tosi (2010) created artificial CMDs to simulate a stellar population with a constant SFR between $0 - 13$ Gyr and used four different completeness limits. They concluded that to safely reconstruct a SFH over a full Hubble time from a CMD, we need to resolve all stars down to $M_V = 4.5$. However, this completeness limit can only be reached for galaxies in the Local Group.

We conclude that our program produces consistent results at the level of 0.05 dex, the age range over which this holds being restricted mainly by the completeness limits. This *internal* consistency of the code does not, however, imply that real SFHs can be recovered with similar accuracy.

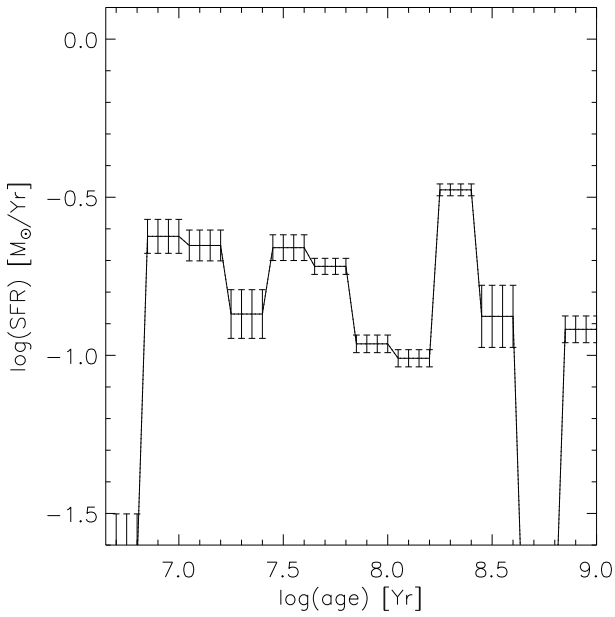

Figure 2.15: Bootstrapping study. The errors retrieved from this test are the random errors of our program. No strong variations caused by random errors affect our results.

2.5.3. Tests of sensitivity to assumptions about parameters

We now concentrate on testing the effects of four parameters: metallicity, extinction, binarity, and the fitting area used (rectangular boxes). To perform this test, we executed the code using the scientific data described in Sect. 2.4, using different assumptions about these parameters and a mass range $M = [0.10, 100]$ $M_{\odot}$ (which is the same mass range used in Sect. 2.5.4). The results are shown in Fig. 2.13. Each panel represents one of the tested variables.

In panel *a)*, we show the SFHs derived for three assumptions about metallicity: solar (Z=0.02), LMC (Z=0.008), and SMC (Z=0.004). In this panel, we ignore binaries, include no additional extinction and used the fitting area called "boxes2" described below. We observed that the SFH does not change very much from LMC to solar, but at SMC metallicity there is a much stronger increase from $\sim$ 100 Myr ago to the present. By comparing the observed and model Hess diagrams, it is clear that the solar metallicity isochrones generally provide a poor fit, especially for the red and blue supergiants that appear much too cool compared to the observations, while LMC and SMC metallicities are very similar (see Fig. 2.14).

Panel *b)* presents the behavior of the SFHs for three different assumptions about the total extinction (foreground plus internal): $A_b = [0.1, 0.15, 0.2]$. We fixed the

metallicity at $Z = 0.008$ (LMC), again ignoring binaries, used Padova isochrones and used the fitting area "boxes2". In general, the SFHs obtained using different extinctions do not vary strongly for these relatively modest variations in the extinction. Greater extinction variations would produce larger shifts towards the red in the model Hess diagrams and are inconsistent with the data.

Panel *c)* shows the dependence on the assumptions for binary fraction (f) and mass ratio (q) of values (1.) $f = 0$, $q = 0$; (2.) $f = 0.5$, $q = [0.1, 0.9]$; (3.) $f = 1$, $q = 1$. The panel also indicates how this dependence affects the estimation of the SFHs. We used Padova isochrones, fixed the metallicity at $Z = 0.008$, ignored the effects of additional extinction, and used the fitting area named "boxes2" described below. Binarity can have an effect on the derived SFHs with minor effects for $\tau \leq 100$ Myr and a shift towards somewhat lower overall SFR for the extreme case f and q equal 1. However, the binarity assumptions made here are not completely realistic. The first and third assumptions are extreme cases with no binaries at all and a galaxy where all the stars have a companion of exactly the same mass, respectively. The second assumption is an intermediate case where there is a continuous (flat) range of q values and a star has $\sim 50\%$ probability of being in a binary system. However, in a more realistic case binary *evolution* should be taken into account as well. This is

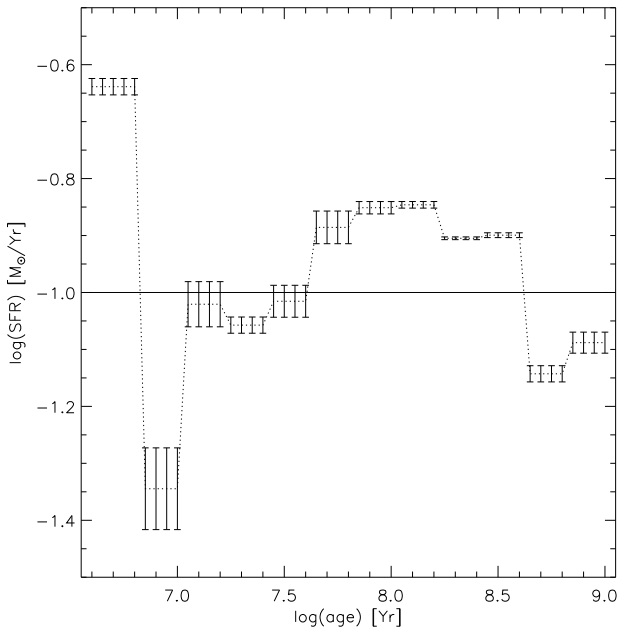

Figure 2.16: Test using Padova isochrones to create the population and Geneva isochrones to analyze them.

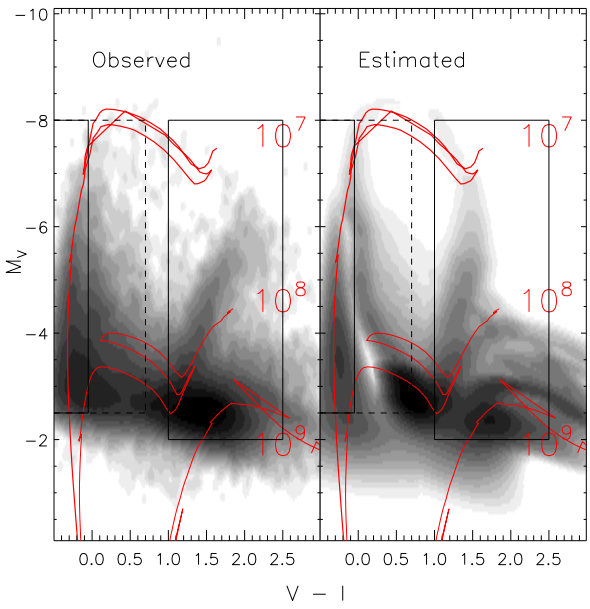

Figure 2.17: Comparison between the observed and fitted Hess diagrams for the field stars studied in this work. As age indicators, three isochrones are overplotted at the ages of 10^7, 10^8, and 10^9 yr. Boxes used to fit the data are represented for both Hess diagrams, observed and fitted.

however beyond the scope of the present work.

In the last panel, panel *d)*, we show the SFH estimates obtained using two different sets of boxes in the fitting. As overplotted in Fig. 2.17, where we plot the observed Hess diagram and the regions fitted, the left box ($-0.5 \leq V-I \leq -0.05$ and $-8.0 \leq V \leq -2.5$) used contains the main sequence stars, the blue He core burning phases being outside of the fit, while the right box ($1.0 \leq V-I \leq 2.5$ and $-8.0 \leq V \leq -2.0$) contains the red He core burning stars and possible RGBs and AGBs. This set of boxes is called "boxes2". The second set of boxes covers the same area for the evolved stars (right box), while the blue He core burning stars are also included in the fitting box ($-0.5 \leq V-I \leq 0.7$), which we label "boxes1" in panel *d)*. In general, we found that, the SFH result from "boxes2" shows a lower value that for "boxes1". We studied these two possible sets of boxes because the fitted Hess diagrams retrieved using these two boxes indicated that the fit for the blue He core burning stars is not in good agreement with observations. The variations after $\sim \tau \sim 10^{8.7}$ yr are unlikely to be real, but are probably due to incompleteness as discussed above.

We created a fake population using Padova isochrones and assuming solar metallicity, no extinction, and no binarity; we then analyze this with our program, using

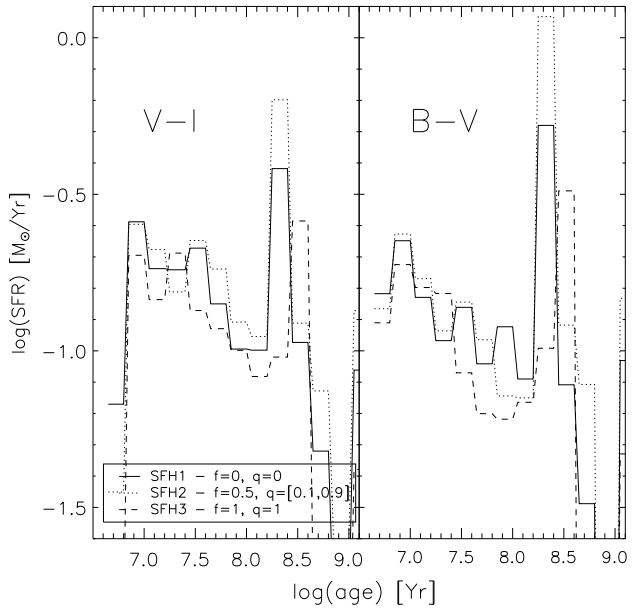

Figure 2.18: SFH for the galaxy NGC 4395. We studied the SFH for three different assumptions about the binaries trying to cover possible combinations between binary fraction and mass ratio for the colors V-I(left panel) and B-V(right panel).

Geneva isochrones to see whether the assumed SFH could be recovered. Figure 2.16 shows the result of this test. There are significant differences between the input and recovered SFH, deviations being as large as $\sim$ 0.4 dex at young ages (< 10 Myr) and differences being at the level of 0.1-0.2 dex at older ages. The error bars presented in Fig. 2.16 were determined using the same method used in the previous section, i.e., are equivalent to the standard deviation of the reconstructed SFHs after 10 different runs with different random realizations.

We finally test how random errors (due to the finite number of stars in the Hess diagram) affect the SFHs, using a bootstrapping method whereby the input data, i.e., the photometric data found in this work, are randomly resampled many times. To perform this test, we used the observations obtained in this work (see Sect. 2.4), Padova 2008 isochrones, LMC metallicity, no additional extinction, and no binarity. Disabling binarity will not influence our results dramatically and will save us computational time. We ran the program 100 times, redistributing randomly the photometric data in each run. From Fig. 2.15, we conclude that Poisson variations do not significantly affect our results.

To summarize, we demonstrated that the main uncertainties in our derived SFHs are systematic, depending on assumptions about binarity, the choice of isochrones,

and metallicity. However, with the exception of the use of solar metallicity isochrones (which provide a poor fit to the data), the overall mean SFRs are fairly consistent with our data up to ages of a few hundred Myr.

2.5.4. Results

To infer the SFH of NGC 4395, we combined both fields to be able to directly compare with the cluster age distribution. The differences in our completeness limits for each band and each field are smaller than 0.1 magnitudes, allowing us to use the completeness values obtained in our first field (results for the second field can also be used instead) to study the SFH of the whole galaxy. In the SFH reconstruction, we used a resolution of 200×200 pixels for the Hess diagrams and a Gaussian kernel with a standard deviation of 0.02 mag in $V - I$ (or $B - V$). Based on our observed Hess diagram we used 2 rectangular fitting areas (*boxes2*) for the SFH reconstruction with the same limits as described in the previous section. To check the consistency of our results we performed the analysis using both $B - V$ and $V - I$ colors, using the same parameters and boxes to fit the data.

Figure 2.17 depicts the observed (left) and best-fit model (right) Hess diagrams (assuming $f = 0.5$ and $q = [0.1, 0.9]$). The final combination of parameters used to estimate the SFH were Padova 2008 isochrones, a Salpeter IMF (M=[0.10,100] $M_{\odot}$), LMC metallicity, three different assumptions for the binarity, distance modulus of 28.1, a total extinction of $A_B = 0.15$, and the photometric errors and completeness limit obtained in Sect. 2.4.

The phases that are most accurately reproduced by the fit are the main sequence, red core-He burning, and RGB/AGB phases. For the blue core-He burning phases, the model fit is less good, being redder than observed and with a more pronounced gap between the main sequence and blue core-He burning stars in the model than in the data. This is a generic problem with the isochrones that exists for any star formation history we adopt.

Our most accurate estimates of the extinction were obtained by trial and error. We compared the main sequence stars from the fitted Hess diagram with data for those observed and assumed different values ($A_B = [0.1, 0.15, 0.2]$) for the total extinction until we obtained the best fit between the two Hess diagrams (considering the main sequence only). The difference between the foreground value ($A_B = 0.074$) and our best-fit model value ($A_B \sim 0.15$) suggests a low internal extinction in NGC 4395 of $A_B \approx 0.076$ mag. This estimation was performed for LMC metallicity.

The estimated SFHs (for $V - I$ and $B - V$) are shown in Fig. 2.18. As discussed in the previous section, the SFHs become very uncertain at ages greater than a few hundred Myr; the apparent burst at $\sim 10^{8.4}$ yr is probably not real. There is also a hint of a rapid drop at very young ages in V-I ($\sim 10^{6.8}$ years), but this may be caused by uncertainties in the isochrones. Furthermore, the youngest age included in our artificial Hess diagrams is 4 Myr; if younger stars were present in the field, these would be included in the youngest bin. The appropriate lower age limit depends on how long young stars are embedded in their native molecular clouds. We present

Table 2.3: Average star formation rate [in $M_\odot Yr^{-1}$] over the past 10^8 years, estimated using different binarity, colors, and isochrones.

	$f = 0$	$f = 0.5$	$f = 1$
	$q = 0$	$q = [0.1, 0.9]$	$q = 1$
		Padova	
V-I	0.18	0.19	0.15
B-V	0.14	0.14	0.12
		Geneva	
V-I	0.20	0.21	0.19
B-V	0.16	0.20	0.16

the SFHs for different binarity assumptions because this parameter is also uncertain. We use the same 3 choices in Fig. 2.18 as those used in Fig. 2.13 above. Taking the values for each bin (in linear units), we estimated the average star formation rate for ages between 10^7 and 10^8 years using the colors V-I and B-V, as shown in Table 2.3.

There is an apparent increase in the SFR between $\log \tau \sim 10^{8.0}$ and $\log \tau \sim 10^{7.0}$, of ~ 0.5 dex. Based on Fig. 2.18, the average star formation rate over the past 10^8 years is $SFR \approx 0.17\ M_\odot yr^{-1}$ within the two ACS fields (assuming $f = 0.5$ and $q = [0.1, 0.9]$). We note that this is a factor of 4 higher than the *global* SFR for NGC 4395 that follows from using the far-infrared luminosity described in Larsen & Richtler (2000), who used the calibration by Buat & Xu (1996). This highlights the difficulty in determining extragalactic star formation rates from integrated light.

2.5.5. Ages and masses of clusters

After identifying the star cluster candidates (see Sect. 2.4) in the two fields, we need to estimate their masses and ages. These parameters were estimated using the program AnalySED, created by Anders et al. (2004). This program determines the masses and ages using GALEV SSP evolutionary models (Schulz et al. 2002). The parameters used for AnalySED are a Salpeter IMF (Salpeter 1955) in the mass range 0.10 to 100 $M_\odot$, Padova isochrones (Girardi et al. 2000), and a LMC metallicity. AnalySED performs a match, comparing the observed and theoretical spectral energy distributions (SEDs), based on GALEV SSP models. As output, AnalySED provides, among other parameters, an estimation of the mass and the age for each cluster.

In addition to our magnitude limit of $V = 23$ ($M_V \sim -5$) for our clusters, we also define a lower mass limit at $10^{2.5}\ M_\odot$ to increase the likelihood that extended objects are true clusters and not just chance projections of a few bright stars. However, over most of the age range ($Log(age) \geq 7$), these false detections would fall below our magnitude limit.

Figure 2.19 shows the age-mass diagram of the cluster candidates in NGC 4395. The number of clusters detected is rather small because the two HST pointings do not cover the whole galaxy and our coverage for clusters is reduced further by our

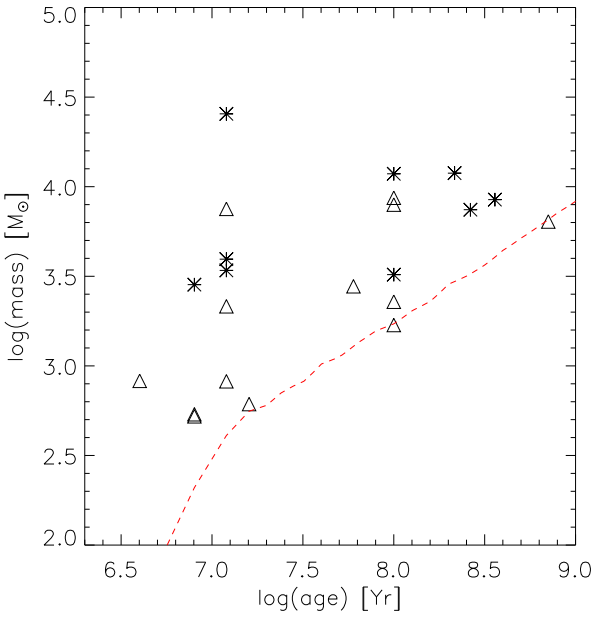

Figure 2.19: Age-mass distribution of the clusters detected in our two fields observed. The red dashed line represents $M_V = -5$. Symbols are the same as in Fig. 2.6.

requirement of the WFPC2 pointings for age-dating. We see that neither massive ($M \geq 10^5$ $M_\odot$) nor old ($\tau \geq 10^9$ yr) clusters are detected, in agreement with previous work (Larsen & Richtler 1999, Mora et al. 2009). We identified few clusters with $\tau > 100$ Myr for LMC metallicity in agreement with Mora et al. (2009), although the number of objects was greater in their work. Nevertheless, the number of objects detected at these ages (and greater) varies, as can be see in Fig. 7 of Mora et al., depending on the metallicity used to estimate the parameters.

2.6. Summary, discussion, and conclusions

We have described our procedures to obtain the age distributions of field stars and star clusters in HST images of nearby ($D \approx 4$ Mpc) galaxies, in particular, we have described our implementation of the synthetic CMD method and tests of our program developed for this purpose. We found that the code recovers the star formation histories of synthetic populations with good accuracy, while errors in the derived SFHs of true populations are dominated by systematics errors. We have derived the SFH for NGC 4395 for three different metallicities and find an approximately constant SFR over the past few hundred Myr assuming LMC-like metallicity. Only a modest

amount of internal extinction ($A_B \approx 0.08$) in NGC 4395 is required in addition to the Galactic foreground extinction to match the data. Hence, uncertainties in the total extinction is not a major source of error compared to, for example, binary stars and the choice of isochrones. Different assumptions may lead to changes in our estimated SFRs of up to a factor of 2–4 in specific age bins, although the global average will be less affected. Poissonian errors do not contribute substantially to the uncertainties because of the large number of field stars used in our analysis.

After estimating the SFH of the field stars and both the age and mass distributions of star clusters, we can now measure which fraction of stars are in clusters. We compare the fractions for cluster ages between 10^7 and 10^8 years, since disruption due to tidal shocks (GMC and spiral arm encounters) and evaporation is expected to become significant at older ages, while younger objects may still be unbound and prone to "infant mortality".

A rough estimate of the cluster formation rate (CFR) can be obtained by dividing the total amount of mass in clusters observed by the age range. From $10^7 \leq \tau \leq 10^8$ yr, the total mass observed in Fig. 2.19 is $M_{obs} \sim 8.3 \times 10^4$ $M_\odot$, which infers a $\log(CFR) \approx -3.03$ [$M_\odot yr^{-1}$]. We correct this for the smaller area covered by the WFPC2 camera compared to the ACS (a factor of ~ 2.27) and thus obtain $\log(CFR) \approx -2.68$ [$M_\odot Yr^{-1}$] for the same equivalent area covered by our field star data.

A magnitude-limited sample does not allow us to observe all the clusters in the age range. Using the observed total mass and assuming a cluster mass function ($\Psi(m)$), we can estimate the total mass in clusters for a certain age range. Larsen (2009) showed that a Schechter function (with $M_\star = 2 \times 10^5 M_\odot$) can model the initial cluster mass function in present-day spiral discs. However, the canonical cluster mass function, a power law with index -2, can be used for the same purpose. To estimate the cluster formation rate we used both functions and calculated the total mass in the age range mentioned above. Since the most massive clusters observed have M$< 10^5$ $M_\odot$, it makes little difference whether we adopt the Schechter function or an untruncated power-law.

The total mass in the cluster system was estimated using the equation

$$M_{tot} = M_{obs} \times \frac{(t_2 - t_1) \int_{m_{lo}}^{m_{up}} m\Psi(m)\, dm}{\int_{t_1}^{t_2} \int_{m_{lim(t)}}^{m_{up}} m\Psi(m)\, dm\, dt}\,, \tag{2.2}$$

where t_1, t_2 represent the time interval ($t_1 = 10^7$ years, $t_2 = 10^8$ years), m_{lo} and m_{up} are the lower and upper mass limits over which the mass is normalized ($m_{lo} = 10$ and $m_{up} = 10^6$ $M_\odot$), and $m_{lim(t)}$ is the (age-dependent) detection limit of our cluster sample (dashed line in Fig. 2.19). Since the last parameter, m_{lim}, is derived from the SSP models used, this integral must be evaluated numerically. Equation (2.2) assumes a uniform cluster age distribution, which is the most conservative choice we can make given the small number of clusters in our sample and the uncertainties in the age determinations (Fig. 2.6). We also assume that $\Psi(m)$ is age-independent, meaning that we ignore disruption. Applying the correction for undetected clusters,

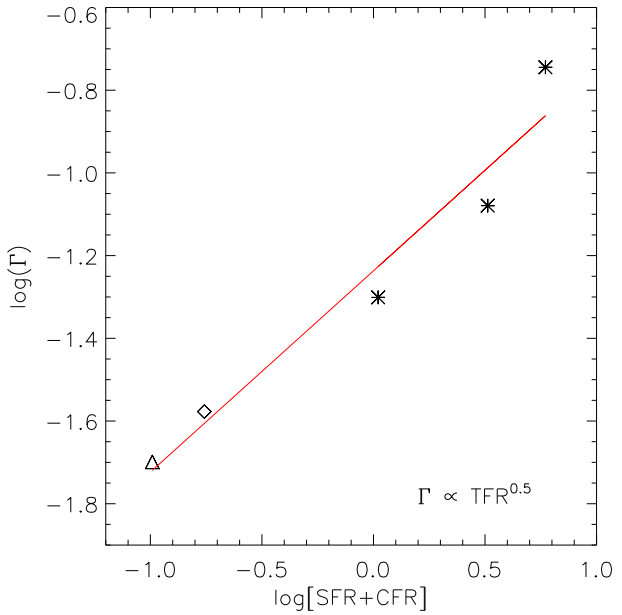

Figure 2.20: Relation between the cluster formation efficiency (Γ) and the total formation rate ($TFR = SFR + CFR$). An apparent power law function fits the date following the equation $\Gamma \approx TFR^{0.5}$. Symbols represent: ⋆ are data from Gieles (2010) for the galaxies M74, M101 and M51; △ is for the SMC (Gieles & Bastian 2008); and ⋄ our estimation for NGC 4395.

we obtained values for the CFR of $\log(CFR) = -2.37$ and $\log(CFR) = -2.35$ for power law and Schechter functions respectively, values that are corrected for the area covered by the HST detectors mentioned above. We have also tried applying Eq. (2.2) to 3 sub-bins in age, which changed the total overall CFR by a very small amount. We note that, strictly speaking, we are not measuring the true cluster *formation* rate, but rather the current *age* distribution of surviving clusters. Dividing these numbers by the SFR ($SFR = 0.17\ M_{\odot}Yr^{-1}$), we obtain a ratio of $\Gamma = CFR/SFR = 0.0263$.

Our estimate of Γ is lower than the value $\Gamma \sim 0.08$ obtained by Bastian (2008). Gieles (2010) estimated Γ for three galaxies namely M74, M101, and M51. The cluster formation rate was estimated by comparing theoretical with empirical luminosity functions. Gieles suggested that Γ has the tendency to increase with SFR. Gieles & Bastian (2008) estimated $\Gamma \approx 0.02$ for the SMC using an accurate determination of the mean global star formation rate based on the field stars (SFR$\approx 0.1\ M_{\odot}Yr^{-1}$) performed by Harris & Zaritsky (2004) and the CFR calculated in their work. Other studies have found the same value for Γ in the SMC (see Goddard et al. 2010). We took the data from Gieles (2010) (see Table 1 in his article), and Gieles & Bastian (2008) and plotted the total formation rate ($TFR = SFR + CFR$) against Γ for these four galaxies

and included our CFR and SFR for NGC 4395 to attempt to detect any correlation. Figure 2.20 shows the plot of log(Γ) versus log(*TFR*). There is an apparent correlation between these two values, which can be approximated by a power law $\Gamma \propto TFR^{0.5}$. Although only five points are plotted and the TFR in NGC 4395 does not cover the whole galaxy, Fig. 2.20 does suggest that the relatively low Γ value we derive for NGC 4395 is consistent with a general trend. In a future study (Silva-Villa et al. 2010, in prep.), we will include more points in this plot for galaxies spanning a range in TFR and check the validity of this result.

Goddard et al. (2010) found an empirical relation between Γ and the SFR density (Σ_{SFR} [$M_\odot yr^{-1}Kpc^{-2}$]). We estimated Σ_{SFR} to be $\sim 4.65 \times 10^{-3}$ $M_\odot Yr^{-1}Kpc^{-2}$ for NGC 4395, which leads to $\Gamma \approx 8\%$ based on the Goddard et al. (2010) relation. This value is higher than that estimated in this work $\Gamma \approx 3\%$. We point out that the area covered by our observations is not the total area of the galaxy and so the SFR density found in this work might be higher than the global average.

Silva-Villa would like to thank Peter Anders for help with the program AnalySED. We thank C. U. Keller and the referee for comments that helped improve this article.

Common sense is not so common.
–Voltaire

Chapter 3

The star cluster - field star connection in nearby spiral galaxies. II. Field star and cluster formation histories and their relation.

E. Silva-Villa & S. S. Larsen
Published in *Astronomy & Astrophysics*, 529, A25 (2011)[1]

Abstract

Recent studies have started to cast doubt on the assumption that most stars are formed in clusters. Observational studies of field stars and star cluster systems in nearby galaxies can lead to better constraints on the fraction of stars forming in clusters. Ultimately this may lead to a better understanding of star formation in galaxies, and galaxy evolution in general. We aim to constrain the amount of star formation happening in long-lived clusters for four galaxies through the homogeneous, simultaneous study of field stars and star clusters. Using HST/ACS and HST/WFPC2 images of the galaxies NGC 45, NGC 1313, NGC 5236, and NGC 7793, we estimate star formation histories by means of the synthetic CMD method. Masses and ages of star clusters are estimated using simple stellar population model fitting. Comparing observed and modeled luminosity functions, we estimate cluster formation rates. By randomly sampling the stellar initial mass function (SIMF), we construct artificial star clusters and quantify how stochastic effects influence cluster detection, integrated colors, and age estimates. Star formation rates appear to be constant over the past $10^7 - 10^8$ years within the fields covered by our observations. The number of clusters identified per galaxy varies, with a few detected massive clusters ($M \geq 10^5$ $M_\odot$) and a few older than 1 Gyr. Among our sample of galaxies, NGC 5236 and NGC 1313 show high star and cluster formation rates, while NGC 7793 and NGC 45 show lower values. We find that stochastic sampling of the

[1]Reproduced with permission © ESO

SIMF has a strong impact on the estimation of ages, colors, and completeness for clusters with masses $\leq 10^3 - 10^4$ $M_\odot$, while the effect is less pronounced for high masses. Stochasticity also makes size measurements highly uncertain at young ages ($\tau \lesssim 10^8$ yr), making it difficult to distinguish between clusters and stars based on sizes. The ratio of star formation happening in clusters (Γ) compared to the global star formation appears to vary for different galaxies. We find similar values to previous studies ($\Gamma \approx 2\%$–10%), but we find no obvious relation between Γ and the star formation rate density ($\Sigma_{\rm SFR}$) within the range probed here ($\Sigma_{\rm SFR} \sim 10^{-3} - 10^{-2} M_\odot$ yr^{-1} kpc^{-2}). The Γ values do, however, appear to correlate with the specific U-band luminosity (T_L(U), the fraction of total light coming from clusters compared to the total U-band light of the galaxy).

3.1. Introduction

It is often assumed that stars can be formed either in the field of a galaxy as single stars or in a group of stars (cluster) that formed from the same molecular cloud at the same time. However this view has been recently questioned by Bressert et al. (2010), who challenged the idea that field and cluster formation are actually distinct modes of star formation.

Owing to dynamical and stellar evolution clusters disrupt (Spitzer 1987) and the stars become members of the field stellar population. While it is commonly assumed that most (if not all) stars formed in clusters (e.g. Lada & Lada 2003, Porras et al. 2003, in the solar neighborhood), the amount of star formation happening in those clusters that remain bound beyond the embedded phase is still uncertain. In any case, if clusters are to be used as tracers of galactic star formation histories, it is of key importance to understand what fraction of star formation is happening in long-lived clusters and whether or not this fraction correlates with other host galaxy parameters. Following Bastian (2008), we refer to this fraction as Γ.

Estimating Γ is not straightforward. Apart from differences arising at the time of formation, cluster disruption will also affect the detected number of clusters of a given age (τ). Lada & Lada (2003) estimate that between 70% to 90% of the stars in the solar neighborhood form in embedded star clusters, while only 4–7% of these clusters survive for more than about 100 Myr. Similarly, Lamers & Gieles (2008) estimate an "infant mortality" rate of 50% to 95%, based on a comparison of the surface density of open clusters and the star formation rate near the Sun. By studying the UV flux in and out of clusters in the galaxy NGC 1313, Pellerin et al. (2007) suggest that over 75% (between 75% and 90%) of the flux is produced by stars in the field, concluding that the large number of B-type stars in the field of the galaxy could be a consequence of the (high) infant mortality of clusters. For the Small Magellanic Cloud, Gieles & Bastian (2008) estimate that optically visible, bound clusters account for 2%-4% of the star formation, while Gieles (2010) estimates this fraction to be in the range 5%–18% for the spiral galaxies M74, M51, and M101. However, most of these studies could not distinguish between scenarios in which a large fraction of stars initially form in clusters that rapidly dissolve or whether there is a genuine "field" mode of star formation. Studying the Antennae galaxy, Fall (2004) estimates that 20% (and possibly all) stars were formed in clusters. Using a larger sample of galaxies, Goddard et al. (2010) find a power-law relation ($\Gamma \propto \Sigma_{\rm SFR}^{\alpha}$) between the fraction of stars forming in clusters that survive long enough to be optically visible and the star formation rate density of the galaxy ($\Sigma_{\rm SFR}$). Their data set covers different types of galaxies, from irregulars (i.e. LMC, SMC, and NGC 1569) to grand design spirals (i.e. NGC 5236). The $\Sigma_{\rm SFR}$ of these galaxies vary from 7×10^{-3} to $\sim 700 \times 10^{-3}$ $M_{\odot}yr^{-1}Kpc^{-2}$. Their Γ vs. $\Sigma_{\rm SFR}$ relation, however, is based on somewhat heterogenous data with different mass- and age ranges, which do not come from the same observations (see details in Sect. 4 of Goddard et al. 2010), although the authors do attempt to homogenize the sample by normalizing the cluster samples to a common mass limit.

The actual definition of the phase called *infant mortality* is somewhat ambiguous in

the literature. Early disruption due to rapid gas expulsion may only take a few Myrs, but the term has also been used to describe mass-independent disruption, meaning that clusters lifetime is independent of mass over a much longer time span. In the latter case, the "infant mortality rate" (IMR) refers to the fraction of clusters that are disrupted per decade of age. We prefer to simply use the term "mass-independent" disruption (MID) in this case. For MID, the IMR is related to the slope a of the age distribution, $dN/d\tau \propto \tau^a$ of a mass limited cluster sample as $a = \log(1 - \mathrm{IMR})$ (Whitmore et al. 2007). For example, de Grijs & Goodwin (2008) found that for the SMC the IMR is close to 30% (between 3-160 Myr), while the logarithmic age distribution of clusters in the Antennae galaxies is about flat ($a \approx -1$), indicating an IMR close to 90% (Fall 2004), assuming that the star formation rate has been about constant over the past few 10^8 years. On theoretical grounds, the time scale for the (gradual) cluster disruption is expected to be mass-dependent, owing to tidal shocks and evaporation that follows early gas expulsion (e.g. Gieles et al. 2006), assuming there is no strong relation between cluster mass and radius. In this description, the dissolution time $t_{\rm dis}$ of a cluster scales with cluster mass as $t_{\rm dis} = t_4(M/10^4 M_\odot)^\gamma$, where t_4 is the lifetime of a 10^4 $M_\odot$ cluster (see Boutloukos & Lamers 2003, Lamers et al. 2005). The time scale on which clusters dissolve may also depend on external factors, such as the tidal field strength, density of molecular gas, passages near/through giant molecular clouds, or through spiral arms, etc. (see e.g. Gieles et al. 2006, 2007). This scenario attempts to compile in one single formula all the possible processes that affect cluster disruption. See Lamers (2009) for a description of the different models for cluster dissolution.

Determining the extent to which cluster dissolution is a mass-dependent process has turned out to be difficult. Estimations of cluster parameters based on observations are affected by stochastic effects, degeneracies, and observational uncertainties. For example, Maíz Apellániz (2009) used Monte Carlo simulations to estimate how stochastic effects coming from the random sampling of the stellar initial mass function influence the determination of ages and masses, which are derived from broadband photometry. Piskunov et al. (2009) show how the consideration of the discreteness of the stellar initial mass function (IMF) can explain features observed in the color-age relation and can improve the fit between models and observations. They conclude that the large number of red outliers can be explained as a systematic offset coming from the difference between discrete- and continuous-IMF at low masses (M_c=10^2 $M_\odot$) and young ages ($\log(\tau)[yr] \sim 7$), reaching up to ~0.5 magnitudes, and decreases down to ~0.04 magnitudes at higher masses (M_c=10^6 $M_\odot$).

To estimate field star formation histories, a different approach is needed than for clusters, because ages cannot in general be determined directly for individual stars. Tosi et al. (1991) presented a method that takes incompleteness, resolution, depth, and observational errors (among other parameters) into account to construct a synthetic color-magnitude diagram (CMD), which can be used to estimate the star formation history by comparison with observations . This method has been developed further by other authors in the past years, e.g. Dolphin (1997) and Harris & Zaritsky (2001), and has been used for a large number of galaxies, e.g. SMC, LMC (Harris & Zaritsky

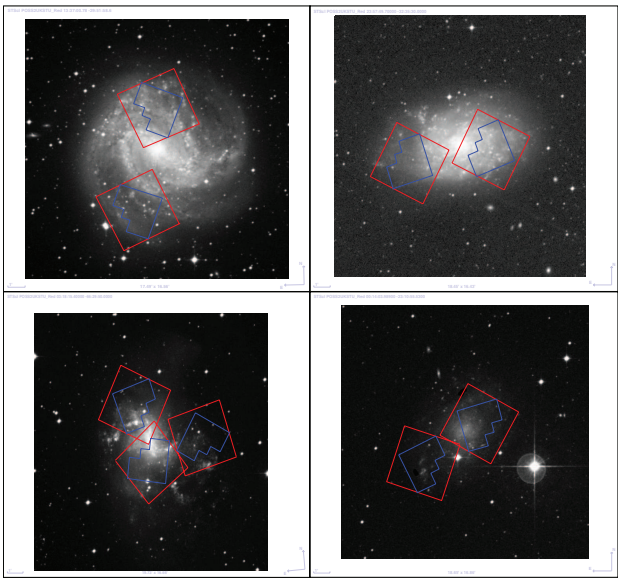

Figure 3.1: Galaxies studied in this paper. *Top left*: NGC 5236; *top right*: NGC 7793; *bottom left*: NGC 1313; and *bottom right*: NGC 45. Red lines represent the pointings covered by the HST/ACS, while the blue lines represent the pointings of the HST/WFPC2. Images were taken from the DSS archive using Aladin software.

2004, 2009), M31 (Brown et al. 2008), NGC 1313 (Larsen et al. 2007). In this series of papers, we make use of this method to estimate the field star formation rates of our target galaxies, which we then compare with cluster formation rates to estimate Γ.

In Silva-Villa & Larsen (2010, hereafter Paper I), we presented the tools needed to study and constrain the Γ value of our set of galaxies, and used NGC 4395 as a testbed galaxy. As the second paper in a series, this paper aims to estimate Γ in different environments and compare it with previous work (e.g. Gieles 2010, Goddard et al. 2010), using the complete set of galaxies. To this end, we took advantage of the superb spatial resolution of the *Hubble Space Telescope* (HST) and used images of the galaxies NGC 5236, NGC 7793, NGC 1313, and NGC 45, which are nearby, face-on spiral galaxies that differ in their current star formation rates and morphology. These galaxies are near enough ($\approx$ 4 Mpc) to allow us to disentangle the cluster system from the field stars, making it possible to estimate cluster and star formation histories separately and simultaneously from the same data.

The paper is structured as follows. In Sect. 3.2, we present a short overview of previous work on our target galaxies, related to the present study. The basic reduction and characteristics of the observations are described in Sect. 3.3. In Sect. 3.4 we present the photometry procedures applied to the data and describe how completeness tests were carried out. We also discuss the effect of stochastic sampling of the stellar IMF on integrated cluster properties. In Sect. 3.5 we present the results

Table 3.1: Galaxy parameters.

Galaxy	$Type^{\dagger}$	$(m-M)^{\ddagger}$	A_B^a	Z	$12 + log(O/H)$
NGC 5236	SAB(s)c	27.84	0.29	0.008,0.019[1]	8.2-8.6[1]
NGC 7793	SA(s)d	27.6	0.08	0.008,0.019[2]	8.57[5]
NGC 1313	SB(s)d	28.2	0.47	0.004,0.008[3]	8.33[5]
NGC 45	SA(s)dm	28.42	0.09	0.004,0.008[4]	—

† NASA/IPAC Extragalactic Database (NED); ‡ Mora et al. (2009) and references therein; ^{a} Schlegel et al. (1998); [1] Bresolin et al. (2009); [2] Calzetti et al. (2010);[3] Walsh & Roy (1997), Larsen et al. (2007); [4] Mora et al. (2007); and [5]Zaritsky et al. (1994) at r = 3 Kpc.

of the estimation of ages and masses of clusters, as well as the field star formation histories. We also estimate the cluster formation rates and use these to determine Γ values. In Sect. 3.6 we discuss our results and finally, we summarize and conclude our work in Sect. 3.7.

3.2. Dataset overview

In this paper we describe results for the remaining four galaxies in our HST/ACS sample: NGC 5236, NGC 7793, NGC 1313, and NGC 45. These four galaxies share the properties of being face-on, nearby spirals; however, they differ in their morphology, star, and cluster formation histories. We present the basic properties of each galaxy in Table 3.1.

Larsen & Richtler (1999) studied cluster populations in a set of 21 galaxies, including the four included here. Using ground-based multiband (*UBVRI* and Hα) observations they estimated the total number of young massive clusters in each galaxy, using a magnitude limit of $M_V \leq -8.5$. In a further work, Larsen & Richtler (2000) estimated the star formation rate density ($\Sigma_{\rm SFR}$) and the specific U-band luminosity, $T_L(U)$ = 100×L(clusters,U)/L(galaxy,U), for each galaxy. The $T_L(U)$ was found to correlate with $\Sigma_{\rm SFR}$. Taking $T_L(U)$ as a proxy for the cluster formation efficiency, these data thus suggested an increase in the cluster formation efficiency with $\Sigma_{\rm SFR}$. It is worth noting here that the $\Sigma_{\rm SFR}$ values were derived by normalizing the total star formation rates, obtained from IRAS far-infrared fluxes, to the optical galaxy diameters obtained from the RC3 catalog. Therefore, while these numbers were useful for studying trends and correlations, they should not be taken as reliable absolute values.

More recent estimates of $\Sigma_{\rm SFR}$ have been made by Calzetti et al. (2010) for the galaxies NGC 5236 and NGC 7793, where they found similar values to Larsen & Richtler (2000). Harris et al. (2001) present a photometric observation of clusters in the center (inner 300 pc.) of NGC 5236. Harris et al. find a large number of young

Table 3.2: Journal of the observations.

Galaxy	Number of field	F336W(U) sec.	F435W(B) sec.	F555W(V) sec.	F814W(I) S	RA. (J2000)	DEC. (J2000)	Date
NGC 5236	1	2400	680	680	430	13:37:00	-29:49:38	2004.07.28
	2	2400	680	680	430	13:37:06	-29:55:28	2004.08.07
NGC 7793	1	2400	680	680	430	23:57:41	-32:35:20	2003.12.10
	2	2400	680	680	430	23:58:04	-32:36:10	2003.12.10
NGC 1313	1	2800	680	680	676	03:18:04	-66:28:23	2004.07.17
	2	2800	680	680	676	03:18:17	-66:31:50	2004.12.18
	3	2800	680	680	676	03:17:43	-66:30:40	2004.05.27
NGC 45	1	2400	680	680	430	00:14:14	-23:12:29	2004.07.05
	2	2400	680	680	430	00:14:00	-23:10:04	2004.06.01

and massive clusters, consistent with a burst of star formation that began around 10 Myr ago, but note that the apparent absence of older clusters might also be due to rapid disruption. Chandar et al. (2010) used the new Wide Field Camera 3 (WFC3) on HST to analyze the cluster system of NGC 5236. They find that luminosity functions and age distributions are consistent with previous work on galaxies of different morphological types (e.g. Fall 2004). Mora et al. (2007, 2009) studied the cluster system for the same set of galaxies used in this work, based on the same HST images. They present detailed estimates of the sizes, ages, and masses for the clusters detected. Mora et al. conclude that the age distributions are consistent with a ~80% MID per decade in age up to 1 Gyr, but could not make a distinction between different models (MDD vs. MID) of cluster disruption. In the galaxy NGC 45 they found a large number of old globular clusters, of which 8 were spectroscopically confirmed to be ancient and metal-poor (Mora et al. 2008).

3.3. Observation and data reduction

The five galaxies studied in this series of papers were selected for detailed observations with the *Advanced Camera for Surveys* (ACS) and *Wide Field Planetary Camera 2* (WPFC2) onboard HST from the work of Larsen & Richtler (1999, 2000). The two instruments have a resolution of 0"05 and 0"046, 0"1 for ACS and WFPC2 (PC,WFs), respectively. At the distance of our galaxies (~ 4 Mpc) the ACS pixel scale corresponds to ~ 1 pc.

Besides NGC 1313, which has three different fields observed, the rest of the galaxies were covered using two pointings (see Fig. 3.1). The bands used for the observations were F336W(~ U), F435W(~ B), F555W(~ V), and F814W(~ I), with the exposure times listed in Table 3.2. The standard STScI pipeline was used for the initial data processing. ACS images were drizzled using the multidrizzle task (Koekemoer et al. 2002) in the STSDAS package in IRAF using the default parameters, but disabling the automatic sky subtraction. WFPC2 images were combined and corrected for cosmic rays using the *crrej* task using the default parameters.

Object detection for field stars and star clusters was performed on an average B, V, and I image, using *daofind* in IRAF for the stars and SExtractor V2.5.0 (Bertin & Arnouts 1996) for the clusters. Coordinate transformations between ACS and WFPC2 used IRAF. For details we refer to Paper I.

3.4. Photometry

We review here the procedures for carrying out photometry on our data, however, for details, we refer to Paper I. Due to the crowding we performed PSF photometry for field stars, while we used aperture photometry for the star clusters.

3.4.1. Field stars

With a set of bona-fide stars visually selected in our images, measuring their FWHM with *imexam*, we constructed our point-spread function (PSF) using the PSF task in DAOPHOT. This procedure was followed in the same manner for each band (i.e., B,V, and I). The PSF stars were selected individually in each band, in order to appear bright and isolated. PSF photometry was done with DAOPHOT in IRAF.

HST zeropoints[2] were applied to the PSF magnitudes after applying aperture corrections (see Sect. 3.4.3). The zeropoints used in this work are $ZP_B = 25.767$, $ZP_V = 25.727$ and $ZP_I = 25.520$ magnitudes. Typical errors of our photometry do not change dramatically from the ones in Paper I (see its Fig. 2).

Having magnitudes for our field stars, Hess diagrams were constructed and are depicted in Fig. 3.2 (each panel presents all fields combined for each galaxy). The total number of stars varies among the galaxies, all having some tens of thousands. Various phases of stellar evolution can be identified in the Hess diagrams:

- main sequence and possible blue He-core burning stars at $V - I \sim 0$ and $-2 \leq V \leq -8$;
- red He core burning stars at $1.2 \leq V - I \leq 2.5$ and $-2.5 \leq V \leq -6.5$;
- RGB/AGB stars, near the detection limit at $1 \leq V - I \leq 3$ and $-0.5 \leq V \leq -2.5$.

The same features were observed for NGC 4395 in Paper I.

Overplotted in Fig. 3.2 are the 50% completeness lines (see Sect. 3.4.5 for details of the completeness analysis). Also, red lines enclose the fitted areas that will be used in Sect. 3.5 to estimate the star formation histories of the galaxies. These areas were selected to cover regions that were clearly over the 50% completeness and represent stars in different stages of evolution (e.g. main sequence, red He core burning).

3.4.2. Star clusters

To detect the cluster candidates we used SExtractor with a detection criterion of six connected pixels and a threshold of 10 sigma above the background level. The total numbers of objects detected in each galaxy are listed in the second column of Table 3.3. For these objects aperture photometry was performed using an aperture radius of six pixels on our ACS pointings, corresponding to about two half-light radii for a typical star cluster. We used a sky annulus with five pixels width and an inner radius of eight pixels. For the WFPC2 images, the apertures used cover the same area. There is a possibility of having close-neighbor objects that contaminate the photometry, whether inside either of the aperture radii or the sky annulus. Sizes were measured using the ISHAPE task in the BAOLAB package (Larsen 1999).

As mentioned in Paper I, three criteria were used to produce catalogs of cluster candidates from the initial SExtractor output.

[2] www.stsci.edu/hst/acs/analisys/zeropints/#tablestart

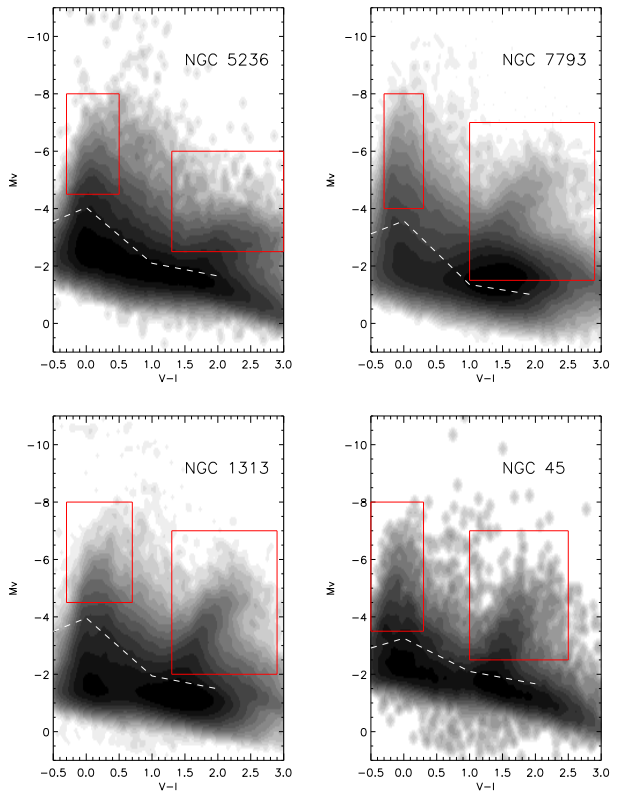

Figure 3.2: Hess diagram for the field stars of the observed galaxies. The dashed white line represents the 50% completeness curve. Red lines enclose the fitted areas used to estimate the SFH (see Sect. 3.5).

1. *Size*: Candidates must satisfy $FWHM_{\rm SExtractor} \geq 2.7$ pixels and $FWHM_{\rm ishape} \geq 0.7$ pixels. These are rather conservative size cuts that may eliminate some of the most compact clusters, but reduce the risk of contamination from other sources.

2. *Color*: Candidates must satisfy $V - I \leq 1.5$.

3. *Magnitude*: Candidates must be brighter than $m_V = 23$ (M_V brighter than -4.6 to -5.4, depending on the galaxy distance).

Since the WFPC2 fields only cover about half the area of the ACS fields, some objects will only have three-band photometry (*BVI*), while others will have all four colors. Objects that satisfy the three criteria listed above are considered as star cluster candidates in the rest of the paper. However, as found in many previous studies, there is no unique combination of objective criteria that can lead to a successful detection

Table 3.3: Number of clusters detected per field, per galaxy. Clusters with measured sizes (2^{nd} column), total of objects with three band photometry(3^{rd} column), accepted (4^{th} and 5^{th} columns), suspected (6^{th} and 7^{th} columns), and total rejected (8^{th} column). Subscripts 3B and 4B represent three and four band photometry. Shaded areas indicate the total per galaxy.

Galaxy_F	Ishape	T_{3B}	A_{3B}	A_{4B}	S_{3B}	S_{4B}	R_{total}
NGC 5236_F1	9788	1027	286	117	519	255	222
NGC 5236_F2	7290	758	274	85	326	123	158
NGC 5236	17078	1785	560	202	845	378	380
NGC 7793_F1	12095	521	83	41	308	150	130
NGC 7793_F2	13597	274	72	34	95	24	107
NGC 7793	25692	795	155	75	403	174	237
NGC 1313_F1	19925	1033	184	70	288	79	561
NGC 1313_F2	13153	751	164	52	115	15	472
NGC 1313_F3	12287	133	57	28	7	2	69
NGC 1313	45365	1917	405	150	410	96	1102
NGC 45_F1	3760	46	22	12	2	1	22
NGC 45_F2	4634	92	45	23	11	5	36
NGC 45	8394	138	67	35	13	6	58

of bona-fide clusters and no false detections. Our cluster candidates were therefore visually inspected to determine whether they resemble star clusters. Based on this, we classified the cluster candidates into three categories: Accepted, Suspected, and Rejected. Figure 3.3 presents some examples of each category. In this figure, the first row presents the Accepted objects, which are clearly extended objects with normal measured sizes and magnitudes. The second row presents the Suspected objects, where the size/magnitude measurements may be affected by crowding, where the shape appears irregular, or where the contrast against the background is not strong. The last (third) row presents examples of the Rejected objects.

Table 3.3 summarizes the total number of objects detected that have size measurements (2^{nd} column), the total number of objects with three-band photometry and have sizes over the limits imposed (3^{rd} column), the total number of accepted objects with three- and four band photometry (4^{th} and 5^{th} columns), the total number of suspected objects with three- and four band photometry (6^{th} and 7^{th} columns), and the total number of rejected objects (8^{th} column). Shaded areas are the total numbers per galaxy.

Figure 3.4 shows two-color diagrams for accepted plus suspected clusters with four band photometry (all the fields combined per galaxy), corrected for foreground extinction with the values presented in Table 3.1. Overplotted is a theoretical track that a cluster will follow between 4 Myr and 1 Gyr using Galev models (Anders & Fritze-v. Alvensleben 2003), assuming LMC metallicity and no extinction. We see that the clusters generally tend to align with the model sequence, but with significant scatter around it. Below we investigate to what extent this scatter may come from

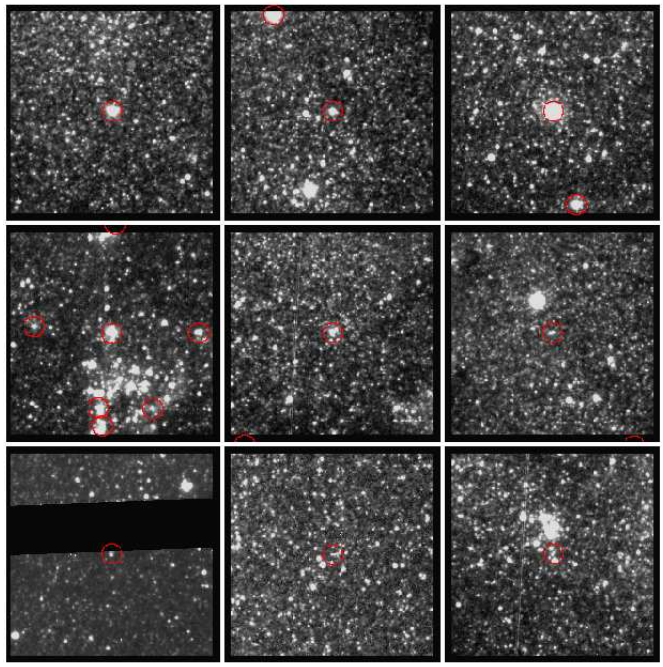

Figure 3.3: Examples of objects that were accepted (first row), suspected (second row), and rejected (third row) after visual inspection. Stamps are from the first field observed in NGC 7793 and have sizes of 100×100 pixels.

stochastic color variations due to random sampling of the stellar IMF.

3.4.3. Completeness

Completeness analysis was carried out separately for field stars and star clusters to account for both populations.

Field stars

As in Paper I, we created artificial stars using the PSF obtained in Sect. 3.4.1. In the magnitude range between 20 to 28, every 0.5 magnitudes, we generated 5 images and passed each one through the photometry procedures, using the exact same parameters as are used for the original photometry. A total of 528 stars were added to each image, with a separation of 100 pixels (we did not take subpixels shifts into account). The images were created using *mksynth* in BAOLab (Larsen 1999) and added to the science images using *imarith* in IRAF. To quantify the dependency of

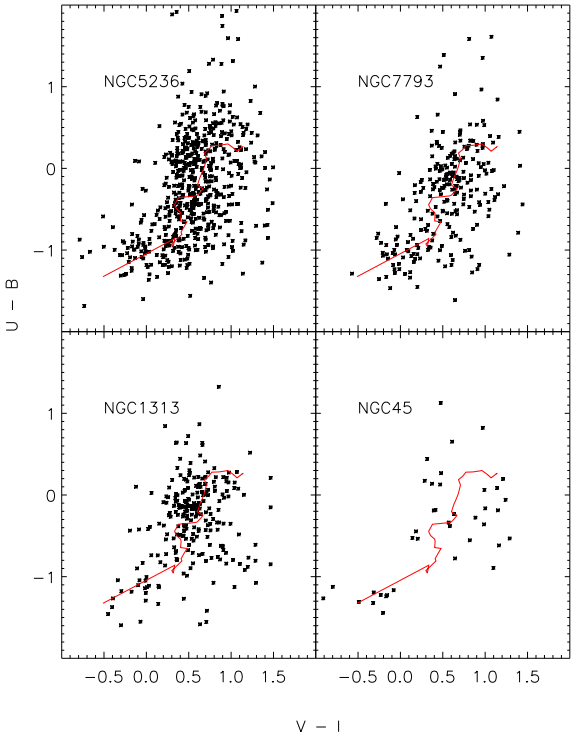

Figure 3.4: Two-color diagrams for the clusters with four band photometry. The red line represents the theoretical path a cluster will follow using GALEV models, assuming LMC metallicity and no extinction. Accepted+ Suspected clusters are presented.

completeness functions on color, we made use of the near 1:1 relation between the $B-V$ and $V-I$ colors of stars (see Paper I for details).

Based on our analysis, we found 50% completeness limits for each galaxy and for each band, as shown in Table 3.4.

Star clusters

In order to quantify completeness limits we added artificial clusters of different ages and masses to our images. We created artificial clusters using a stochastic approach. Assuming a Kroupa IMF (Kroupa 2002) in the mass range 0.01 to 100 $M_\odot$, a total cluster mass of $M = [10^3, 10^4, 10^5]$ $M_\odot$, and a cluster age range between $\tau = [10^7, 10^{9.5}]$ yr (with 0.5 dex steps), we randomly sampled stars from the IMF until the total mass of the stars reached the total mass assumed for the cluster.

Table 3.4: 50 % completeness limits for field stars.

Galaxy	Field	F435W(B)	F555W(V)	F814W(I)
NGC 5236	1	26.12	26.10	25.10
NGC 5236	2	26.48	26.35	25.48
NGC 7793	1	26.60	26.52	25.25
NGC 7793	2	26.91	26.78	26.03
NGC 1313	1	26.64	26.66	26.15
NGC 1313	2	26.65	26.55	26.14
NGC 1313	3	26.79	26.78	26.41
NGC 45	1	26.77	26.74	26.28
NGC 45	2	26.67	26.60	26.08

Positions were assigned by randomly sampling a King profile (King 1962). There is a possible pitfall regarding the mass of the last star sampled, because it could overcome the total input (assumed) mass. We kept the last star, even if the total mass is higher than assumed. This problem affects low-mass clusters more than high-mass clusters. With the ages and masses for the stars, we then interpolated in isochrones (of LMC-like metallicity) from the Padova group (Marigo et al. 2008) and assigned magnitudes to each star. For all the artificial clusters, an $FWHM = 2.7$ pixels was assumed (corresponding to a $R_{\rm eff} \approx 4$ pc). Figure 3.5 shows stamps of artificial clusters of different ages and masses, using an average (B, V, and I) image of the galaxy NGC 7793 as an example.

For each combination of age and mass, a total of 100 randomly generated clusters were added to the science images using a square grid. The artificial images with clusters were created using *mksynth* in BAOLab (Larsen 1999) and added to the science images using *imarith* in IRAF. Following the same procedure used for the cluster photometry, an average *BVI* image was created for each field. SExtractor was then run on this average image, using the same parameters as in Sect. 3.4.2. SExtractor returns a file with coordinates, measured FWHM and other information. To save computational time, owing to the large amount of objects that SExtractor could detect, we removed all the original objects (science objects detected previously) from the list and kept the ones that are not in the original image. This new coordinate file was passed to *ishape* in BAOLab to compute PSF-corrected sizes. We used the coordinate file to run photometry, again with the same procedures and parameters as for the science photometry. Having B, V, I photometry done, size cuts were applied and the output file was matched with the input coordinate file to evaluate how many of the added artificial objects were recovered successfully.

Figure 3.6 shows the output (m_V) average magnitude of the recovered clusters versus the fraction recovered for the three masses and six ages assumed in each galaxy. For the masses log(M)[$M_\odot$]=[3,4,5] as an illustrative example, Fig. 3.6 shows the total number of objects detected applying three different size criteria: (1.) $FWHM_{ishape} > 0$, i.e. no size cut used to select the clusters; (2.) $FWHM_{ishape} \geq 0.2$, same size cut used

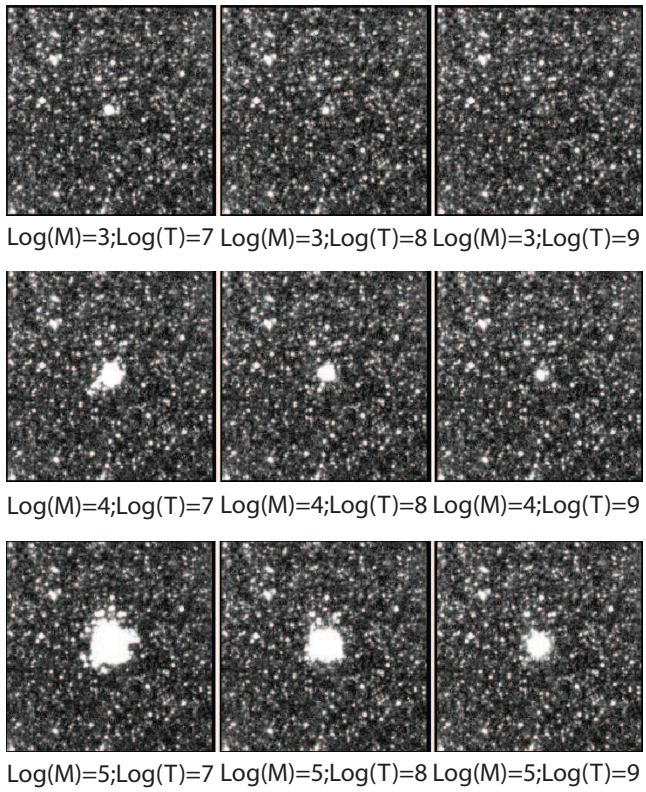

Figure 3.5: Stochastic clusters created to estimate the completeness in NGC 7793 (average B, V, and I image, first field). From top to bottom, rows represent masses of log(M)[$M_\odot$]=[3,4,5]. From left to right, columns represent ages of log(τ)[yr]=[7,8,9]. Each images has a size of 100×100 pixels.

by Mora et al. (2007, 2009); and (3.) $FWHM_{ishape} \geq 0.7$, the size cut used in this paper. Each line is for a given cluster mass, while each symbol belonging to a line represents the time steps assumed, i.e., $\tau = [10^7, 10^{9.5}]$ yr (with 0.5 dex step). From this test we conclude that

1. High-mass clusters (log(M)[$M_\odot$]=5), at any age, are easily recognized by our procedures, regardless of the size criteria used.

2. For decreasing cluster mass, clusters of old ages drop out of the sample, and for log(τ)[yr]≥8.5 our completeness is less than 50% for masses below log(M)[$M_\odot$]=4.

3. The completeness depends on the mass, on the size used to classify an object as extended or not extended, and on age. Decreasing the size threshold would

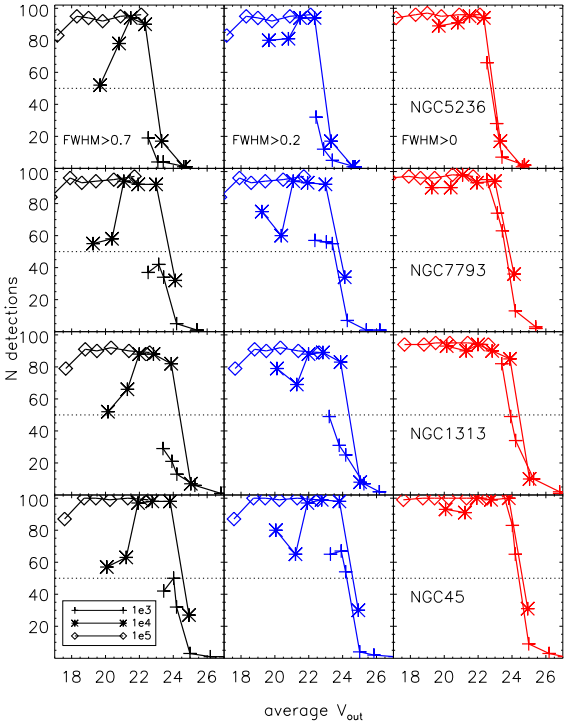

Figure 3.6: Completeness curves for stochastic clusters with ages log(τ)[yr]=[7,7.5,8,8.5,9,9.5] and masses of log(M)[$M_\odot$]=[3,4,5] for the four galaxies. All clusters have an input FWHM=2.7 pixels. Red lines represent the number of detections without applying any size criteria (right column). Blue lines are the number of detections after applying the size criteria of $FWHM_{ishape} \geq 0.2$ pixels, used in Mora et al. (2007, 2009) (middle column). Black lines are the number of detections after applying the size criteria used in this work ($FWHM_{ishape} \geq 0.7$ pixels) (left column). The legend is in units of solar masses ($M_\odot$). The symbols over the lines represent an age step (i.e. 0.5 dex) starting from the left.

increase the completeness somewhat for low-mass, young objects, but could introduce additional contamination.

4. Stochasticity affects young star clusters (log(τ)[yr]$\leq$7.5) more dramatically.

At the very young ages in Fig. 3.6 the completeness drops below 100% at all masses. This can be understood from Fig. 3.7, which shows the histograms for the FWHM of the detected objects measured with *ishape* for log(M)[$M_\odot$]=[3,4,5] and log(τ)[yr]=[7,8,9], using the results from NGC 7793 as an example. The figure shows

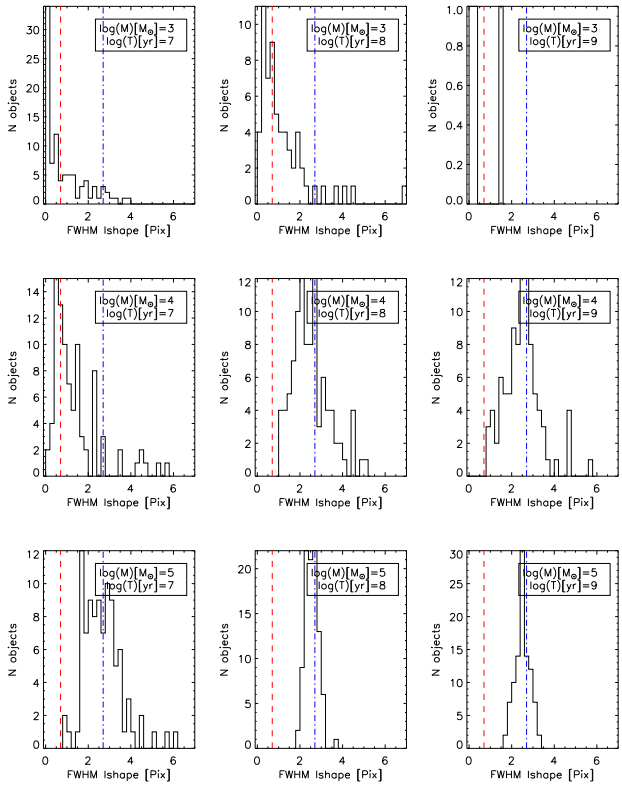

Figure 3.7: Histograms of measured FWHMs for the stochastic clusters in NGC 7793 created for the completeness analysis. From top to bottom, rows represent masses of log(M)[$M_\odot$]=[3,4,5]. From left to right, columns represent ages of log(τ)[yr]=[7,8,9]. Legends are in logarithmic mass and age units. The red dashed line represents an FWHM=0.7 pixels, as assumed in Sect. 3.4.3, while the blue dash-dotted line represents the input FWHM=2.7 pixels.

that at high masses and old ages, the recovered sizes are on average similar to the input values, with some spread. However, at younger ages and/or lower masses, the measured sizes are systematically less than the input values. In these cases, the light profiles can be dominated by a single or a few bright stars, while for high masses and/or old ages, the light profiles are much smoother and better fit by the assumed analytic profiles. At young ages and low masses, this bias in the size measurements leads to a decrease in the completeness fraction as more clusters fall below the size cut.

3.4.4. Aperture corrections

Aperture corrections were estimated separately for star and clusters. We applied the same procedures as in Paper I. For field stars, our PSF-fitting magnitudes were corrected to a nominal aperture radius of 0″5, following standard procedures. From this nominal value to infinity, we applied the corrections in Sirianni et al. (2005).

For star clusters, aperture corrections were applied following the equations in Mora et al. (2009), which give a relation between the FWHM of the objects and the aperture corrections. The photometric parameters (and data set) used in our work are the same as the ones used by Mora et al. (2009), allowing us to use their equations. This set of equations apply corrections to a nominal radius of 1″45. We adopted the values in Sirianni et al. (2005) to correct from there on, although the corrections to infinity are minor ($\sim$ 97% of the total energy is encircled within 1″5).

3.4.5. How do stochastic effects influence star cluster photometry?

The classical approach used to estimate masses and ages of unresolved star clusters in the extragalactic field is based on the use of multi-band integrated colors and comparison of these with SSP models. Anders et al. (2004) show that it is necessary to have at least four-band photometry to be able to break degeneracies (e.g. age-metallicity). However, standard SSP models assume a continuously populated stellar initial mass function (SIMF), while clusters consist of a finite number of stars. For unresolved clusters, the random sampling of the SIMF can strongly affect integrated properties such as cluster colors, magnitudes, and parameters (ages, masses) derived from them (Cerviño & Luridiana 2006, Maíz Apellániz 2009, Popescu & Hanson 2010a,b). A promising attempt to take the stochastic color fluctuations into account when deriving ages and masses has been made by Fouesneau & Lançon (2010), based on a Bayesian approach.

Here we do not attempt to offer any solution to the SIMF sampling problem, but we quantify its effects that are related to our study. To that aim, we created clusters by randomly sampling the SIMF and assigning magnitudes to individual stars in the same bands used for our photometry (i.e. U, B, V, and I). In addition to its impact on cluster detection and classification, as described in the previous section, we also investigated how stochastic SIMF sampling affects the two-color diagrams and ages.

We used the same recipe as in Sect. 3.4.3 to create artificial clusters. Assuming a range of ages between $10^{6.6}$ Myr and $10^{9.5}$ yr and total masses of M=[10^2, 10^3, 10^4, 10^5, 10^6] $M_\odot$, we created 100 clusters every 0.1 dex in age. The top row in Fig. 3.8 shows the two-color diagrams for each one of the total masses, together with an LMC-metallicity Padova SSP model (Marigo et al. 2008). The evolution of the colors U-B and V-I with time are shown in the second and third rows, and the comparison of input (assumed) and output (estimated) ages using AnalySED (Anders et al. 2004) are in the bottom row. The colors indicate the input ages.

Many features are observed here. (1.) For high masses (log(Mass)[$M_\odot$]=[5,6]), the stochastically sampled clusters form narrow sequences in the color-color and color-

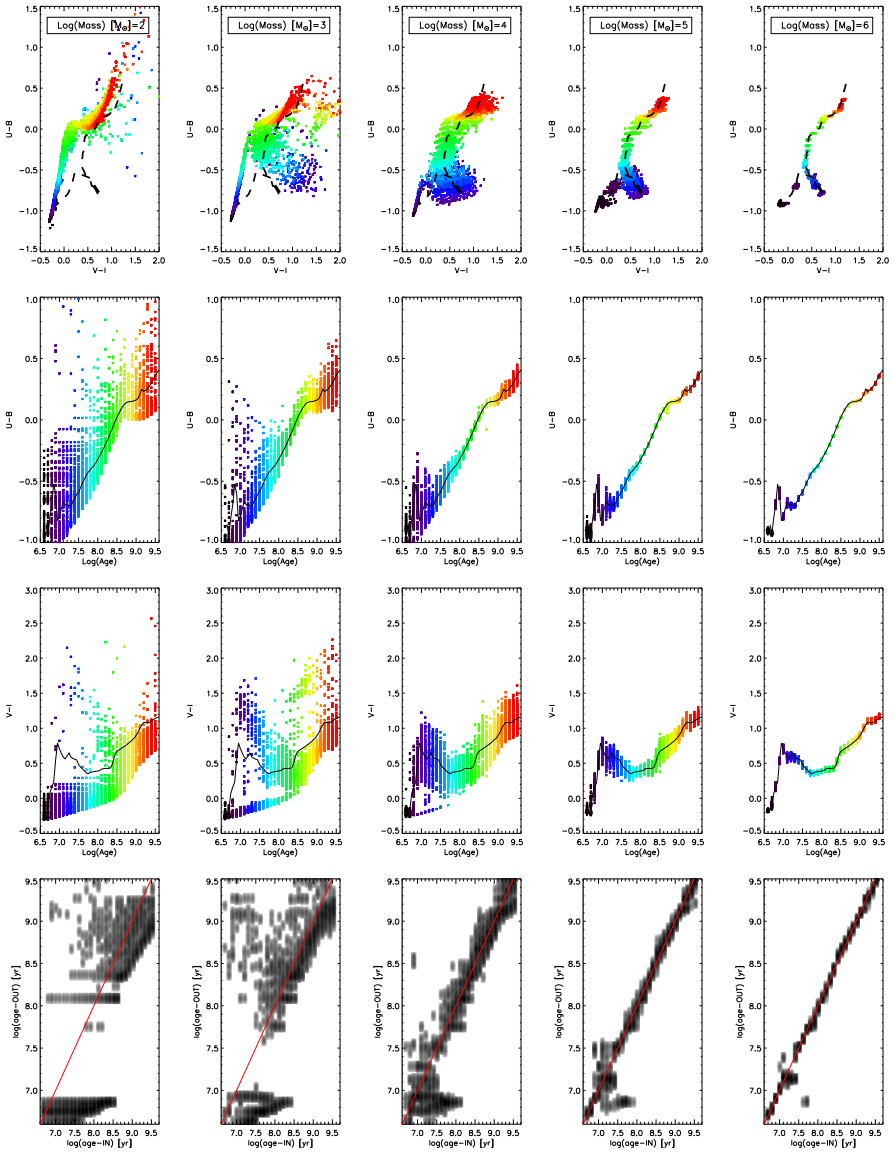

Figure 3.8: Stochastic effects on colors and ages of clusters. *First row*: Two color diagrams for a stochastic sample of clusters with different masses and different ages. The dashed line represents Padova 2008 SSP models of LMC-like metallicity. *Second row*: U-B color evolution. *Third row*: V-I color evolution. *Fourth row*: Density plot to make a comparison between input and output ages. The red line represents the 1:1 relation, not a fit to the data.

age diagrams, in agreement with Cerviño & Luridiana (2006). (2.) At intermediate masses, i.e., log(Mass)[$M_\odot$]=[3,4], which are typical of the cluster masses observed in extragalactic works, the scatter increases strongly. The scatter observed in the two-color diagrams for this mass range is similar to what is seen in our observed two-color diagrams. (3.) For very low masses (log(Mass)[$M_\odot$]=[2]), the scatter again decreases but the model colors now deviate strongly from the SSP colors. This is because such clusters have a very low probability of hosting a luminous (but rare and short-lived) post-main sequence star, while the SSP models assume that the colors are an average over all stages of stellar evolution (see Piskunov et al. 2009). (4.) For ages $\log(\tau) \lesssim 8$ and intermediate masses (log(Mass)[$M_\odot$]=[3,4]), the color distribution actually becomes bimodal, as observed by Popescu & Hanson (2010a,b). The blue "peak" in the color distribution is due to clusters without red supergiants, while the presence of even a single red supergiant shifts the colors into the other peak. (5.) The bottom row shows that age estimates are completely dominated by stochastic effects for low-mass clusters (log(Mass)[$M_\odot$]=[2,3]). For higher masses the ages are more accurately recovered, even if a small scatter is observed compared to the 1:1 relation, especially at ages of a few tens of Myr where the light is strongly dominated by red supergiant stars.

Based on these results it is clear that photometry and the ages estimated from broad band photometry can be heavily affected by the stochastic effects introduced by SIMF sampling, as also shown by Maíz Apellániz (2009). We conclude that low-mass clusters ($M \leq 10^3 M_\odot$) are very strongly affected, reaching age differences up to $\log(age_{in})$-$\log(age_{out}) \approx 2.5$ dex, for clusters with $\log(\tau)[yr] \leq 8.5$, while for high-mass clusters ($M \geq 10^4 M_\odot$), this effect gradually diminishes, an effect that is clearly visible as gaps in Fig. 3.8 (last row). Another important effect is observed as a deviation from the 1:1 red line observed for the low-mass clusters, which indicate that the estimated age (Age_{out}) is again wrongly recovered, even at old ages (1 Gyr). One should be aware of the risk that low-mass, young clusters may erroneously be assigned old ages. When using SSP models to convert their luminosities to masses, based on such wrong age estimates, such objects might be assigned erroneously high masses, thus making it into an observed sample (e.g. Popescu & Hanson 2010b).

It is important to mention that the SSP models used do not take the binarity or rotation of massive stars into account (see e.g. Maeder & Meynet 2008, Eldridge & Stanway 2009). Also, different isochrone assumptions and the techniques used to perform the fit to the ages and masses can be affecting the results (see e.g Scheepmaker et al. 2009, de Grijs et al. 2005). The tests presented in this paper are only intended to address the stochastic sampling effects, and we only rely on Padova isochrones. A more detailed study must be made to better account for other effects (e.g. by binaries, rotation, etc).

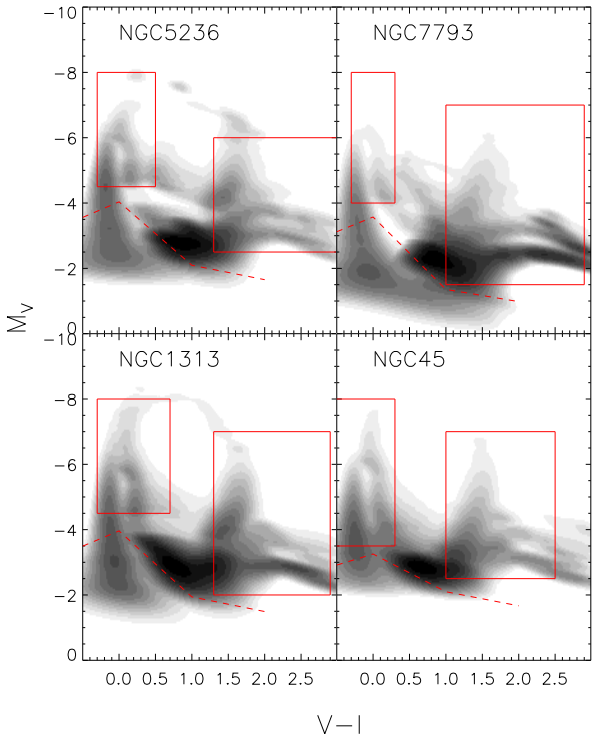

Figure 3.9: Fitted Hess diagrams for the sample studied. Red lines are the boxes used for the fit and the 50% completeness, same as Fig. 3.2.

3.5. Results

In the next sections we estimate the field star formation histories (SFHs) for each galaxy and determine the ages and masses of the cluster candidates. We then estimate the cluster formation efficiencies, Γ.

3.5.1. Field star formation histories

To estimate the SFHs, we used the synthetic CMD method. We implemented this method using an IDL-based program that was introduced and tested in Paper I. For a description of the program we refer the reader to that paper, but here we summarize the basic functionality.

The synthetic CMD method (Tosi et al. 1991) takes advantage of the power supplied by the CMDs. The method uses a group of isochrones, together with assump-

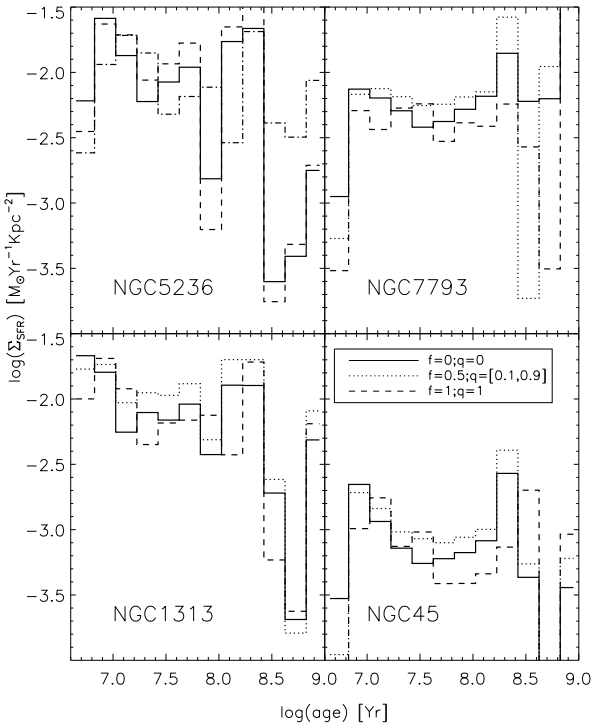

Figure 3.10: Star formation rate densities for the data set. Each line represent an assumption for the binarity (see text for details).

tions about the SIMF, metallicity, distance, extinction, and binarity, to reproduce an observed CMD. Photometric errors and completeness functions (both being treated as magnitude dependent parameters by our program) are also taken into account. The program searches for the combination of isochrones that best matches the observed CMD, thereby estimating the SFH.

The parameters used to estimate the SFH of the galaxies are: a Hess diagram with a resolution of 200 × 200 pixels is created, using a Gaussian kernel with a standard deviation of 0.02 magnitudes along the color axis. The matching is done within the rectangular boxes depicted in Fig. 3.2, using the V-I vs. V color combination, Padova 2008 isochrones (Marigo et al. 2008) and a Kroupa (2002) IMF in the mass range 0.1 to 100 $M_{\odot}$. The assumed distance moduli, foreground extinctions, and metallicities are given in Table 3.1, while the photometric errors and completeness for each galaxy were determined in Sect. 3.4. The program also includes a simplified treatment of binaries, in which binary evolution is ignored, but the effect of unresolved binaries on

the CMD are modeled. To account for binarity we used three different assumptions for the binary fraction (f) and mass ratio (q): (1.) $f = 0.0$ and $q = 0.0$, (2.) $f = 0.5$ and $q = [0.1, 0.9]$ (assuming a flat distribution), and (3.) $f = 1$ and $q = 1$. These three assumptions are the same ones as used in Paper I.

Figures 3.9 shows the best-fit Hess diagrams. Comparing with the observed Hess diagrams (Fig. 3.2), we see that the fits are far from perfect. In particular, all the model Hess diagrams show a clear separation between the blue core He burning ("blue loop") stars and the main sequence, while this is not obvious in most of the observed diagrams. This might be partly due to some variation in the internal extinction, which has not been included in our modeling. To infer the SFHs of our sample, we combined all the fields (per galaxy) and passed to our program. The star formation rates, normalized to unit area, are shown in Figure 3.10 and the average values are listed in Table 3.5 for ages between 10 and 100 Myrs. In this age range, our data are less affected by incompleteness. Previous estimates of the $\Sigma_{\rm SFR}$ done by Larsen & Richtler (2000) and Calzetti et al. (2010) are included in table 3.5. We see that NGC 5236 and NGC 1313 have higher $\Sigma_{\rm SFR}$ values than with NGC 7793 and NGC 45, in agreement with the previous estimates. Within the uncertainties (see Paper I), we do not see any significant trends in the SFRs between 10^7 and 10^8 years. While our estimate of $\Sigma_{\rm SFR}$ agrees very well with the others for NGC 5236, there are significant differences for some of the other galaxies, most notably for NGC 4395. It should be kept in mind that the $\Sigma_{\rm SFR}$ values derived here are for our specific ACS fields, while the others are averages over whole galaxies over a rather large outer diameter. It is therefore not very surprising that our new estimates tend to be higher.

Table 3.5: Estimates of the star formation rates.

Galaxy	SFR†	Areas†	$\Sigma^{\dagger}_{sfr}$	$\Sigma^{\ddagger}_{sfr}$	Σ^{a}_{sfr}
	[$M_{\odot}yr^{-1}$]	[Kpc^2]	[$M_{\odot}yr^{-1}Kpc^{-2}$]	[$M_{\odot}yr^{-1}Kpc^{-2}$]	[$M_{\odot}yr^{-1}Kpc^{-2}$]
NGC5236	0.39	28.71	13.43×10^{-3}	13.8×10^{-3}	16.8×10^{-3}
NGC7793	0.15	23.05	6.43×10^{-3}	2.12×10^{-3}	2.8×10^{-3}
NGC1313	0.68	60	11.26×10^{-3}	4.04×10^{-3}	—
NGC45	0.05	48.99	1.01×10^{-3}	0.23×10^{-3}	—
NGC4395^{b}	0.17	36.48	4.66×10^{-3}	0.25×10^{-3}	—

†estimated in this paper; ‡Larsen & Richtler (2000); ^{a}Calzetti et al. (2010); ^{b} values from Paper I.

3.5.2. Cluster ages and masses

To determine the ages and masses of the clusters we used the program AnalySED (Anders et al. 2004). Using GALEV SSP models (Schulz et al. 2002), AnalySED compares the observed spectral energy distributions with a library of models to find the best fit. We used GALEV models based on a Kroupa IMF (Kroupa 2002) in

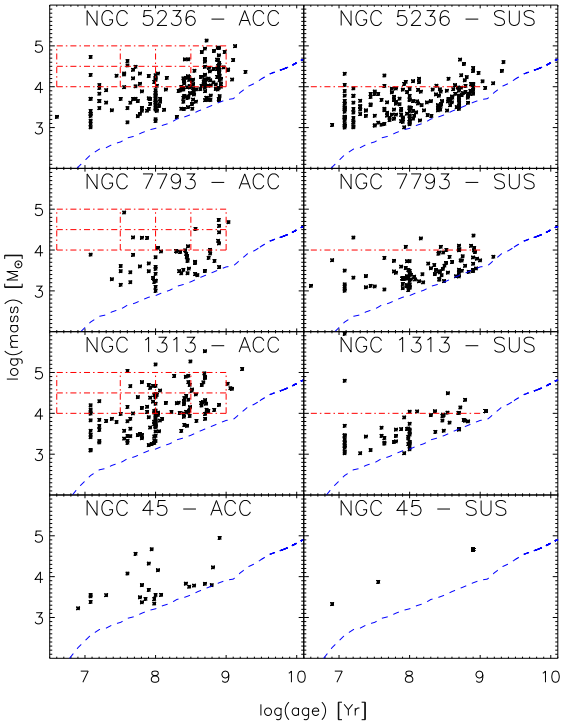

Figure 3.11: Age-mass distributions for the cluster systems. Blue dashed lines represent the magnitude cut at $m_v = 23$. Red boxes will be used to create the age and mass distributions. Left column present the distribution for the Accepted sample, while the right column present the suspected sample of clusters (see Sect. 3.4.2). Red dash-dotted line in the right column denotes the mass 10^4 $M_\odot$ for comparison.

the mass range 0.1 to 100 $M_\odot$, Padova isochrones (Girardi et al. 2002), and different metallicities, depending on the galaxy.

Based on our analysis of uncertainties due to stochasticity, we applied a mass criterion to the cluster samples in addition to the three selection criteria defined in Sect. 3.4. We require clusters in our sample to be more massive than 1000 $M_\odot$; however, we remind the reader that ages are only reliable for masses greater than 10^4 $M_\odot$ (for ages $\tau \leq 1$ Gyr). The magnitude limit, $M_V \sim -5$, is generally below our 50% detection limit based on the stochasticity test.

Figure 3.11 shows the age-mass diagrams for clusters that satisfy the four criteria for the accepted and suspected samples separated. Overall, we observe that the suspected clusters are below 10^4 $M_\odot$ (right column in the figure). We see that the

number of clusters in NGC 45 is small, compared with the other three galaxies. To first order, this appears to be consistent with the overall low star formation rate derived for this galaxy. Clusters in all four galaxies display a range in age and mass, but most are younger than 1 Gyr and have masses below 10^5 $M_\odot$, with few exceptions. We cannot exclude, however, that the sample contains some older clusters that have been assigned too young ages. In particular, relatively metal-poor old globulars would not be fit well by the models used here. Our sample includes two of the eight spectroscopically confirmed old globular clusters in NGC 45 from Mora et al. (2008). From these we find ages of 0.04 and 0.8 Gyr, while Mora et al. find spectroscopic average ages of 4.5 and 6.5 Gyr but consistent with ages as old as 10 Gyr. This confirms the suspicion that some of the clusters in our sample might be older, metal-poor globulars with misassigned ages.

Our catalogs of the cluster candidates are available online. Table 3.10 shows a few example lines to illustrate the format and the information contained in the catalogs.

3.5.3. Cluster disruption and formation efficiencies

Although we have derived masses and ages for our cluster candidates, some additional steps are necessary before we can use this information to derive cluster formation rates. In Paper I we used a Schechter (Schechter 1976) mass function ($M_\star = 2 \times 10^5$ $M_\odot$) to extrapolate below the (age-dependent) mass limit and in this way we estimated the total mass in clusters with ages between 10^7 and 10^8 years for NGC 4395. This approach ignores any effects of disruption but is still useful for relative comparisons. We therefore first apply the same approach to the four galaxies in this paper. Completeness limits were estimated by plotting the luminosity functions and identifying the point where they start to deviate significantly from a smooth power law. This occurs at the following absolute magnitudes: $M_V = -6.2$ for NGC 5236, $M_V = -5.7$ for NGC 7793, $M_V = -6.8$ for NGC 1313, and $M_V = -5.9$ for NGC 45. After estimating the mass in clusters with $10^7 < \tau/\mathrm{yr} < 10^8$ down to a limit of 10 $M_\odot$ and dividing by the age interval (see Paper I for details), the resulting CFRs were normalized to the area of the full ACS fields (a factor of ~ 2.27 more) for comparison with the field star formation rates. The resulting CFRs are listed in the second column of Table 3.8 ($\mathrm{CFR_{P1}}$).

Especially for NGC 45, the CFRs derived in this way are highly uncertain owing to the small number of clusters that have four-band photometry. Better statistics can be obtained by only using the three-band photometry in the ACS frames, but at the cost of having no age information for individual clusters. However, CFRs may still be estimated by comparing the observed *luminosity functions* (LFs) with scaled model LFs (Gieles 2010). If the CFR is assumed constant and assumptions made about the initial cluster mass function (Ψ) and disruption parameters, the LF can be modeled as follows (Eq. 7 in Larsen 2009):

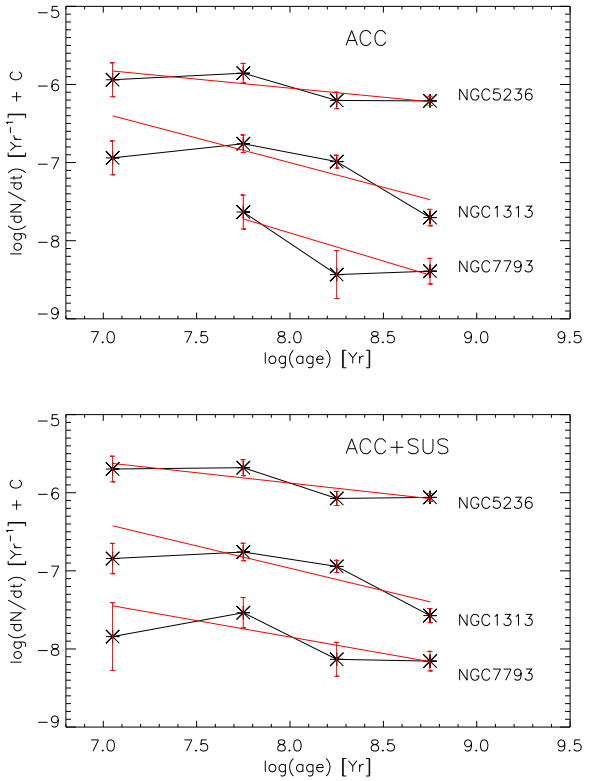

Figure 3.12: Age distributions for clusters in the galaxies NGC 5236, NGC 7793, and NGC 1313 in the mass range 10^4 to 10^5 $M_\odot$. Black lines represent the distributions for galaxies. Red lines represent the best fit. Upper panel are the ADs only using the clusters classified as accepted. The lower panel are the ADs for the clusters classified as accepted plus suspected.

$$\frac{dN}{dL} = \int_{\tau_{min}}^{\tau_{max}} \Psi_i[M_i(L,\tau)] \times \frac{dM_i}{dM_c} \times \Upsilon_c(\tau) \times \mathrm{CFR} \times f_{\mathrm{surv}}(\tau)\, d\tau\,, \tag{3.1}$$

where $\Psi_i[M_i(L,\tau)]$ is the initial mass function; $\Upsilon_c(\tau)$ is the mass-to-light ratio, which is only dependent on time in order to be able to compute it from classical SSP models; CFR is assumed constant over time; and $f_{\mathrm{surv}}(\tau)$ is the number of clusters that survive after applying MID; M_i and M_c are the initial and current masses of a cluster with luminosity L and age τ, and these are related through the assumed secular disruption law (Lamers et al. 2005). The description of MID adopted here assumes that a constant fraction of the cluster population is removed per logarithmic age bin, as opposed to a

Table 3.6: Slopes for the age distributions for the accepted and the accepted+suspected samples.

Mass [$M_\odot$]	NGC 5236	NGC 7793	NGC 1313
	Accepted		
$10^4 - 10^5$	-0.23±0.1	-0.72±0.27	-0.63±0.12
	Accepted+Suspected		
$10^4 - 10^5$	-0.26±0.08	-0.42±0.19	-0.57±0.11

constant fraction of the mass of each individual cluster. If Ψ_i is a uniform power law, this makes no difference. However, if the MID stem from gradual mass loss from individual clusters, any features in Ψ_i (such as the cut-off mass for the Schechter function) will be shifted downwards with time, whereas only the normalization of Ψ_i will change with time for constant number loss.

In order to apply Eq. (3.1), some constraints on cluster disruption are necessary. Models and empirical constraints on cluster disruption have been discussed in recent years by different authors (e.g. Boutloukos & Lamers 2003, Lamers et al. 2005, Whitmore et al. 2007, Larsen 2009, Zhang & Fall 1999, Fall 2004, among others), and Fall et al. (2009) for different types of galaxies such as the LMC, SMC, Milky Way, M83, or Antennae. Given that it is currently uncertain to what extent MID or MDD dominates the cluster disruption, we carried out our analysis for both scenarios.

Figure 3.12 shows the age distributions (ADs) for clusters with masses between 10^4 and 10^5 $M_\odot$ for the galaxies NGC 1313, NGC 5236, and NGC 7793. NGC 45 has too few clusters to derive meaningful ADs. We show fits for both the Accepted and Accepted+Suspected samples. The slopes of the age distributions, obtained by carrying out fits of the form $\log(dN/dt) = a \times \log(\tau) + b$ to the data in Fig. 3.12, are given in Table 3.6. There are no large differences between the slopes derived for the Accepted and Accepted+Suspected sample. Figure 3.11 shows that most of the clusters in the suspected sample have masses below our limit of $\log(M)$ [$M_\odot$] = 4.0, explaining the similarity of the age distributions above this limit.

As a consistency check for the slope of the age distributions, we performed a maximum likelihood fit to the data, assuming a power-law relation and using the power-law index as a free parameter. Using the accepted and accepted plus suspected sample of clusters, we estimated the slope of the age distributions using the same age and mass ranges as shown in Fig. 3.12 (i.e. ages between 4 Myrs up to 1 Gyr and masses between 10^4 and 10^5 $M_\odot$). The results obtained are presented in Table 3.7. The derived slopes agree very well with those in table 3.6, within the errors.

Using clusters with ages between $10^{6.6} \leq \tau \leq 10^8$ yr and a mass $10^4 \leq M \leq 10^5$ $M_\odot$ we checked for (possible) variations over the slope of the age distributions. The best fit for these slopes in the new age interval are -0.17 ± 0.39, -0.38 ± 2.34, and 0.78 ± 0.43 using the accepted sample, and -0.39 ± 0.31, 0.05 ± 0.91, and 0.59 ± 0.91 using the accepted plus suspected sample, for the galaxies NGC 5236, NGC 7793, and

Table 3.7: Slopes for the age distributions for the accepted and the accepted+suspected samples based on the maximum likelihood fit.

Mass [$M_\odot$]	NGC 5236	NGC 7793	NGC 1313
Accepted			
$10^4 - 10^5$	-0.27±0.11	-0.48±0.32	-0.63±0.10
Accepted+Suspected			
$10^4 - 10^5$	-0.31±0.09	-0.30±0.21	-0.60±0.09

NGC 1313 respectively. The new slopes are to be flatter than the values for the whole age range, showing even positive values; however, in most of the cases, the error is larger than the estimation itself. The possibility of having shallower slopes indicate that there is a possible curvature of the age distribution of star cluster systems, which is not consistent with a (simple) power law.

The slopes found here are, however, somewhat shallower than the value of $a = -0.9 \pm 0.2$ found for NGC 5236 by Chandar et al. (2010). If interpreted within the MID scenario, the slopes derived here correspond to MID disruption rates of 41%, 81%, and 77% per decade in age if we use the accepted sample, and 45%, 62%, and 73% if we use the sample of accepted plus suspected objects, for the galaxies NGC 5236, NGC 7793, and NGC 1313, respectively. A weighted average of the slopes for the Accepted samples leads to a mean slope of $\langle a \rangle = -0.42 \pm 0.07$ and an MID disruption rate of (62±6)% per decade in age. We use this mean weighted value for all the galaxies in our sample, including NGC 45 and NGC 4395 where the numbers of detected clusters are too low to allow us to estimate the slopes of the age distributions independently.

It is worth comparing our age distributions with those of Mora et al. (2009). Their slopes were considerably steeper than those found here, but this is partly because Mora et al. worked with magnitude-limited samples, while our age distributions are for mass-limited samples. When taking this into account, Mora et al. found that their data were consistent with MID disruption rates of 75%–85% per dex, still somewaht higher than the values found here. We note that the stochastic effects, combined with our relatively conservative size cuts, likely cause us to underestimate the number of objects in the youngest bins. This might account for some of the flattening of the age distributions in the youngest bins that is also seen in Fig. 3.12 for NGC 1313 and NGC 5236. For this reason our estimates of the slopes and disruption rates might also be considered lower limits. The less strict size cut used by Mora et al. (FWHM=0.2 pixels instead of our 0.7 pixels) would cause them to detect more compact, young objects, but also possibly ones with increased contamination. Finally, since visual selection was part of the sample selection in both our work and the one of Mora et al., this will also lead to differences in the final samples.

A key difference between the MID and MDD models is that, while the former predicts no change in the shape of the mass distribution with age, the latter predicts

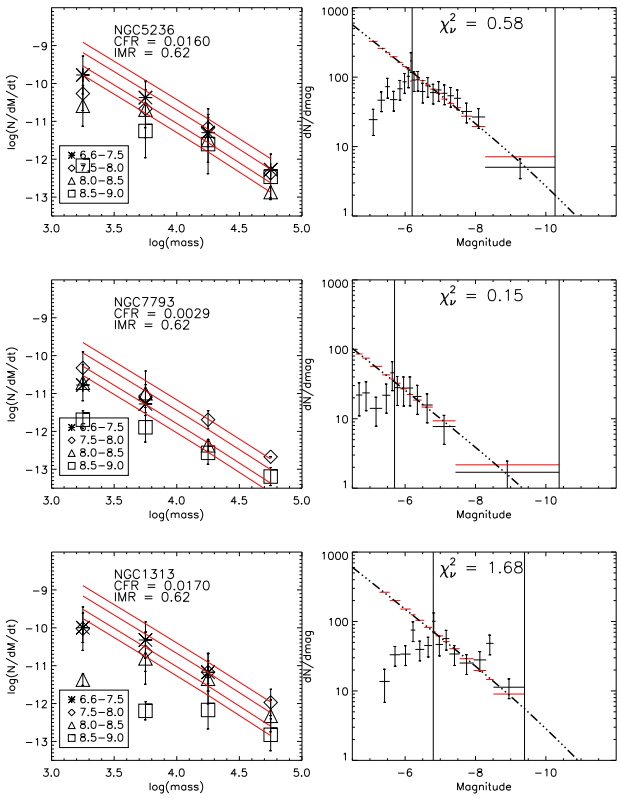

Figure 3.13: Mass-independent models. Left column: MDs observed (black symbols) and predicted models (red lines). Right column: Luminosity function observed (black horizontal lines), predicted models (red horizontal lines), and theoretical model (dash-dotted line). Vertical straight lines represent the limits used for the fit of the LFs.

a flattening at low masses. In order to test whether we can distinguish between the two scenarios, model mass distributions (MD, number of objects, per mass bin, per linear age bin) were computed for different age intervals using a relation analogous to Eq. 3.1, but integrating over τ for fixed M rather than fixed L. These model MDs were then compared with the observed MDs in the same age intervals. For the MDD scenario we assumed $\gamma = 0.62$ and a disruption time of $t_4 = 1 \times 10^9$ yr (Lamers et al. 2005). No infant mortality was included in the MDD models (i.e. $f_{\rm surv} = 1$ at all ages). The MID models used the IMR obtained above (62%), which is active in the age range 5 Myrs to 1 Gyr, and t_4 was set to infinity, making the models independent of mass. We compared the model MDs with our observations, dividing our cluster samples into the following age and mass bins: log(M)[$M_\odot$]=[3.0,3.5,4.0,4.5,5.0] and log(τ)[yr]=[6.6,7.5,8.0,8.5,9.0] (shown in Fig. 3.11).

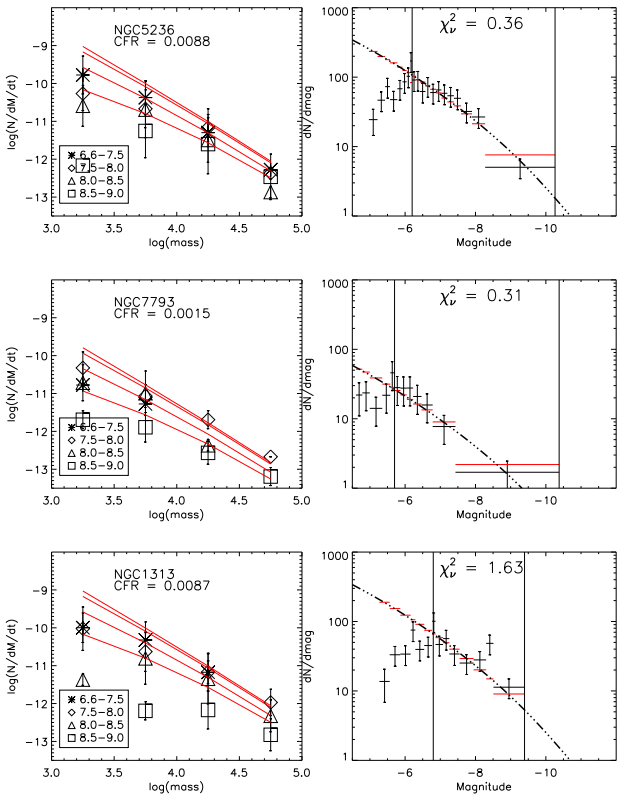

Figure 3.14: Mass-dependent models. Left column: MDs observed (black symbols) and predicted models (red lines). Right column: Luminosity function observed (black horizontal lines), predicted models (red horizontal lines), and theoretical model (dash-dotted line). Vertical straight lines represent the limits used for the fit of the LFs.

In Figs. 3.13 and 3.14 we compare the observed and predicted MD and LF for MID and MDD models. The best fits were defined by scaling the model LFs to match the observed ones, where the observed LFs were created using variable binning with ten objects per bin for NGC 1313 and NGC 5236 (following Maíz Apellániz (2009)) and five objects per bin for NGC 45, NGC 4395, and NGC 7793. Errors were assumed to be Poissonian. Also shown is the reduced χ^2 for each galaxy. Based on these figures, it is difficult to distinguish between the MID and MDD scenarios, mostly because of the limited dynamical range of the data and the poor statistics.

Our final estimates of the CFRs come from the LFs for clusters with 3-band photometry in all five galaxies in our sample, using model LFs computed for both MDD and MID disruption. The observed LFs were created in the same way as described above, using variable binning. We used the magnitude ranges up to the

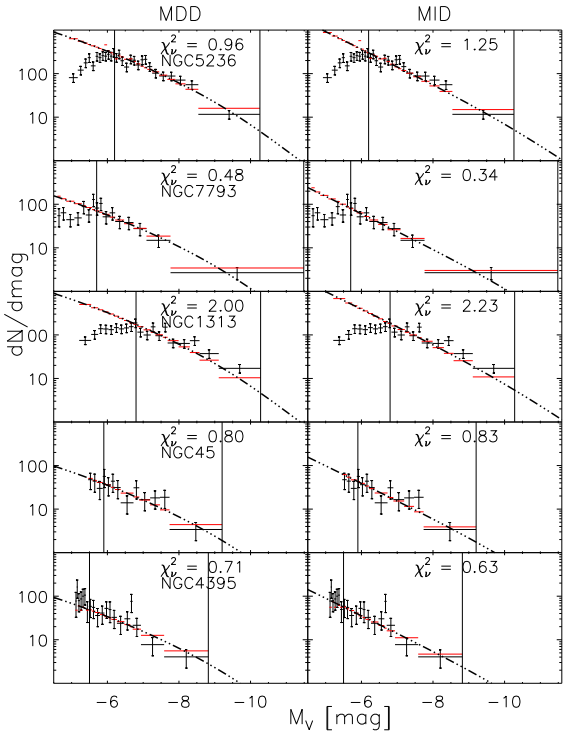

Figure 3.15: LFs for the five galaxies in our sample. We used MDD and MID theoretical models in left and right columns, respectively. Vertical lines are the limits of the fit. Red horizontal lines represent the binned theoretical values, while black horizontal lines represent observations. Errors are Poissoninan. Dashed-dotted line is the theoretical LF not binned.

brightest cluster in the sample and the lower limit was set at the completeness limits estimated above (see vertical lines in Fig. 15). The CFRs are listed in Table 7 for the 4- and 3 band photometry. The CFRs for the four-band photometry have been scaled to the size of the ACS elds. The observed LFs and the best-fitting models are shown in Fig. 3.15, where MID and MDD models have been tested for the five galaxies in our sample. The CFRs inferred from the fits in Fig 15 only include the accepted clusters. If we include the "suspected" objects then the CFRs increase by 52%, 62%, 30%, 4%, and 25% for NGC 5236, NGC 7793, NGC 1313, NGC 45 and NGC4395, respectively, for the MDD scenario. Similar changes occur for MID. Furthermore, if we exclude the known ancient GCs in NGC 45 (Mora et al. 2008) from the sample, the Γ value for this galaxy decreases by $\sim$ 20%. Taken together, this then makes NGC 45 less of an outlier in Fig. 3.16 and in general shifts the data points upwards.

Table 3.8: Estimates of the cluster formation rates. Subscript P1 refers to estimations made following Paper I. Disruption models are labeled as MDD and MID. Number of bands used for the estimation are labeled as 3B and 4B.

Galaxy	CFR_{P1} $[M_\odot yr^{-1}]$	CFR^{3B}_{MDD} $[M_\odot yr^{-1}]$	CFR^{4B}_{MDD} $[M_\odot yr^{-1}]$	CFR^{3B}_{MID} $[M_\odot yr^{-1}]$	CFR^{4B}_{MID} $[M_\odot yr^{-1}]$
NGC5236	37.7×10^{-3}	23.0×10^{-3}	19.9×10^{-3}	41.0×10^{-3}	36.6×10^{-3}
NGC7793	14.5×10^{-3}	4.0×10^{-3}	3.4×10^{-3}	6.8×10^{-3}	6.6×10^{-3}
NGC1313	60.7×10^{-3}	23.0×10^{-3}	19.7×10^{-3}	44.0×10^{-3}	38.6×10^{-3}
NGC45	8.6×10^{-3}	2.5×10^{-3}	2.7×10^{-3}	4.4×10^{-3}	3.6×10^{-3}
NGC4395	4.5×10^{-3}	2.4×10^{-3}	1.0×10^{-3}	4.0×10^{-3}	1.6×10^{-3}

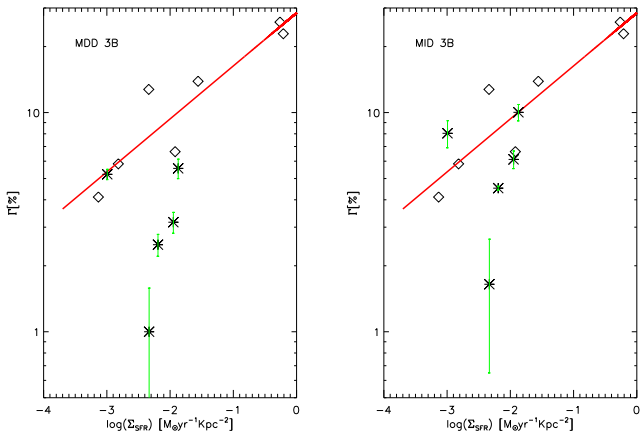

Figure 3.16: Relation between Γ and Σ_{SFR} using average values of Γ for the models MDD and MID. Rhombs symbols and line represents the Goddard et al. (2010) data and black star symbols represent our set of galaxies.

Having estimated the SFRs and CFRs, we are now able to calculate Γ. Table 3.9 lists the Γ values corresponding to the different estimates of the CFR. As an additional consistency check, we also include a direct comparison of the fraction of light coming from clusters and from field stars, using the magnitude range between m_V = 23 and m_V = 18. This is not a direct measure of Γ, but is still useful for checking any trends. The Γ values derived from the LF fitting are generally a few percent, with the values derived from MDD models about 48% smaller (or less) than those derived for the MID models. We computed the mean value for each model and the respective the standard error of the mean (columns 5th and 8th in Table 3.9).

Table 3.9: Estimations of Γ and comparison with Goddard et al. (2010) results.

Galaxy	Γ_{P1} [%]	Γ^{3B}_{MDD} [%]	Γ^{4B}_{MDD} [%]	$\Gamma_{MDD} \pm \sigma_{MDD}$ [%]	Γ^{3B}_{MID} [%]	Γ^{4B}_{MID} [%]	$\Gamma_{MID} \pm \sigma_{MID}$ [%]	$\Gamma^{\dagger}$ [%]	$T_L(U)^{\dagger}$	L_{CL}/L_{FS} [%]
NGC5236	9.8	5.9	5.2	5.6±0.6	10.5	9.4	10.0±0.9	10.3	2.36±0.31	9.0
NGC7793	9.8	2.6	2.3	2.5±0.3	4.5	4.5	4.5±0.1	8.6	1.15±0.32	3.4
NGC1313	9.0	3.3	2.9	3.2±0.2	6.4	5.7	6.1±0.6	9.9	1.49±0.44	11.7
NGC45	17.3	5.0	5.4	5.2±0.3	8.8	7.2	8.0±1.1	2.2	0.24±0.17	6.1
NGC4395	2.6	1.4	0.6	1.0±0.6	2.3	0.9	1.6±0.1	8	0.07±0.05	1.7

†Larsen & Richtler (2000). Super and sub-indices for Γ are the same as Table 3.8. Columns 5 and 8 are the mean and standard error for each model. Column 9 values using Goddard et al. with our Σ_{SFR}. Column 11 is the fraction between the light from clusters and the light from field stars in the magnitude range 18 to 23 using M_V.

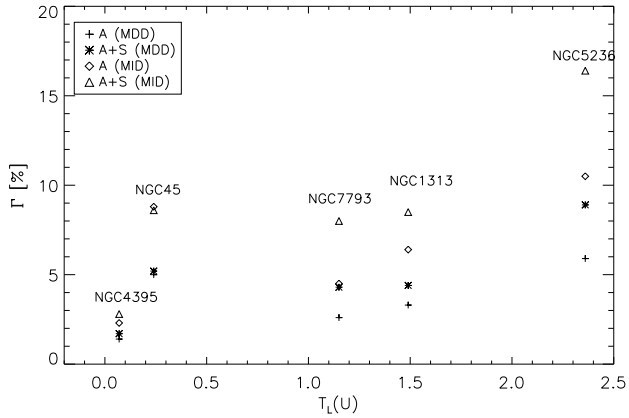

Figure 3.17: Relation between T_L(U) and Γ using the models MDD and MID. The values for Γ using the Accepted+Suspected sample are also included.

3.6. Discussion

In Fig. 3.16 we compare our Γ vs. $\Sigma_{\rm SFR}$ measurements with the data in Goddard et al. (2010) (rhombs). We cannot confirm whether a correlation is present within the range of $\Sigma_{\rm SFR}$ values probed by our data, but overall our Γ values are similar to those found by Goddard et al. in this range of $\Sigma_{\rm SFR}$ or slightly lower. However, following the methods of Goddard et al., Adamo et al. (2011) estimated values for Γ in the two blue compact galaxies ESO 185 and Haro 11. The results from Adamo et al. are in good agreement with the power law proposed by Goddard et al. (2010).

According to Larsen & Richtler (2000), the five galaxies span a significant range in specific U-band luminosity. From Table 3.9 and Fig. 3.17, we see that galaxies with high Γ values generally tend to also have high $T_L(U)$ values. One exception to this is NGC 45, which has a rather high Γ for its $T_L(U)$. The $T_L(U)$ value for this galaxy is, however, based on only two clusters, hence subject to very large uncertainty. Nevertheless, the high Γ value for NGC 45 is also somewhat puzzling given that it has the lowest $\Sigma_{\rm SFR}$. This may suggest that there is not a simple relation between Γ and $\Sigma_{\rm SFR}$. In this context, it is also interesting that this galaxy has a large number of ancient GCs for its luminosity, yielding an unusually high globular cluster specific frequency for a late-type (Sd) galaxy (Mora et al. 2009).

Our measurements of Γ values in the range ~2–10% are consistent with other recent estimates of the fraction of stars forming in bound clusters. It should be kept in mind that this number is not necessarily an indicator of "clustered" vs. "isolated" star formation, since some stars may form in embedded clusters that dissolve or expand on short enough time scales to drop out of our sample.

There is a correlation between T_L(U) and Γ, as shown in Fig. 3.17. We estimated

values for Γ using the accepted+suspected samples for the three-band photometry and for MDD and MID models as presented in the figure. The galaxy NGC 45 deviates from the apparent relation. Two things must be noted. (1) The inclusion of the suspected sample does not change the trend observed dramatically, although the increases in the CFRs is reflected in the new Γ estimations, and (2) CFR estimates based on different disruption models follow the same trend.

Estimates of the actual "infant mortality rate" are hard to make unless the embedded phase is probed directly, something which is difficult in external galaxies. For NGC 1313, Pellerin et al. (2007) find that the IMR is a very efficient process for the dissolution of star clusters in this galaxy (*IMR* = 90%) based on UV fluxes in and out of clusters. Our estimate of a Γ value of 3%–5% for NGC 1313 indicates that > 95% of star formation in this galaxy happens outside clusters that are detected in our sample, in reasonable agreement with the Pellerin et al. estimate. However, it is also clear that cluster dissolution is a continuous process, and systems that are probed at older ages are generally expected to show a lower fraction of stars in clusters.

A proper account of dissolution effects could, in principle, be used to correct measurements of Γ at different ages to a common reference (say, 10 Myr), but current uncertainties in the disruption process makes this difficult to apply in practice. As a case in point, Chandar et al. (2010) estimate a mass-independent disruption rate of 80%–90% per decade in age for NGC 5236, a value that is significantly higher than our estimate ∼ 40% (∼ 62% is our estimated weighted average). These differences underscore that the definition of cluster samples (especially in star-forming galaxies) is subject to strong selection effects, many of which are age dependent and thus likely to affect the age distributions. One example is the size cuts, which can easily cause a bias against young objects where stochastic SIMF sampling leads to underestimated sizes even for masses of $\sim 10^4 M_\odot$. Furthermore, there may also be a physical relation between cluster size and age (e.g. Elson et al. 1989, Barmby et al. 2009, Mackey & Gilmore 2003a,b), compounding this problem.

When using young clusters (τ less than 100 Myr) we observed that the slope of the age distribution gets shallower, indicating a possible curvature or deviation from a power-law relation and showing values for the age distributions different from previous estimations. However, these results are based on a sample that is strongly affected by very few of clusters.

3.7. Summary and conclusions

Using HST observations of the galaxies NGC 45, NGC 1313, NGC 4395, NGC 5236, and NGC 7793, we studied their populations of star clusters and field stars separately with the aim of constraining the quantity Γ, i.e. the ratio of stars forming in bound clusters and the "field". We have been following the basic approach described in Paper I, i.e. comparing synthetic and observed color-magnitude diagrams (for the field stars) and SED model fitting (for the star clusters), to get the formation histories of stars and clusters.

We tested how stochastic effects induced by the SIMF influence photometry and the estimation of ages and how the completeness limits are affected. We conclude that massive clusters (log(Mass)[$M_\odot$] $\geq$ 5]) are easily detected (with the parameters used in this work) at any age, while the detection of clusters with masses below $\sim 10^4 M_\odot$ can be strongly affected by stochasticity. Our tests thus show that completeness functions do not just depend on magnitude, but also on age and size. It would be desirable to find better classification methods than a simple size cut to determine what is, and what is not, a cluster.

We estimated star formation histories and found that NGC 5236 and NGC 1313 have the highest star formation rates, while NGC 7793, NGC 4395, and NGC 45 have lower SFRs. Within the uncertainties, we do not see significant variations within the past 100 Myr.

Comparing observed and modeled mass- and and luminosity distributions for the cluster populations in different galaxies, we find that we cannot distinguish between different disruption models (mass dependent vs. mass independent). We compared model luminosity functions for each disruption scenario with observed LFs and derived CFRs for the cluster systems. From our measurements of the CFRs and SFRs we derived the ratio of the two, Γ, as an indication of the formation efficiency of clusters that remain identifiable until at least 10^7 years. We find Γ values in the range ~2–10%, with no clear correlation with $\Sigma_{\rm SFR}$ within the (limited) range probed by our data. However, our measurements are roughly consistent with those of Goddard et al. (2010), who find a relation between $\Sigma_{\rm SFR}$ and Γ for a sample of galaxies spanning a wider range in $\Sigma_{\rm SFR}$ (but more heterogeneous data).

A general difficulty in this type of work is to identify a reliable sample of bona-fide clusters. Comparison with previous work suggests that the cluster samples, although covering the same galaxies, are significantly affected by the criteria used to classify clusters over the images. This results in different estimates of cluster system parameters, such as those related to the disruption law. Accurate estimates of these parameters are also hampered by the relatively poor statistics that result from having only patchy coverage of large, nearby galaxies in typical HST imaging programs.

We would like to thank the referee for comments that helped to improve this article. This work was supported by an NWO VIDI grant to SL.

Table 3.10: Online material. The rows presented in this table illustrate what the online material will look like. *Column 1st*: Name of the galaxy, field observed and cluster number. *Column 2nd*: ID classification .*Columns 3rd and 4th*: X and Y coordinates of the clusters over the images. *Columns 5th and 6th*: Right ascension and declination (J2000). *Columns 7th-14th*: U, B, V, and I magnitudes and their respective errors. *Column 15th*: Age estimated for LMC-like metallicity. *Column 16th*: Mass estimated for LMC-like metallicity. *Columns 17th and 18th*: Sizes measured with SExtractor and Ishape, respectively. *Column 19th*: Flag for accepted and suspected objects.

Galaxy_Field_#	ID	X	Y	RA	DEC	U	Ue	B	Be
		[PIX]	[PIX]	[J2000]	[J2000]	[Mag]	[Mag]	[Mag]	[Mag]
NGC5236_1_1	5214	245	2539.	13:36:58.81	-29:51:13.94	21.08	0.10	20.89	0.01
NGC5236_1_2	5238	340	2549.	13:36:58.99	-29:51:09.77	22.90	0.21	22.27	0.02
NGC5236_1_3	4360	596	2225.	13:36:58.23	-29:50:51.62	22.55	0.15	22.32	0.02
NGC5236_1_4	5454	614	2609.	13:36:59.62	-29:50:58.36	20.73	0.04	20.64	0.01
NGC5236_1_5	3919	621	1928.	13:36:57.22	-29:50:44.62	21.46	0.07	21.79	0.02
NGC5236_2_1	6116	574.	2690.	13:37:05.64	-29:56:51.97	22.07	0.08	22.15	0.01
NGC5236_2_2	5845	655.	2423.	13:37:04.84	-29:56:42.65	22.05	0.13	21.65	0.02
NGC5236_2_3	5690	719.	2180.	13:37:04.10	-29:56:34.62	22.29	0.12	22.57	0.02
NGC5236_2_4	5859	746.	2461.	13:37:05.12	-29:56:39.33	21.72	0.08	21.35	0.01
NGC5236_2_5	5773	821.	2297.	13:37:04.67	-29:56:32.47	21.87	0.08	21.97	0.01

Table 3.11: Continuation Table 3.10.

Galaxy_Field_#	V	Ve	I	Ie	Log(τ)	Log(M)	FWHM$_{SEx}$	FWHM$_{Isha}$	Flag
	[Mag]	[Mag]	[Mag]	[Mag]	[Yr]	[$M_\odot$]	[Pix]	[Pix]	
NGC5236_1_1	20.86	0.01	20.57	0.03	8.00	3.86	7.35	2.91	acpt
NGC5236_1_2	21.66	0.02	20.64	0.02	8.87	4.43	5.84	0.74	acpt
NGC5236_1_3	21.90	0.02	21.09	0.02	8.92	4.08	3.81	1.30	acpt
NGC5236_1_4	20.54	0.01	20.14	0.01	8.39	4.20	4.80	1.93	acpt
NGC5236_1_5	21.76	0.02	21.24	0.03	8.05	3.53	6.16	1.63	acpt
NGC5236_2_1	22.04	0.01	21.61	0.02	8.00	3.48	3.89	0.95	acpt
NGC5236_2_2	21.40	0.01	20.71	0.02	8.78	4.16	7.37	3.67	acpt
NGC5236_2_3	22.28	0.02	21.62	0.02	7.81	3.48	3.91	1.35	acpt
NGC5236_2_4	21.17	0.01	20.71	0.01	8.70	4.18	6.79	2.79	acpt
NGC5236_2_5	21.74	0.01	21.23	0.02	8.39	3.73	4.39	1.84	acpt

He who is not courageous enough to take risks will accomplish nothing in life.
–Muhammad Ali

Chapter 4

The relation between surface star formation rate density and spiral arms in NGC 5236 (M83).

E. Silva-Villa & S. S. Larsen
Submitted to *A&A*, 2011.

Abstract

For a long time the consensus has been that star formation rates are higher in the interior of spiral arms in galaxies, compared to inter-arm regions. However, recent studies have found that the star formation inside the arms is not more efficient than elsewhere in the galaxy. Previous studies have based their conclusion mainly on integrated light. We use resolved stellar population to investigate the star formation rates throughout the nearby spiral galaxy NGC 5236. We aim to investigate how the star formation rate varies in the spiral arms compared to the inter-arm regions, using optical space-based observations of the NGC 5236. Using ground-based Hα CTIO images we traced regions of recent star formation, and reconstructed the arms of the galaxy. Using HST/ACS images we estimate star formation histories by means of the synthetic CMD method. Arms based on Hα images showed to follow the regions where stellar crowding is higher. Star formation rates for individual arms over the fields covered were estimated between 10 to 100 Myr, where the stellar photometry is less affected by incompleteness. Comparison between arms and inter-arm surface star formation rate densities (Σ_{SFR}) suggested higher values in the arms ($\sim$ 0.5 dex). Over a small fraction of one arm we checked how the Σ_{SFR} changes for the trailing and leading part. The leading part of the arm showed to have a higher Σ_{SFR} in the age range 10-100 Myr. Predictions from a density wave theory of a rapid increase in the star formation at the edge where the stars and the gas enter the density wave are confirmed. The Σ_{SFR} presents a steep decreases with distance from the center of the arms through the inter-arm regions.

4.1. Introduction

Studies of OB stars (see e.g. Morgan et al. 1953, McGruder 1975, Muzzio 1979, Kaltcheva 2009), show that the concentration of these type of stars is higher in the Sagittarius arm of the Galaxy. This suggest an active star formation in the arms of spiral galaxies. The creation of spiral arms is a problem that has been studied since the late 60's (e.g. Lin & Shu 1964, Roberts 1969). The density wave theory explains how the spiral arms can be formed and can remain stable over time for an isolated galaxy. The theory predicts more active star formation in the arms, where the gas compression induced by the density waves triggers the process.

If the density wave theory is correct, the process of gas being compressed by the waves could lead to many observable effects, e.g. different star formation rates or color-gradients across the arms. Assuming a constant angular velocity of the spiral density wave and an approximately flat rotation curve of the stellar component, inside the corotation radius the gas will overtake the density wave, which will produce an increase in the star formation. Outside the corotation radius the wave overtakes the gas. Consequently, the stars will drift and age, creating a color gradient that can be observed. Martínez-García et al. (2009) have studied the color gradient across spiral arms of 13 spiral galaxies. In their work, a reddening free index was used to study this process, concluding that azimuthal color gradients are common in spiral arms of disk galaxies.

Compression of the gas across the galaxy is expected to be observed as regions with enhance star formation. The components use to estimate the star formation efficiencies (SFE) in a galaxy are the gas and the stellar population, the later being commonly measured through their integrated light. When H_2 is use to trace star forming regions (e.g. Foyle et al. 2010), there seemed to be no specific correlation between the SFE and the spiral arms. However, studies that estimate the SFE as the fraction of Hα and/or HI maps do find a correlation between the SFE and the spiral arm (Lord & Young 1990, Cepa & Beckman 1990, e.g.). Nevertheless, it is important to note that most of the studies of star formation (either efficiency or rate) and their relation with the arms over spiral galaxies have been done using gas components as tracers, namely HI, H_2, CO, etc. and unresolved stellar populations, measured through their integrated light (e.g. Knapen et al. 1996, Leroy et al. 2008). Tracers based on gas components are assumed to indicate the regions where SFE is high, which could lead to erroneous estimations, as stated by Foyle et al. (2010).

As a new approach, we present in this paper the use of *resolved* stellar population as tool to study how the surface star formation rate density (Σ_{SFR}) varies in the arms and inter-arm areas of the nearby spiral galaxy NGC 5236. This galaxy has been selected because it is one of the closest face-on, nearby, grand-design spiral galaxies, where spatial resolution allows a study for this kind. The low inclination in the line-of-sight reduces the contamination by reddening during the observations. Previous estimations of the Σ_{SFR} show values of $\sim 13\times10^{-3}$M$_\odot$yr^{-1}Kpc^{-2} (see Larsen & Richtler 2000, Calzetti et al. 2010, Silva-Villa & Larsen 2011), which is high compare to other galaxies (e.g. Larsen & Richtler 2000, see table 2). Harris et al. (2001) studied the

cluster system in the inner 300 pc, indicating a possible burst that began aroung 10 Myr ago. This burst combined with the high levels of Σ_{SFR} suggest that the NGC 5236 is still actively forming stars, making it ideal to study differences in the star formation and the possible relations with environment and location.

Kinematic studies of NGC 5236 were presented by Lundgren et al. (2004) based on gas (H_2+HI+He) measurements. The estimation of the gas surface density in the arms done by Lundgren et al. is higher than the Toomre's value for stability ($Q \propto \Sigma_{gas}^{-1}$). This excess is possibly causing instabilities in the arms of the galaxy, potentially leading to star formation. However, their estimation of the gas surface density in the inter-arm regions do not show the same high values. In a further work, Lundgren et al. (2008) used far-UV, B and Hα integrated light to estimate star formation rates, while CO was used for gas maps. Lundgren et al. conclude that the star formation presents higher levels in the nuclear regions, close where the bar ends, and in the arms of the galaxy. In the same presentation, Lundgren et al. claim for an increased SFE along the arms of this galaxy.

This paper is structured as follows. We introduce the observations, optical and Hα, used to study the field stellar population and the regions of recent star formation, respectively, in Sect. 4.2. Section 4.3 is devoted to review how the optical bands were used to run the photometry of the field stars. Using Hα (i.e. tracing recent star formation), we will introduce in Sect. 4.4 the method used to re-construct the arms of the galaxy. Using the photometry from Sect. 4.3, we estimated the star formation history of different groups of field stars in Sect. 4.5. Finally, we present our discussion and conclusions in Sects. 4.5 and 4.6, respectively.

4.2. Observations

For the study presented here, we used images from Hubble Space telescope and Cerro Tololo observatory, covering different optical wavelengths and Hα.

4.2.1. BVI observations and data reduction

We use observations of NGC 5236 taken by the *Hubble Space Telescope* (HST), using the *Advanced Camera for Surveys* (ACS). The instrument has a resolution of 0."05 per pixel. With a distance modulus of 28.27 ($\sim$ 4Mpc, Thim et al. 2003), 1 pixel corresponds to $\sim$1 pc in our images.

The images of this galaxy have been taken in the optical bands F435W ($\sim B$), F555W ($\sim V$), and F814W ($\sim I$), with exposure times of 680 sec for the bands B and V, and 430 sec for the band I. Our observations were taken in 2004 as part of the Cycle 12, centered at $\alpha : 13 : 37 : 00$ and $\delta : -29 : 49 : 38$ and $\alpha : 13 : 37 : 06$ and $\delta : -29 : 55 : 28$ (J2000) for the first and second field observed, respectively.

The standard STScI pipeline was used for the initial data processing. ACS images were drizzled using the multidrizzle task (Koekemoer et al. 2002) in the STSDAS package in IRAF using the default parameters, but disabling the automatic sky

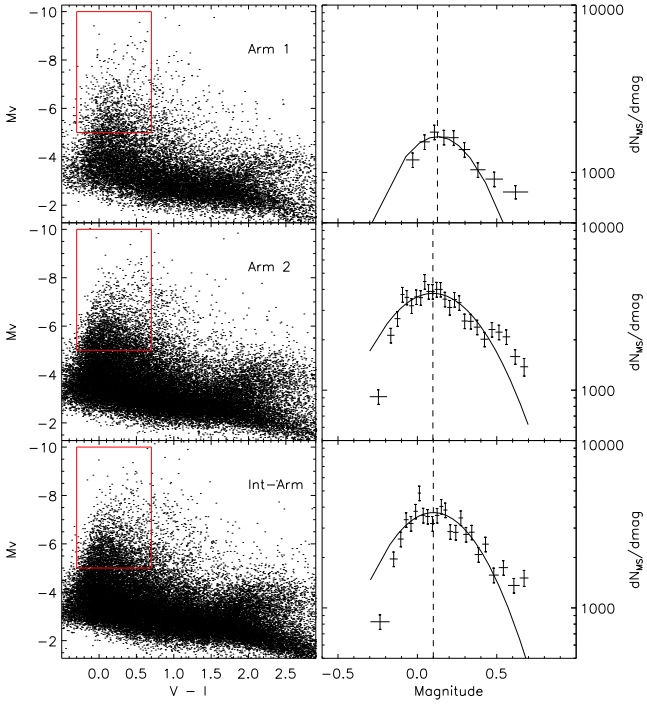

Figure 4.1: *Left column*: Hess diagrams for the Arm 1, Arm 2, and inter-arm regions. *Right column*: Histogram of main sequence stars inside the boxes marked over the CMDs. Error are Poissonian. Vertical dashed lines represent the peak of the Gaussian distributions.

subtraction. Object detection for field stars was performed on an average B, V, and I image, using daofind in IRAF.

4.2.2. Hα observations

We use an archival *Cerro Tololo Inter-American Observatory* (CTIO) 1.5m telescope image of NGC 5236, taken in 2006 as part of the *Survey for Ionization in Neutral Gas Galaxies* (SINGG, Meurer et al. 2006)[1]. The survey used the Hα and R bands over the galaxies observed, with a resolution of 0.″4 per pixel. The total exposure time of the observation for NGC 5236 was 1800 sec, with center coordinates at α : 13 : 37 : 02

[1]SINGG is a subsample of the *HI Parkes All Sky Survey* (HIPASS), Meyer et al. (2004)

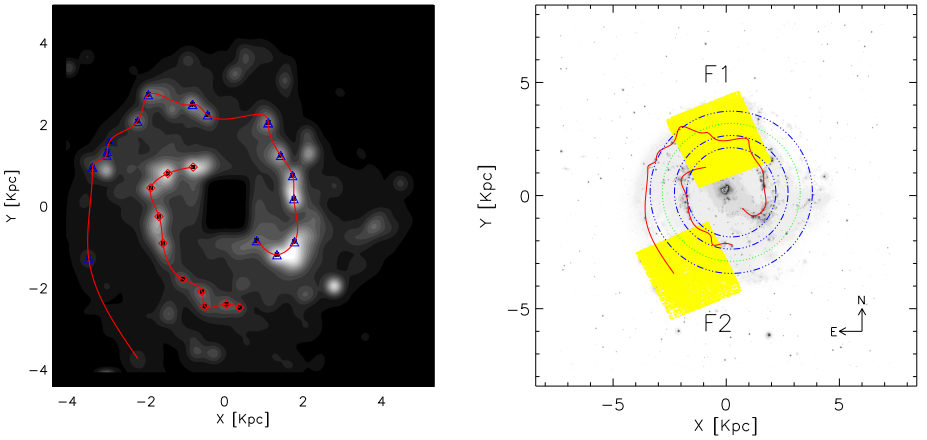

Figure 4.2: Arms over the CTIO observations. *Upper panel*: Blurred image used for the detection of pronounced Hα regions. *Lower panel*: Original CTIO of NGC 5236. Overplotted in each panel are the estimated locations of the arms. In the lower panel the two fields observed with the HST/ACS are marked as yellow regions. Green dot-dashed line is the corotaion radius located at 170" (Lundgren et al. 2004). Dash-dotted lines in blue denote annuli at 200."0, 140."0 and 110."0, see text for details.

and $\delta : -29 : 52 : 06$ (J2000). The image use in this paper is base only on the Hα filter. For details on the observations and calibration of the image see Meurer et al. (2006).

4.3. Field stars photometry

Details of our method of analysis can be found in Silva-Villa & Larsen (2010). Below we will reiterate the main points of the procedures we used to carry out photometry on our data.

Due to the crowding, we performed PSF photometry for field stars. Using a set of bona-fide stars visually selected in our images, measuring their FWHM with *imexam*, we construct our point-spread function (PSF) using the PSF task in DAOPHOT. This procedure is employed in the same manner for each band (i.e., B,V, and I). The PSF stars are selected individually in each band, in order to appear bright and isolated. PSF photometry is done with DAOPHOT in IRAF.

Our PSF-fitting magnitudes are corrected to a nominal aperture radius of 0."5, following standard procedures. From this nominal value to infinity, we apply the corrections in Sirianni et al. (2005).

HST zero-points[2] have been applied to the PSF magnitudes after applying aperture corrections. The zero-points used in this work are $ZP_B = 25.767$, $ZP_V = 25.727$

[2]www.stsci.edu/hst/acs/analisys/zeropints/#tablestart

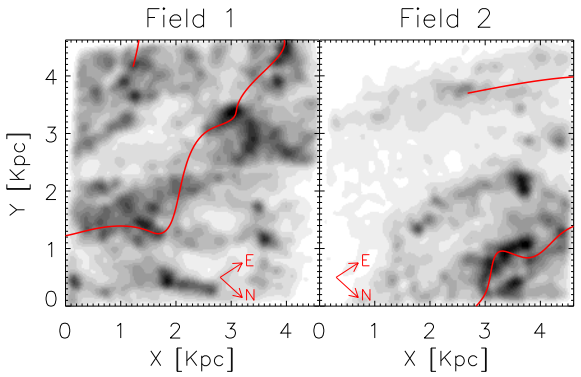

Figure 4.3: Surface density of stars for the ACS fields. Red lines represent the path of the arms.

and $ZP_I = 25.520$ magnitudes. Typical errors of our photometry do not change dramatically from the ones in Silva-Villa & Larsen (2010, see its Fig. 2).

The final color-magnitude diagrams (CMD) for the stars in the arms and the inter-arm regions (see Sect. 4.5 for definition of the stars that belong to the arms and in the inter-arm region) are presented in Fig. 4.1, left columns. In the same figure we attempt to observe any indication of changes in the extinction. We created histograms of the main sequence stars, defined to be stars in the color range $-0.3 \leq (V-I) \leq 0.7$ and in the magnitude range $-10 \leq M_V \leq -5$, as indicated by the red boxes over the CMDs (see Fig. 4.1). The histograms were created with variable bin widths using 100 stars per bin. The number of stars is normalized to the width of the bin. Over the observed distributions we fitted a Gaussian function to estimate the maximum of the distributions. We do not observe a large variation among the Arm 2 and the inter-arm areas, where the peak of the distribution is close the same value ($\sim 0.10 \pm 0.02$). However, the Arm 1 presents a slight shift in the peak of the distribution ($\sim 0.13 \pm 0.02$) compare to Arm 2 and inter-arm regions. This difference is not large (≤ 0.03, and errors overlap), but we note that the Arm 1 is closer to the galactic center, where extinction can be affecting the observations. There is also an apparent increase in the distributions close to $(V-I) \approx 0.5$. Inside our photometric errors, separating the main sequence stars from the blue He burning phases is not straightforward, but the count of stars can give an indication of the presence of these stars, as seen in Fig. 4.1, where at $(V-I) \approx 0.5$ the distribution of stars clearly deviates from the Gaussian fit.

4.4. Defining the spiral arms over NGC 5236

To identify the arms of NGC 5236, we followed the method described by Scheepmaker et al. (2009), using Hα as indicator. The CTIO image of the galaxy was cropped to remove as much background as possible. Over the new (sub)image, we use a Gaussian kernel (with a 20 pixels width) to blur the image, enhancing the regions where

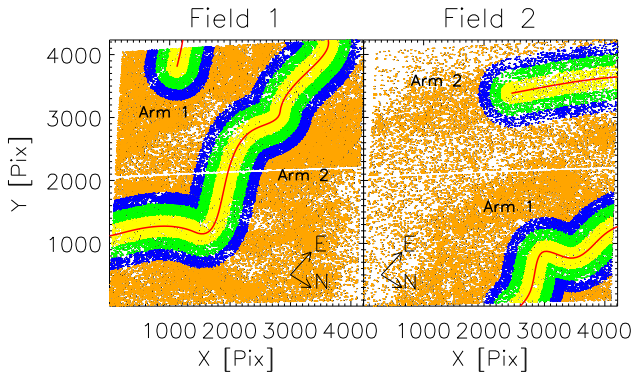

Figure 4.4: Selection of the resolved stellar population over the arms of NGC 5236. Red lines show the arms of the galaxy based on Hα images. Yellow, green, and blue represent the selection of stars at different distances that belong to the arms. Orange regions represent the inter-arms.

Hα appears to be more concentrated. Because of the high concentration of gas in the center of the galaxy, we manually mask this part of the image, which will allow better analysis of the regions outside of the center. We have analyzed the blurred image with *Daofind* in IRAF to find the places where Hα is more concentrated (minimum good data value over 400). The coordinates retrieved by IRAF have been visually inspected to remove unnecessary detections, i.e. detections that could affect the estimations of the arm's path and that are not part of the ACS field-of-view. We have used a cubic spline interpolation to fit the arms of NGC 5236. Figure 4.2 depicts the CTIO images. The upper panel is the cropped and blurred image, overplotted with the estimated location of the arms. The lower panel shows the original CTIO image, overplotted with the location of the arms (red lines) and the two fields covered by the ACS observations (yellow squares). Conversion of the coordinates from the CTIO coordinate system to the ACS coordinate system has been done using *wcsctran* in IRAF. First, using the header of the CTIO image, coordinates were converted to WCS coordinates, and then, using the same procedure, converted finally to ACS coordinates system. The different circumferences are marking the distances 200."0, 140."0, 170."0 and 110."0 used to estimate the velocity of a particle at different radii (see Sect. 4.6).

We create the density plot of the resolved stellar populations over the ACS fields with the arm's path created using the Hα. After overplotting the arms, we observe that the arms follow the region where the density of stars is higher, as seen in Fig. 4.3. From the same figure, it is observe that other regions have high density of stars, e.g. in the field 2 there is a possible "feather" between the two arms, and in the field 1 we observe many regions with high densities of stars, which is expected, due to the proximity to the center of the galaxy, where the concentration of gas is higher (e.g. Crosthwaite et al. 2002, Lundgren et al. 2004).

For the rest of this paper we will refer as *Arm 1* to the arm that is fully inside the corotation radius (see green dotted line in Fig. 4.2), while the *Arm 2* has one part inside the corotation radius and one part outside of it. Figure 4.2 presents the two arms and the corotation radius, estimated by (Lundgren et al. 2004) to be located at 170″.

4.5. Selection of stars and star formation histories

We aim to study here how the star formation varies from the center of the spiral arms to the inter-arm regions. We use the resolved stellar population detected over our ACS fields and estimate their star formation histories at a fixed distance from the center of the arm.

4.5.1. The arms

Stars were selected every 0.2 Kpc, assuming that the arms presented above mark the "center" of the distribution. Figure 4.4 shows the distribution of the stars which follow the arms at the distances 0-0.2, 0.2-0.4, and 0.4-0.6 Kpc, represented with the colors yellow, green, and blue, respectively. In our second field the distance between the two arms will allow to cover a larger area, however, we kept the same distances as in the first field in order to have comparable results among the fields.

For each of the selected group of stars, star formation histories (SFH) were calculated using the synthetic CMD method (Tosi et al. 1991). In a previous work we tested the IDL-based program created to estimate the SFH, studing the spiral galaxy NGC 4395 (Silva-Villa & Larsen 2010). In a further presentation we investigated the SFH of a set of galaxies, including NGC 5236 (see Silva-Villa & Larsen 2011). We have updated the code presented by Silva-Villa & Larsen (2010) allowing the use of multiple metallicities. When using multiple metallicities, the code models the Hess diagram as a weighted sum of all isochrones in the input library. The final SFH is obtained adding together the individual SFR over time for each assumed metallicity.

The parameters used for the estimation of the SFH over NGC 5236 are: Distance modulus of 28.27, solar and LMC-like metallicities, a binary fraction of 0.5 with a mass ratio between 0.1-0.9 (assuming a flat distribution and no binary evolution), and using the color combination V-I. We normalized our estimations by the areas covered, having then the surface star formation rate density (Σ_{SFR} [$M_{\odot}yr^{-1}Kpc^{-2}$]). The estimation of the different areas covered was carried out following a similar procedure as for the selection of the stars. We create an image of the size of the ACS fields and calculate the distance of each pixel to the arms, assuming the same distances as for the stars selection. Having the total amount of pixels under the desired area, the areas where calculated following the relation:

$$A_i = A_{total} \times \frac{Npix_{A_i}}{Npix_{A_{total}}} , \tag{4.1}$$

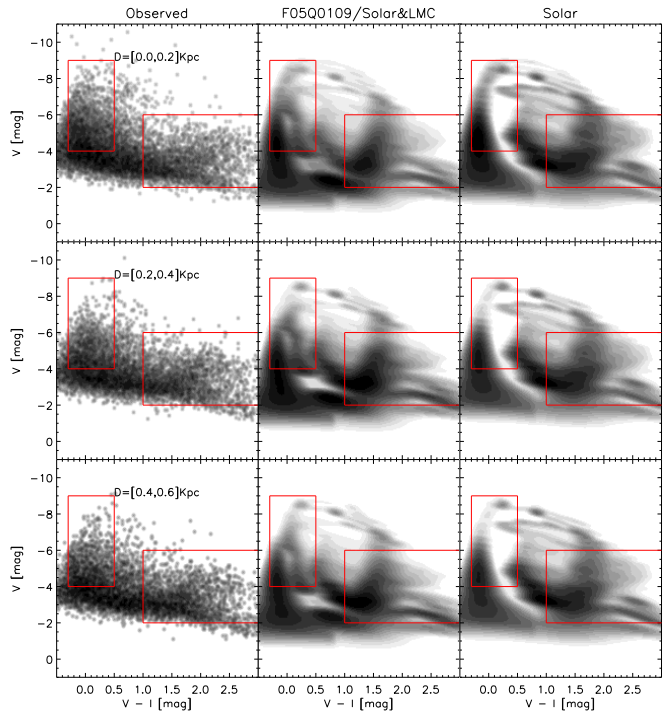

Figure 4.5: *Left colum*: CMDs for the Arm 2 in the field 1 at different distances from the center of the arm. *Middle colum*: Best fit CMDs for the Arm 2 in the field 1 at different distances from the center of the arm assuming solar and LMC like metallicities, a binary fraction of 0.5 with a mass ratio between 0.1-0.9, and a fix extinction of 0.29. *Right colum*: Best fit CMDs for the Arm 2 in the field 1 at different distances from the center of the arm assuming solar metallicity, a binary fraction of 0.5 with a mass ratio between 0.1-0.9, and a fix extinction of 0.29. The fits were done using the red boxes shown in the figure.

where A_i is the area to be calculated, A_{total} is the total area covered by the ACS (21.3 Kpc^2, each field), and $Npix_{A_i}$ and $Npix_{A_{total}}$ are the number of pixels for the area i and the total number of pixels, respectively.

Figure 4.5 illustrate the fits done over the field 1 for the three areas over the Arm 2. We noted that the fits are far from perfect. Trying to understand what could be the cause of the deviation of the fits, we estimated SFHs varying the input parameters. As an example, the right column in Fig. 4.5 present the fits using only solar metallicity (instead of solar and LMC). It is clear that solar metallicity leaves a "gap" between the main sequence stars and the blue loop, which is not seen in

our observed CMDs (first column). The combination of both metallicities gives a better fit to the data, as the blue loops extend to higher effective temperatures (bluer colours) for LMC-like metallicity, and we can not reject the possibility of higher ones. Regardless of the improvement when using a combination of metallicities, we note that the neither red nor blue He burning phases are well fitted by our program, appearing bluer and redder, respectively, in our final fits, when compare with the observations. It is important also to note that the fitting at advance stages of stellar evolution (i.e. RGB and/or AGB phases) presents a poor fit. This could be related with the treatment of these phases by the isochrones and the proximity to the completeness limits. Assumptions of no binaries did not show any improvement in our estimations. Following the small change in extinction, as suggested in Sect. 4.2, we used a time dependent extinction, but we did not observed any improvement. The middle column presents the best fit which combines the parameters described in the previous paragraph.

In view of the difficulties reproducing the observed CMDs, caution should clearly be exercised when interpreting SFHs inferred from these fits.

For each field and each arm, between 10 and 100 Myr (age range less affected by incompleteness), we estimated the mean values for Σ_{SFR}. We also combined results for each arm, adding the results from each field, see Fig. 4.6 and 4.7. We summarize our results in table 5.1.

Independent measurements of Σ_{SFR} (i.e. per field, per arm, per area covered) are shown in Fig. 4.6, where Arm 2 suggest that during the past 100 Myr there has been an increase in the Σ_{SFR} (right panels). To observe the total behave of the SFH we joined the resulting SFH for all areas of the Arm 2, but for the Arm 1 we only used the results from the field 2, because the areas covered in the field 1 were too small and a clear distinction between arm and inter-arm region was not strong enough. The results are presented in Fig. 4.7. Observing this figure it becomes clear the increase of the Σ_{SFR} between 10 to 100 Myr, for Arm 2. This increase is better observed in the upper-right panel of Fig. 4.7. This increase is observed for each one of the areas covered in that particular arm, which suggest a physical effect. In Sect. 4.6 we interpret this results.

4.5.2. The inter-arm regions

To estimate the Σ_{SFR} for the inter-arm regions we used the stars outside the arms (orange regions in Fig. 4.4). Stars selected in this way were passed to our program and SFHs for each field observed were estimated (see Fig. 4.7 lower panel). The areas were calculated as the total area (A_{total}) minus the areas covered by the arms, then having an estimation of the Σ_{SFR} (see table 5.1). We added the independent estimations for the two fields and plotted the mean value in Fig. 4.8 as a continuum value, which is lower than the values derived for the arms, making a clear distinction between the SFH's happening in the arms compare to the inter-arm areas. It is important to note the differences among the fields. The first field, which is close to the center of the galaxy present a higher Σ_{SFR}, even indicating a small increase

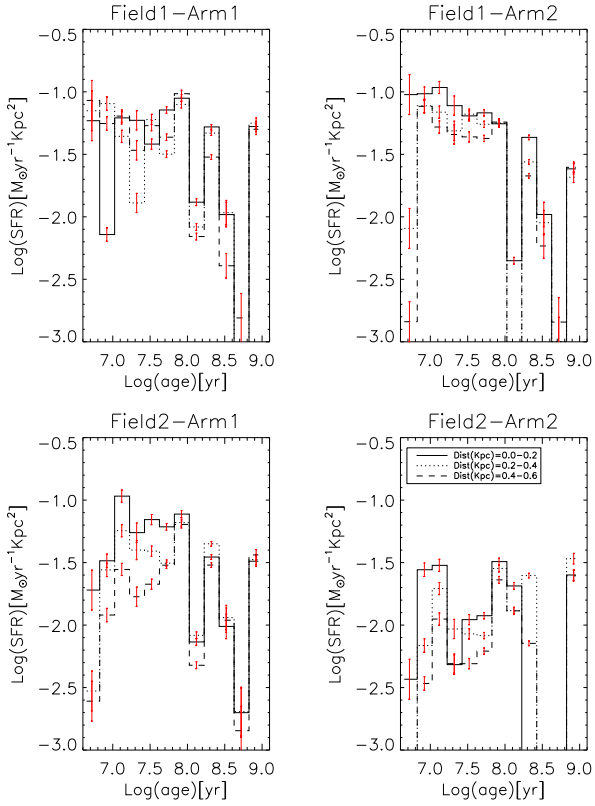

Figure 4.6: Star formation histories for each arm over each field. Errors are the random errors of our program (see Silva-Villa & Larsen 2010).

over time. The second field, which is located further away from the center, presents a lower Σ_{SFR}. This separation indicates differences that could be related with the amount of material that could potentially be use to form stars, it is expected to find more gas concentrated in the center of the galaxy than in the outer parts (e.g. Crosthwaite et al. 2002, Lundgren et al. 2004). Also important to note is the increase observed between ~20-100 Myr. This increase could be related with the limits stated for the arms and inter-arm regions, where the increase in the number of stars at the "edge" of the arms could be contaminating the inter-arm areas. Also, as noted in the previous sections, there are regions in the inter-arms that present high levels of Hα, suggesting recent star formation activity. Nevertheless, based on the fits observed in the previous section, the possibility of observing an increase could be an artifact of the fitting process.

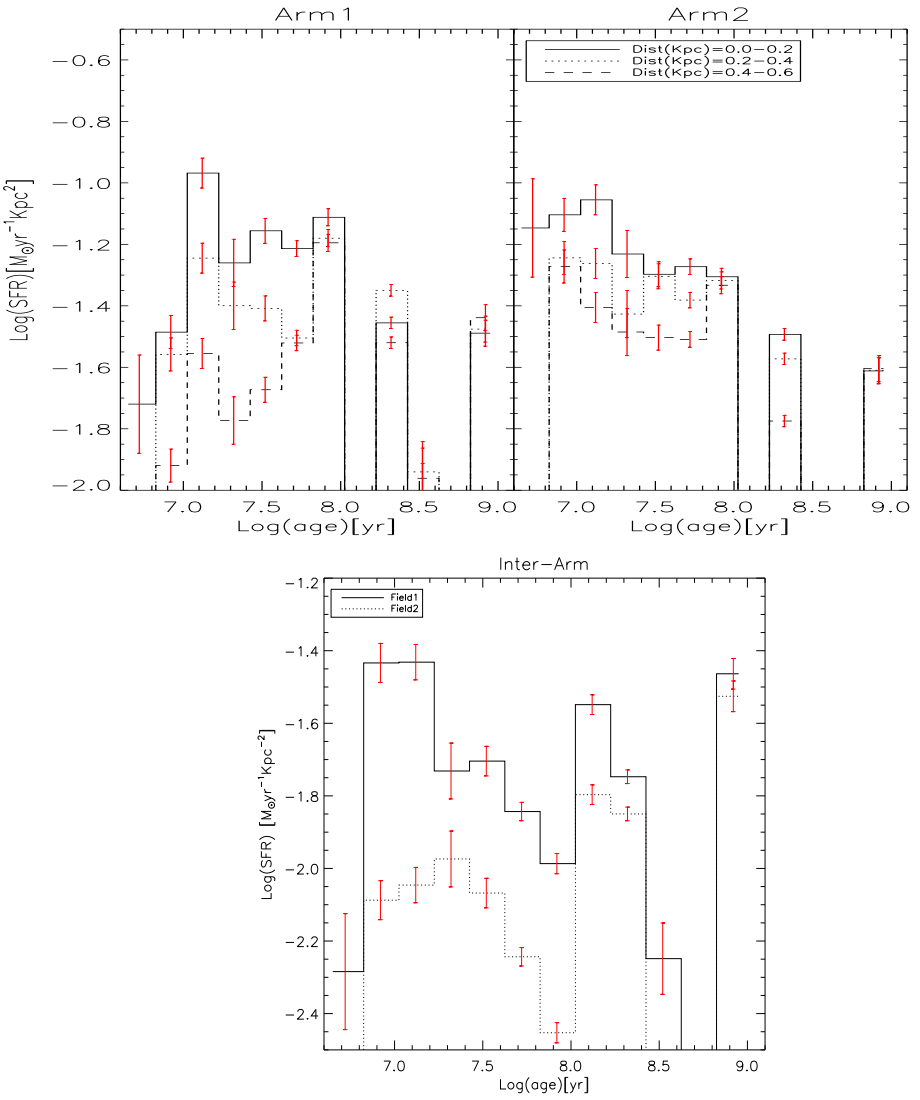

Figure 4.7: *Upper panels*: Star formation histories for each arm after joining fields. *Lower panel*: Star formation history of the fields. Errors are the random errors of our program (see Silva-Villa & Larsen 2010).

Table 4.1: Surface star formation rate densities at different distances from the center of the arm. Errors are the standard deviation of the mean. Arm 1 values are for field 2 only.

Field_Arm	$Dist_{arm}$ [Kpc]	Area [Kpc^2]	Σ_{SFR} [$\times 10^{-3} M_\odot yr^{-1} Kpc^{-2}$]
Arms covered			
Arm1	0.0-0.2	1.06	67±24
Arm1	0.2-0.4	1.05	43±14
Arm1	0.4-0.6	1.01	29±18
Arm2	0.0-0.2	3.29	67±15
Arm2	0.2-0.4	3.44	41±19
Arm2	0.4-0.6	3.54	31±17
Inter-arms covered			
Field1	—	12.84	23±11
Field2	—	15.24	8±3

4.6. Discussion

The Σ_{SFR} of the arms in NGC 5236 estimated here suggest that the arms of the galaxy have increased their star formation rate during the last 100 Myr (see Fig. 4.7, upper panels).

Figure 4.8 shows the variation of the mean Σ_{SFR} (between 10 and 100 Myr) as a function of distance across the arms and the Σ_{SFR} for the inter-arm regions, as defined in the previous section. Starting from the innermost region of the arms, traced by Hα, we observed a very fast and steep decrease moving outward across the arms. Estimations of Σ_{SFR} show a clear difference between the arms and the inter-arm regions, the former having a higher value in the center, while reaching similar levels at the external regions, where the separation between arm and inter-arm becomes dificult. In Fig. 4.3 we showed how Hα can trace the regions in the galaxy where the crowding of stars is higher, suggesting that the recent star formation might be higher in the arms of the galaxy (assuming that Hα traces regions of recent star formation). There are other regions in the same figure where large concentrations of stars are present, but based on the procedures described here, in those regions Hα is not as strong as in the arms. We do not disregard the possibility of having recent star formation in the inter-arm regions, possibly induced by e.g. supernovae explosion. Lundgren et al. (2008) suggested that in the bar and in the arms of the galaxy, the Σ_{SFR} and the SFEs are higher that in the inter-arm areas. Our measurements of Σ_{SFR} showed to be higher in the arms of the galaxy, in agreement with the work done by Lundgren et al. (2008), when compared to the inter-arm regions (at least qualitatively), however, we do not draw any conclusion regarding the bar of the galaxy.

We tested results expected from the density wave theory and observed its behave

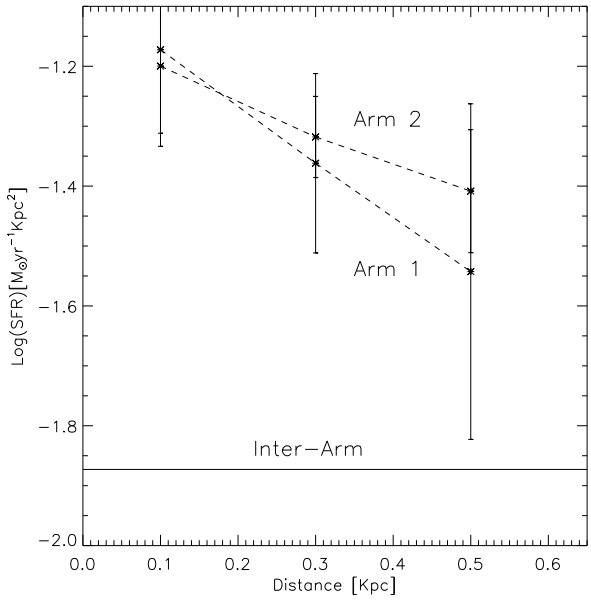

Figure 4.8: Σ_{SFR} as a function of distance for both arms. Straight horizontal line represents the inter-arm (continuum) region.

studying the Σ_{SFR} in the fields covered in this paper. Using increasing distances from the center of the arms (as defined in this paper through Hα) a comparison was made to see the spatial variations in the arms of the galaxy, looking for the differences between the arms and the inter-arm regions.

The density wave theory (Lin & Shu 1964, Roberts 1969) explains how, over the hubble time, it is possible to have arms in spiral galaxies. We test predictions from this theory using resolved stellar population. Assume the gas located in the galaxies is overtaken by the density wave (or viceversa, depending on the radius), then, it is expected to observe higher star formation rate per unit area in the arms of the galaxy compare to the inter-arm regions (Elmegreen 2011a), due to the compression of the gas. Also, from the density wave theory it is expected to observe young stars close to the regions where the gas is more concentrated (i.e. where the star formation is happening), but with time and rotation, stars evolved and travel through the arm. This process can be observe as a color-gradient across the arms. Theoretical predictions of the time ranges for color-gradients were estimated by Martínez-García et al. (2009) using the reddening-free parameter $Q(rJgi)$ (where r, J, g, i are the photometric bands used). Martínez-García et al. show that the maximum of Q is reached at $\sim 2 \times 10^7$yr after a burst of stars (assuming a Salpeter (1955) IMF), and then starts to decline, reaching lower values at $\sim$ 100Myr after the burst. These estimation are of course

affected by inclination, the photometric bands used, metallicity, etc. Martínez-García et al. (2009) studied the color gradient variation over different spiral galaxies. The authors used a sample of 13 spiral galaxies, and showed how a fraction of the arms analyzed clearly showed the expected color gradient expected from the density wave theory. We used resolved stellar populations over the Arm 2, in field 1, where the statistics is larger (see Fig. 4.4), to observe the variations of the Σ_{SFR} inside this (part of the) arm. Separating the areas at 0.2-0.4 Kpc and 0.4-0.6 Kpc into "trailing" and "leading" parts of the arm (left and right in Fig. 4.4), we estimated Σ_{SFR} separately. Using the rotation curve found in Lundgren et al. (2004), we estimated how much time a particle will need to move 0.2 Kpc at different radii. Inside corotation radius (170", Lundgren et al. 2004, $\sim$ 3Kpc for the distance modulus assumed in this paper), the times for a particle to move that distance is close to $\sim$ 5Myr. Outside corotation, the time is increase by a factor of $\sim$ 3 times. As observed in Fig. 4.2, the circumference at different radii are not crossing perpendicular to the arms. Due to this, the real path a particle will have is larger than 0.2 Kpc. We decided to estimate mean Σ_{SFR} every 10Myr, and check how it varies with time. The panel in Fig. 4.9 shows the Σ_{SFR} as a function of position in the arm for different time intervals. Inside corotation, the gas overtakes the density wave, creating a very steep increase in the first few Myr, which must start to decrease with time, as observed in the figure. Nevertheless, Fig. 4.10 presents the average of the Σ_{SFR} over an age range between 10-100Myr. As indicated by the arrow in the figure, and being (mostly) inside corotation, a very steep increase in the Σ_{SFR} is observed, reaching a maximum where the location of the Hα is denoting the center of the arm, and then showing a decrease with time. The small fraction of the arm outside corotation was not analyze separately due to the low statistics and the lack of smoothness of the arm at that location (see Fig. 4.2).

As a consistency check to our results, we selected the massive bright stars over the CMD for Arm 2 in field 1, defined as stars between $-0.3 \leq (V-I) \leq 0.7$ and $-10 \leq M_V \leq -7$. The number of stars in each area were divided by the area covered and then passed to logarithmic scales. The estimated values were shifted to the same levels of the SFH estimations for the comparison (see Fig. 4.9 red dash-dotted line). We observed that the distribution of these stars is in excellent agreement with the distributions showed using the trailing and leading parts of this particular arm.

These interpretations of our results are in good agreement with the conclusions of Martínez-García et al. (2009) for spiral galaxies, and with the predictions of the density wave theory, which states that the leading part of the arm must have a higher star formation compare to the trailing part of an arm, inside the corotation radius.

4.7. Summary and conclusions

Using Hα CTIO images of the galaxy NGC 5236, we have traced the recent star formation regions. Assuming that the star formation is larger in the arms of spirals, we have reconstructed the arms of the galaxy. Superb resolution of HST/ACS observations have allowed us to identify the stellar populations, which we have used

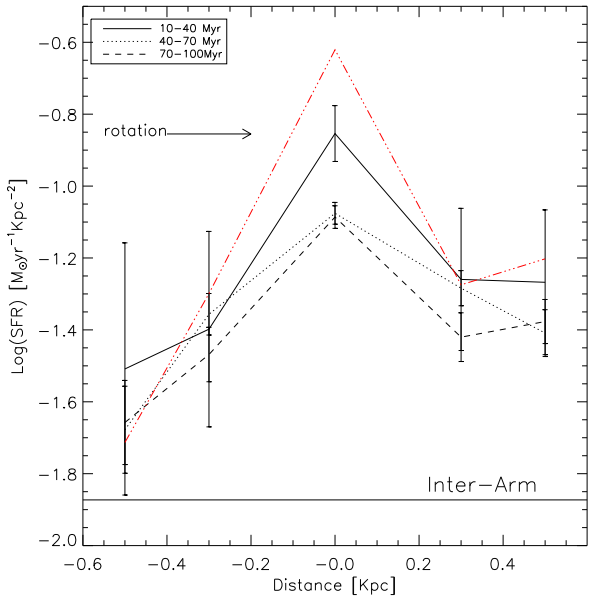

Figure 4.9: Spatial variation of Σ_{SFR} across the Arm 2, observed in field 1. The values are averaged over age every 30 Myr. Errors are the standard deviation of the mean. Red dash-dotted line represent the number of massive, bright stars in the main sequence normalized by the are, see text for details.

to observe the variations of Σ_{SFR} in the inner parts of the arms and compare how this parameters behaves with increasing distances from the center of the arms through the inter-arm regions.

Hα showed to be a good tracer of higher concentrations of stars across the regions covered with our HST observations. Star formation histories were estimated using the synthetic CMD method (Tosi et al. 1991) across the arms and the inter-arm regions separately. We want to emphasis that the fits to the CMDs done are far from perfect. We observed that the variations of different parameters did not further improved our results, however we observed that the inclusion of more than one metallicity helps to reproduce better the observed CMDs. We observed that the arms of NGC 5236 present a higher Σ_{SFR}, compare to the mean value for the inter-arm regions combined by ≥ 0.5 dex. Our estimations show to have similar conclusion as the ones obtained by Lundgren et al. (2008) for this galaxy, which were based on gas, dust, and integrated light studies, while we used resolved stellar populations.

Comparison of the trailing and leading part done over the Arm 2 (only for the observations in field 1) indicates that the region leading has a higher Σ_{SFR}. This result is in good agreement with Martínez-García et al. (2009), who used a reddening-free photometric index (Q) to trace the variation of the stars formation across a spiral

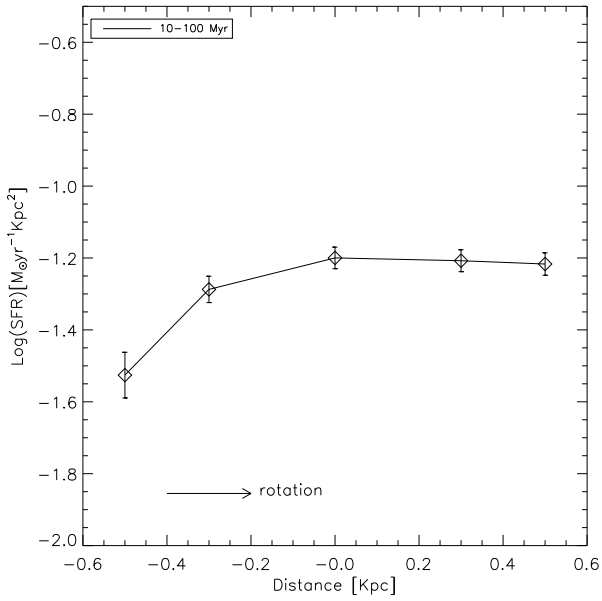

Figure 4.10: Variation of Σ_{SFR} across the Arm 2, observed in field 1. Variation averaged over the whole age range 10-100 Myr. Errors are the standard deviation of the mean.

arm, using a sample of 13 spiral galaxies. Both results are in agreement with the density wave theory, which suggested that the region hitting, either the gas or the spiral density wave, must induce a higher star formation due to the increase in the density of the gas.

We would like to thank Diederik Kruijssen and Juan Carlos Muñoz-Cuartas for insightful discussions that helped improve this article. This work was supported by an NWO VIDI grant to SL.

There is nothing more deceptive than an obvious fact.
–Arthur Conan Doyle

Chapter 5

Evidence of an interaction from resolved stellar population: The curious case of NGC 1313.

E. Silva-Villa & S. S. Larsen
To be submitted to *MNRAS*, 2011.

Abstract

The galaxy NGC 1313 has attracted the attention of various studies due to the peculiar morphology observed in optical bands, although it is classified as a barred, late-type galaxy with no apparent close-by companions. However, the velocity field suggests an interaction with a satellite companion. Using resolved stellar populations we aim to study different parts of the galaxy to understand further its morphology. Based on HST/ACS images, we estimated star formation histories by means of the synthetic CMD method in different areas in the galaxy. Incompleteness limit our studies to ages younger than $\sim$ 100Myr. Stars in the red and blue He burning phases are used to trace the distribution of recent star formation. Star formation histories suggest a burst in the southern-west region. We support the idea that NGC 1313 is experiencing an interaction with a satellite companion, observed as a tidal disrupted satellite galaxy in the south-west of NGC 1313. However, we do not observe any indication that suggested a perturbation due to the interaction with the satellite galaxy at other locations across the galaxy.

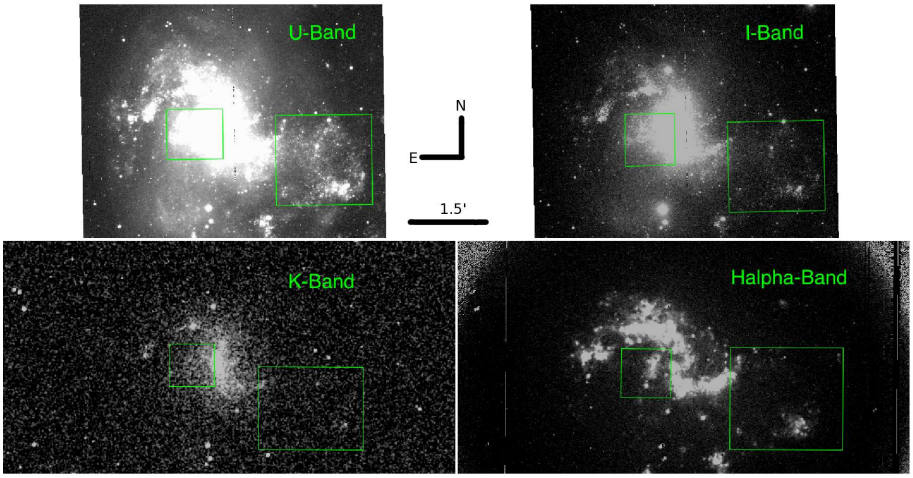

Figure 5.1: NGC 1313 observed through different filters. Images have arbitrary intensity scales, however, they all matched their WCS coordinates. Original sources of the images are: *U*: Las Campanas Observatory; *I*: Las Campanas Observatory; *K*: 2MASS Survey; and *Hα*: CTIO. Green boxes illustrate the areas discussed in this paper.

5.1. Introduction

The late type barred spiral galaxy NGC 1313 has been classified as a galaxy in transition between SBm and SBc by **?**. After observations in different bands, the peculiar morphology (see Fig. 5.1), the indications of a possible interaction with a satellite galaxy (e.g. Sandage & Brucato 1979) and the particular shape of the arms, called the attention of many studies.

Figure 5.1 shows NGC 1313 in the bands U, I, K, and Hα, using arbitrary intensity scales, but matching their WCS coordinates. Looking at the bar of the galaxy (see left small green boxes in Fig. 5.1) some issues call the attention: (1.) the bands U and Hα can trace recent star formation, and show to be enhanced in the bar and close to it; (2.) the bands I and K can trace intermediate/old populations (although, also relatively young) which appear to be stronger in the bar of the galaxy compared to the arms; (3.) the Hα image clearly shows a particular region next to the bar (east side) that does not appear to be connected neither with the bar nor with the arms; (4.) a detached region to the south-west is particularly prominent in the U-band image; and (5.) the bar and spiral arms are embedded in a faint, elongated region of diffuse light running from the south-east towards the north-west, visible in the U- and I-band images (see also Ryder et al. 1995). The surface brightness of this emission appears somewhat higher towards the southern part of the images in Fig. 5.1.

Due to the observed unusual morphology (e.g. Marcelin 1979, Blackman 1981), studies of this galaxy claimed for a displacement of the dynamical center of rotation

with respect to the optical center. However, accurate measurements of the velocity fields were presented by Peters et al. (1994) using HI and 1.4 GHz observations, showing that the galaxy presents a smooth velocity field in the regions close to the bar, contrary to the results presented by previous studies, concluding that there is not such displacement.

Comparing models and observations of velocity fields, Marcelin & Athanassoula (1982) estimated values of the M/L ratios. Marcelin & Athanassoula suggested lower values of M/L in the bar (3-10 times smaller) compared to the inner disc. This result, combined with their observation of a displacement in the bar was suggested as two different populations, one in the bar of the galaxy and a second one in the inner disc. Walsh & Roy (1997) suggest a possible enrichment in the bar of the galaxy based on (slightly higher, $\sim$ 0.2 dex) measurements of O/H, compared to the disc. Mollá & Roy (1999) used a multiphase chemical evolution model trying to reproduce the flat abundance gradient observed in NGC 1313 (Walsh & Roy 1997). Their model was not able to recover at the same time the abundance distribution, gas density and the star formation profiles obtain by observations, which makes the galaxy a particular and especial case to study.

The second important feature observed in Fig. 5.1 (right big green boxes) is the presence of an active region at the south-west part of the galaxy. Observing the bands U and Hα there is an indication of recent star formation activity in that particular region. Sandage & Brucato (1979) suggested the remnants of a tidally disrupted companion galaxy. The possibility of a satellite companion in process of interaction with NGC 1313 was also suggested by Blackman (1981). Blackman found that the velocity fields of NGC 1313 were inconsistent with pure rotation profiles, which is interpreted by Blackman as an indication of the presence of a satellite companion. Velocity fields obtain by Peters et al. (1994) show a clear disturbance over the south-west, suggesting an interaction between two galaxies. Observing the same region through the bands I and K it suggests the presence of previous populations in the region, which do not show to be connected to the southern arm of NGC 1313, possibly associated with the satellite galaxy. However, I and K bands can also trace red super giants (i.e. relatively young stars).

Larsen et al. (2007) studied resolved stellar population and (massive) star clusters in NGC 1313 using the same observations used in this paper. Larsen et al. suggested an increase in the star formation history over the south-west region of the galaxy (region covered by the right big green boxes in Fig. 5.1). The possible cause of the increase observed by Larsen et al. could be related with the tidal interaction observed by Marcelin (1979), Sandage & Brucato (1979), Blackman (1981) and Peters et al. (1994).

Based on *Hubble Space Telescope* (HST) observations, we study the galaxy NGC 1313, looking to understand further its morphology. Thanks to the superb resolution of the HST, we can use the resolved stellar population as a finger print of past events. We have observations of three main regions over the galaxy, covering the northern and southern arms, the bar of the galaxy, and the region that may have been disturbed by an interaction with a satellite companion. The location of our observations will

allow us to test and understand further the morphological features of NGC 1313. If there were any interaction and/or merger in the past, the resolved stellar populations can be use as tracers of the processes. We present our observations and photometry in Sect. 2. Using the colour-magnitude diagrams for the resolved stars, we devoted Sect. 3 to see what information can be extracted from there. We study the star formation histories of the different fields observed and for different group of stars in Sect. 4. We discussion our results, summary and conclusion in Sects. 5 and 6.

5.2. Observations and photometry

NGC 1313 was observed using the *Advanced Camera for Surveys* (ACS) onboard the the *Hubble Space Telescope* (HST) as part of the Cycle 12 in 2004. The instrument has a resolution of 0.'05 per pixel. With a distance modulus of 28.08 (~ 4Mpc, Méndez et al. 2002), 1 pixel corresponds to ~1 pc. Optical bands were covered using the filters F555W (~V), and F814W (~I), with exposure times of 680 sec for the V-band, and 676 sec for the I-band. Three main regions were targeted covering the north-east, center-east, and south-west (see Fig. 5.2).

Standard STScI pipeline was used for the initial data processing. ACS images were drizzled using the multidrizzle task (Koekemoer et al. 2002) in the STSDAS package in IRAF. We use the default parameters, but disabling the automatic sky subtraction. A full description of our procedures for object detection over the images can be found in Silva-Villa & Larsen (2010).

5.2.1. Field stars photometry

Stellar photometry was done by means of point-spread function (PSF) fitting photometry due to crowding. Visually inspecting the FWHM (with *imexam* in IRAF) a set of isolated bona-fide stars were used to construct the PSF in each band. PSF photometry was done with *DAOPHOT* in IRAF.

Our PSF-fitting magnitudes are corrected to a nominal aperture radius of 0.'5, following standard procedures. From this nominal value to infinity, we apply the corrections in Sirianni et al. (2005). HST zero-points[1] have been applied to the PSF magnitudes after applying aperture corrections. The zero-points used in this work are $ZP_B = 25.767$, $ZP_V = 25.727$ and $ZP_I = 25.520$ magnitudes. Typical errors of our photometry do not change dramatically from the ones in Silva-Villa & Larsen (2010, see its Fig. 2), and we refer the reader to that paper for more details about our photometry procedures.

The final V-I colour-magnitude diagrams (CMD) for the stars in the three fields are presented in Fig. 5.3 (first row). The colour-dependent 50% completeness limits for NGC 1313 were estimated in Silva-Villa & Larsen (2011), and are overplotted in Fig. 5.3 as dashed lines.

[1] www.stsci.edu/hst/acs/analisys/zeropints/#tablestart

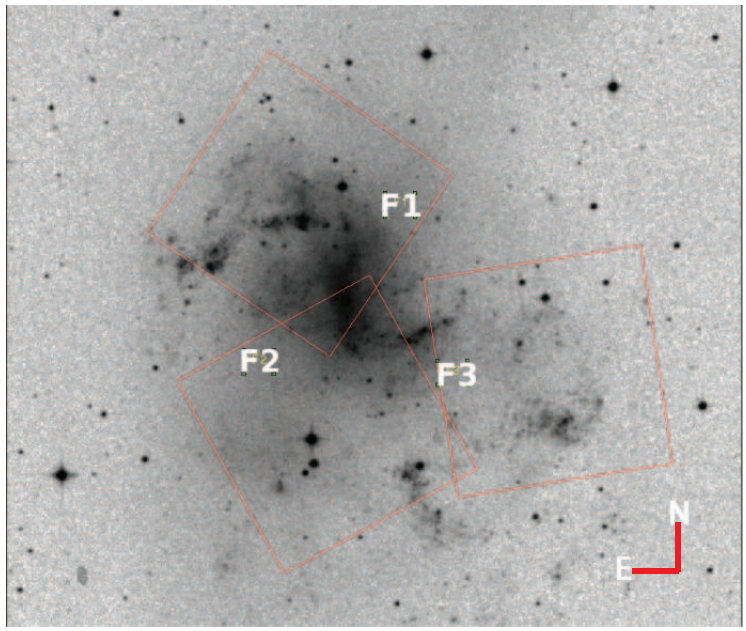

Figure 5.2: Digitalized Sky Survey image if NGC 1313 and ACS pointings used in this work.

5.3. What colour-Magnitude diagrams can tell us

A direct comparison among CMDs (see first row in Fig. 5.3) starts to indicate some differences across the galaxy. Observing the CMD of field 3, we observe a decrease in the number of stars between the phases RSG and RGB, which is not observed in the CMDs of the other two fields. This "gap" suggests that the star formation of the field 3 is different in comparison with the other two fields. Also, the density of stars in the young (i.e. main sequence) is different among the fields, being relatively higher in the field 3 compared to field 2, while having low crowding in the field 2. We try to observe further differences through the observations of the He burning phases among the fields and their spatial distribution.

Stars in the red and blue He burning phases (hereafter referred as R_{He} and B_{He} phases) are well age-dated by theoretical isochrones, and a comparison between these two group of stars and isochrones at different ages can (roughly) indicate how the recent star formation is distributed over the galaxy. Stars in the He burning phases has been used to trace star formation in other galaxies (e.g. Dohm-Palmer et al. 1997, for Sextant A), however, other features over the CMDs (e.g. the main sequences turn-off, sub-giant branches) are being used for the same purpose (see the review by Gallart et al. 2005, and references therein). Due to the distance of NGC 1313, we can not use all the possible features over the CMD to estimate/trace star formation histories, many of them fall below our completeness limits, so we focus the study in

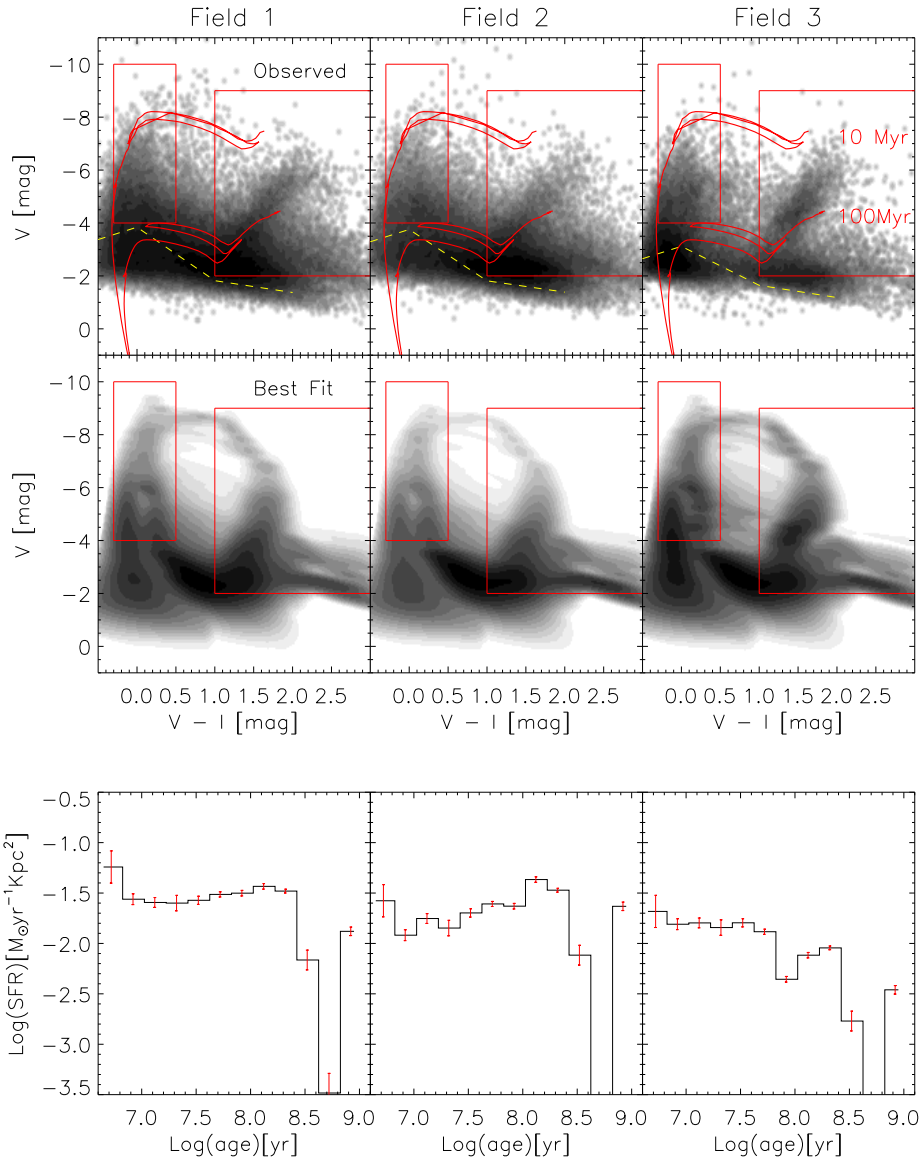

Figure 5.3: *First row*: CMDs for the three fields observed over NGC 1313. Dashed lines represent the colour-dependent 50% completeness limits. Red lines represent isochrones at 10 and 100 Myr. *Second row*: Best fit of the SFH. *Third row*: SFHs estimated in this paper. Error bars are poissonian, estimated by Silva-Villa & Larsen (2010).

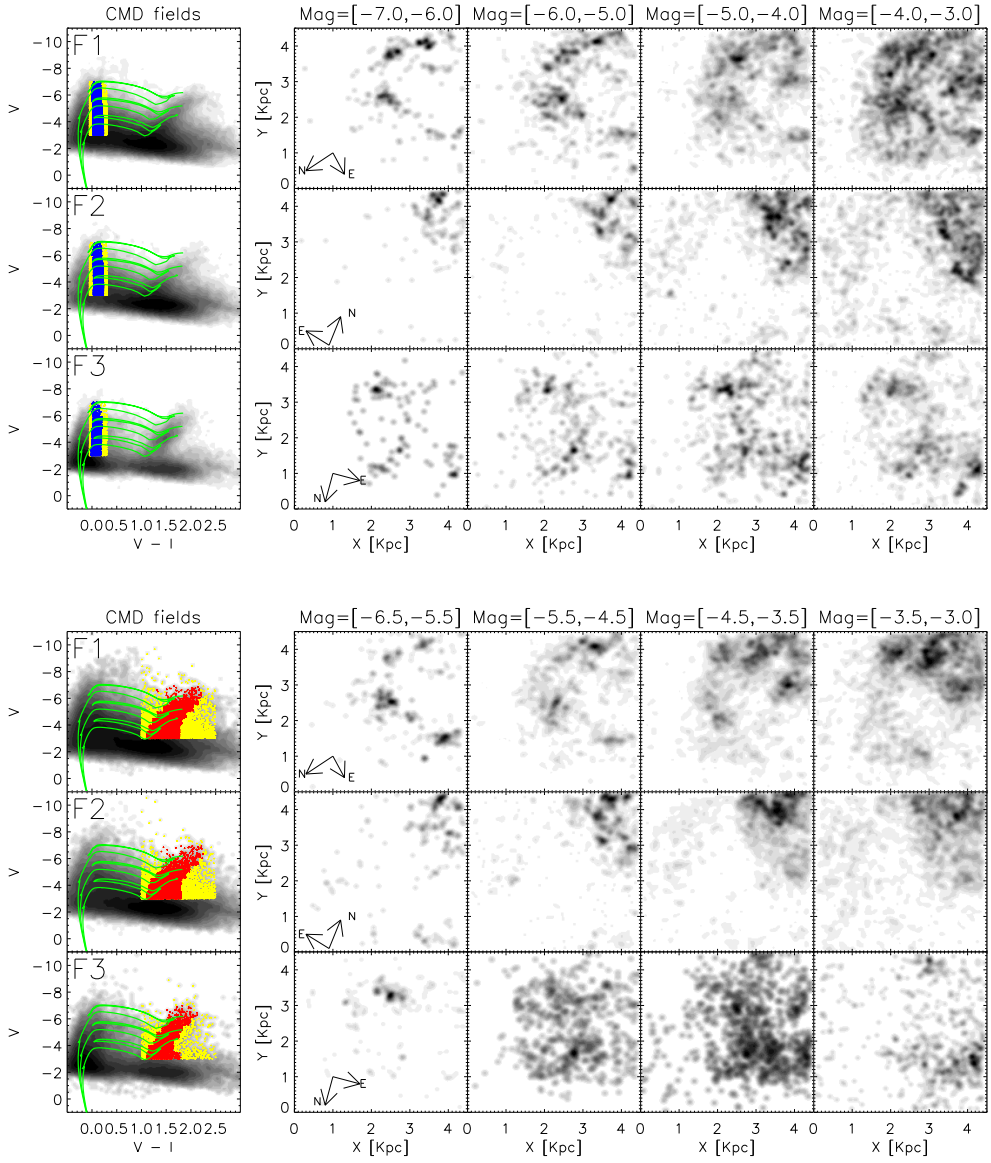

Figure 5.4: Blue and red He burning phases and how are the distributions with different magnitude bins. Padova 2008 (Marigo et al. 2008) isochrones for LMC-like metallicity are overplotted with at $log(\tau)$[yr]= [7.3, 7.6, 7.9].

this section on the use of the R_{He} and B_{He} phases.

We selected stars that could be in their He burning phases between the magnitudes intervals $-3 \geq M_V \geq -7$ and the colour ranges $-1 \leq$ (V-I) ≤ 2.5 and $-0.05 \leq$ (V-I) ≤ 0.3 for the red and blue sides, respectively. These two colour ranges were established by visual inspection, i.e. the B_{He} phases must be parallel to the main sequence stars, and on their right, while for the R_{He} phases regions are harder to enclose, so we used a larger colour range. The final sample of stars in the R_{He} and B_{He} side was obtained estimating the mean value of the color distribution and the 1σ deviation every 0.5 magnitudes in M_V. We illustrate our results in Figs. 5.4, where stars in yellow are stars outside the 1σ, while red and blue represent the two He burning phases respectively. Overplotted are three isochrones representing ages at $\tau = [10^{7.3}, 10^{7.6}, 10^{7.9}]$yr ($1^{st}$ column in Fig. 5.4), assuming LMC-like metallicity and using Padova 2008 isochrones (Marigo et al. 2008). To see how stars at different ages are distributed over the galaxy, we used stars close to each isochrones, separating them in the magnitude bins $M_V = [-6.5, -5.5, -4.5, -3.5, -3]$ and $M_V = [-7, -6, -5, -4, -3]$ for the R_{He} and B_{He}, respectively (see columns 2^{nd} to 5^{th} in Fig. 5.4). These bins roughly correlate with the three isochrones overplotted. Based on the spatial distributions of R_{He} and B_{He} at different magnitudes (i.e. different ages), we observe that:

- *Field 1*: The first two panels (from left to right for R_{He} and B_{He}) show that the brighter stars are concentrated in the northern arm of NGC 1313, however, the density of B_{He} appear to be larger as approaching the fainter magnitudes (last two panels on the right). This larger amount of stars in the fainter magnitudes for the B_{He} could be a consequence of contamination from main sequence stars, which are harder to separate at fainter magnitudes. The region indicated in Fig. 5.1 with an enhancement in Hα (small boxes in Fig. 5.1), is located around $(X, Y) \approx (4, 3)$Kpc. We observed how this region starts to be more visible when moving to the fainter magnitudes in the R_{He} panels, indicating a possible increase in the star formation in the past. Also observed in the R_{He} panels is an increase in the number of stars at the end of the arm ($(X, Y) \approx (4, 1.5)$Kpc, brighter panel). However, in a general view, the increase appear to be more continuos.

- *Field 2*: The spatial distribution of the stars appear to be separated into two regions, from $\sim$ 2Kpc to the left and to the right. It is important to note that there is no apparent formation of stars at the center of this field. These two statements are more clear in the B_{He} than in the R_{He}. Nevertheless, the concentrations are higher in the right side, where the bar is located. The region on the left resembles a stream of stars, however, this region is not connected neither with the arms of the galaxy nor with the bar.

- *Field 3*: In the youngest bin we see a region of active/very recent star formation towards the southern part of the field (at $(X, Y) \approx (2.5, 3.5)$). In the second bin we see a fairly smooth distribution of stars, many of which are found within an elongated structure with a radius of $\sim$ 1 kpc that is roughly centered on the

ACS field of view. The third bin shows an overdensity of stars towards the northern part of this structure (at $(X, Y) \approx (3, 1.5)$) and in the oldest bin most of the stars are associated with this overdensity. It thus appears that there has been a progression of star formation from the northern part of the field towards the south over the past 80-100 Myr.

Based on the distribution of the density of stars observed in the fields, we subdivided our fields to observe changes in the SFH that can give more information on the evolution of this galaxy:

- Our field 1 covers three main regions:
  (1.) *the bar*, located in our images between $(X_i, Y_i) = (1.5, 3.3)$ and $(X_f, Y_f) = (4.2, 4.2)$ Kpc; (2.) *the "Hα region"*, located in our images between $(X_i, Y_i) = (3.0, 2.2)$ and $(X_f, Y_f) = (4.1, 3.3)$ Kpc; and (3.) *the northern arm*, located in our images between $(X_i, Y_i) = (1.5, 1.0)$ and $(X_f, Y_f) = (4.2, 1.5)$ Kpc, removing the region covered by the *Hα region*.

- The field 2 covers two main regions:
  (1.) *the region R*, located in our images between $(X_i, Y_i) = (2.1, 1.0)$ and $(X_f, Y_f) = (4.2, 4.2)$ Kpc; and (2.) *the region L*, located in our images between $(X_i, Y_i) = (0.0, 1.0)$ and $(X_f, Y_f) = (2.2, 4.2)$ Kpc.

- The last field, field 3, covers two main regions:
  (1.) *the region U*, located in our images between $(X_i, Y_i) = (0.0, 2.1)$ and $(X_f, Y_f) = (3.7, 4.2)$ Kpc; and (2.) *the region D*, located in our images between $(X_i, Y_i) = (0.0, 0.0)$ and $(X_f, Y_f) = (3.7, 2.1)$ Kpc. Figure 5.5 presents the density of stars of each field and the subdivision used for further analysis.

CMDs for each of the subsections were created to see if they show any differences (see columns 2 and 3 in Fig. 5.5). Color-dependent completeness limits estimated by Silva-Villa & Larsen (2011) and isochrones at 10 and 100 Myr (Marigo et al. 2008) are overploted. We do not include the CMD of the northern arm over field 1 because it does not present any significant differences in comparison to the other regions in the same field. Between the bar of the galaxy and the Hα region located next to it (identified in Fig. 5.1, small green boxes), we do not see major differences. Both regions present a spread in absolute magnitude of the red and blue core He-burning stars, implying an age spread. However, the R_{He} phases of the bar reach magnitudes brighter than the Hα area suggesting higher star formation activity. Field 2 presents two regions, L and R. The CMDs of these regions present some differences. First, the difference in the density of stars in both areas is clear, where the R has a much larger number of stars. This is expected, because part of the bar of the galaxy is covered by the R region, as well as part of the southern arm. Differences in the population of stars among these two areas is clear, the tip of the main sequence and the R_{He} phases is much more brighter in the R than in the L, indicating the old population that belongs to the L. Also, the high density of stars in the RGB/AGB phases observed in the L indicate a very old population, and the low density of stars in the main

sequence indicates that either there is no star formation occurring at the moment or that the star formation rate is very low. The CMDs in the field 3, regions U and D, also show interesting characteristics. In the U region, the separation between the main sequence and the B_{He} phases is clearly visible, something not seen in any of the other CMDs presented. It also presents a very narrow R_{He} phases, which reaches magnitudes of $M_V \approx -7$. The region D presents also a large population of stars in the main sequence, however the population of stars in the RGB/AGB has a higher number of stars compared with the U. The location of D is close to the southern arm of NGC 1313, so the possibility of a combination of stars that do belong to the arm of the galaxy and stars that do not follow the arm distribution can cause this effect. Also important to note is that the peak of the R_{He} phases is ~ 0.5 magnitudes fainter in comparison with the U region, and the distribution is broader, suggesting a more constant formation process over time.

5.4. Star formation histories

We employ the synthetic CMD method (Tosi et al. 1991) to obtain the star formation histories (SFH). Our IDL-based program for the estimation of SFH was created and tested on the galaxy NGC 4395 (Silva-Villa & Larsen 2010). In a further study, Silva-Villa & Larsen (2011) studied the SFH of NGC 1313 (as a whole) as part of a sample of five galaxies and found a Σ_{SFR}=11.26×10^{-3} $M_\odot yr^{-1}Kpc^{-2}$. In comparison with the rest of the sample in Silva-Villa & Larsen, NGC 1313 is the second most active galaxy.

The parameters used to estimate the SFH in this paper are a distance modulus of 28.08, Magellanic Clouds-like metallicities ($Z = (0.004, 0.008)$, Walsh & Roy 1997), a binary fraction of 0.5 with a mass ratio between 0.1-0.9 (assuming a flat distribution and no binary evolution), a foreground extinction of A_b=0.47, and the colour combination V-I. We adopted Padova 2008 isochrones (Marigo et al. 2008). The results were normalized by the areas covered, having then the surface star formation rate density (Σ_{SFR} [$M_\odot yr^{-1}Kpc^{-2}$]).

The best fits obtained and the estimated SFHs for individual fields are presented in Fig. 5.3 (second and third row). In general, the SFH for the three fields are very similar, showing a constant star formation over time. However, there is an apparent increasing trend observed in the field 3. Our completeness limits are very close to the isochrones at 10^8 yr, so we do not assign any physical meaning to the "well" observed at $\sim 10^{8.7}$ yr.

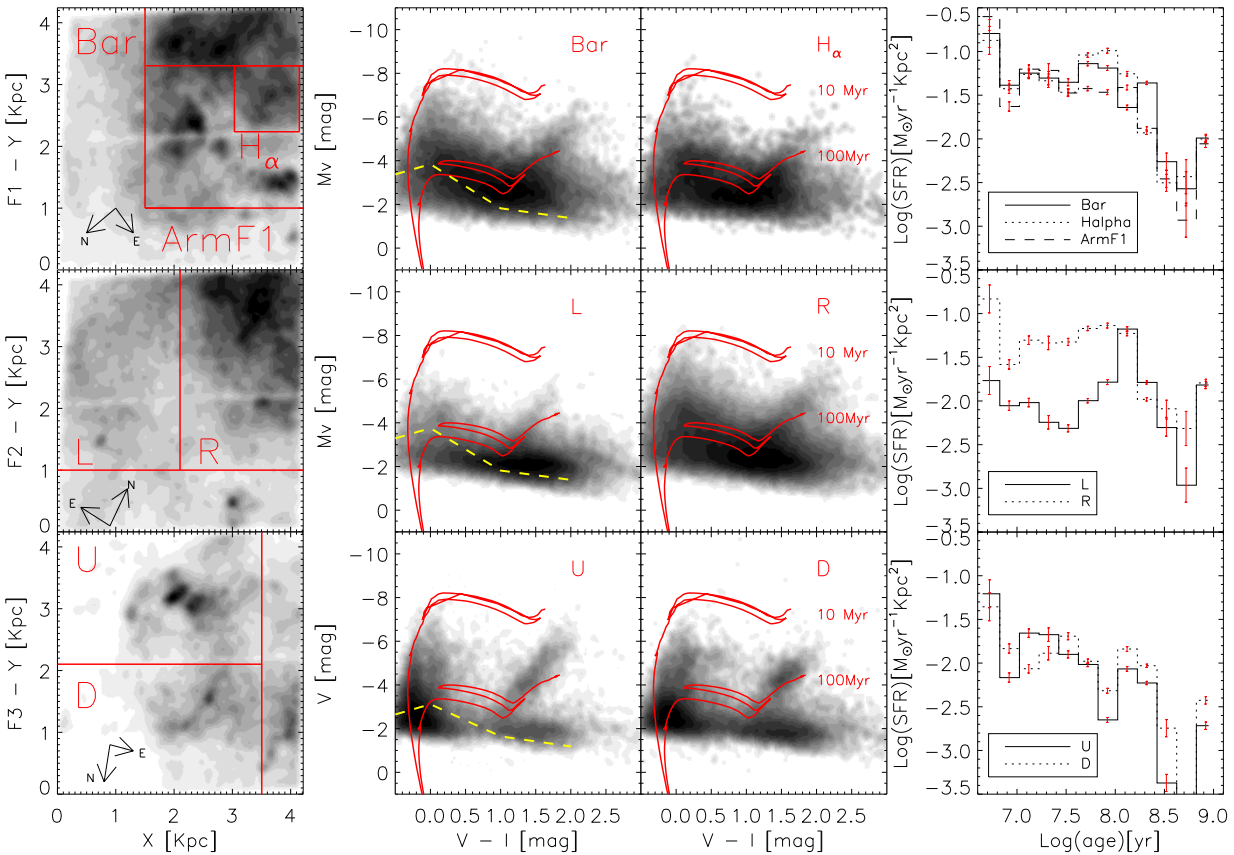

Figure 5.5: *Columns 1*: Density of stars over the three fields observed. The red lines indicate the subdivisions used to study different areas (see text for more details). *Column 2 and 3*: CMDs of the different areas. Red lines represent isochrones at 10 and 100 Myr (Marigo et al. 2008), and yellow dashed line is the 50% color-dependent completeness estimated by Silva-Villa & Larsen (2011). *Column 4*: Star formation histories. Error bars are Poissonian and were estimated in Silva-Villa & Larsen (2010).

Due to the differences observed in the CMDs in the previous section, we estimate SFHs for each of the subsections over our fields.

The Bar, Hα and Northern arm regions: Estimations of the three regions covered in our field 1 do not show a significant difference for ages between ∼10 and ∼40 Myr, however, we observe a difference of ≈0.4 dex from ∼40 up to 100 Myr (see column 4, Fig. 5.5) . The Hα region in the field appears to be disconnected from the bar and the arms of the galaxy, however the SFH observed in Fig. 5.5 shows a significance difference, showing even larger mean values (see table 5.1). Another important observation is the spatial distribution of the northern arm, which shows to be optically patchy. The SFH of the northern arm also shows a variation with respect the bar or the Hα regions. The three areas covered in the field 1 present a constant SFH between 10 and 100 Myr, where the estimations are less affected by incompleteness.

The R and L regions: The comparison between the regions L and R shows a more intriguing result. As observed in the density plots of the stars and the CMDs for these two regions in the field 2 (see column 1, 2, and 3, Fig. 5.5), the star formation history in the bar is different than in the apparent stream of stars located in the L region. The peak in the SFH observed at $\sim 10^{8.2}$ yr is very close to our completeness limits, so we do not assign any physical meaning. Nevertheless, the difference of about ∼ 1 dex for younger ages (≤100 Myr) indicates a different star formation rate for the two regions observed in this field.

The U and D regions: The two SFH for the regions U and D show a clear increase over time (see column 4, Fig. 5.5), but there is a significant difference among them, at least in the past ∼ 100 Myr. An increase in the SFH for NGC 1313 in the same region has been observed previously by Larsen et al. (2007), using the same dataset used in this work. Larsen et al. suggested the increase of the star formation based on two results: (1.) there is an increase in their estimations of the *relative* star formation, and (2.) they estimate the fraction between the number of "old" over "young" massive clusters (i.e. M≥ 5000 $M_\odot$), showing to have a higher value for the field 3 compare to the other two areas observed. We concluded that the increase in the SFH for the third field is a physical effect acting over the last ∼100 Myr.

Estimations of the mean values, and the respective standard deviation of the mean, for the full three fields and the subareas in each field are presented in table 5.1.

5.5. Discussion

Different wavelengths present the northern arm of NGC 1313 with a destroyed structure (i.e. patchy, see Fig. 5.1 and 5.2). The patchy shape observed in the northern arm (field 1) is curious for a spiral galaxy. Peters et al. (1994) found a loop of hydrogen around NGC 1313, which intersects the satellite companion. The result was interpreted by Peters et al. as the possible orbit followed by the (disrupted) companion galaxy. The orbit suggested by the authors passes from the northern arm and goes back down to the southern arm, showing to have an almost circular

Table 5.1: Mean values of Σ_{SFR} [$\times 10^{-3} M_{\odot} yr^{-1} Kpc^{-2}$] for the three fields and sub fields. Estimations are between 10 and 100 Myr.

Field/Subfield	Mean	STDDEV
Full field		
F1	30.9	3.2
F2	21.0	5.3
F3	14.9	5.1
Field 1		
Bar	54.8	12.1
H_{α}	60.9	28.7
Arm	42.0	16.0
Field 2		
R	51.7	16.8
L	9.2	4.1
Field 3		
U	12.4	7.9
D	11.9	5.3

orbit with a circular velocity ~ 105 Km/s. Assuming a circular orbit with radii 8 Kpc, the time to cover half orbit around NGC 1313 is ~ 237 Myr. We do not observe any physical features neither in the CMDs nor in the SFH of the field 1 that can suggest the pass of an object close to the northern arm. However, our measurements are constrain to the last 100 Myr due to incompleteness, so if the satellite galaxy passed by the northern arm, our data might not be enough to see the effects induce by this process. Nevertheless, the SFH increase observe in the field 3 in Fig. 5.5 ramps up around 100 Myr ago, which could be the results of the close encounter with NGC 1313.

The small active Hα region close to the bar (see small squares in Fig. 5.1) suggested recent activity in that particular location, which, visually, do not appear to be connected with neither of the arms of the galaxy, nor with the bar. We estimated the SFH of the Hα region, and found a slight difference among the bar, the northern arm and this region ($\leq$0.4 dex the largest difference), indicating that the whole area has been forming stars at (more or less) the same rate (see values in table 5.1 for bar, Arm, and Hα, and column 4 in Fig. 5.5).

Optical and Hα images indicate star formation activity in the bar of the galaxy. The study of the distribution of stars in the R_{He} and B_{He} phases (see Fig. 5.4), and the density maps (see Fig. 5.5), covered by our observations close to the bar (Field 2) suggests two different group of stars. This has been confirmed based on separated SFH for the regions L and R, which present a difference of ~ 1 dex for ages $\leq$ 100 Myr ago (see Fig. 5.5). The result observed in the SFHs was expected based on the difference in the amount of stars and their spatial distribution, which show a

large difference between the regions L and R. It remains puzzle the particular spatial distribution of the stream of stars in the L region because those stars do not appear linked with any of the two arms of the galaxy, not with the bar either.

The estimations by Marcelin & Athanassoula (1982) of the M/L in the bar compared to the estimations in the inner part of the disc showed to be 3-10 times smaller, which was interpreted by the authors as an indication of two different populations. A similar result was presented by Walsh & Roy (1997), where they observe (slightly, only $\sim$ 0.2 dex) higher levels of O/H in the bar compared to the arms, suggesting an enrichment process. A second interpretation of the results observed could come from the process of interaction that NGC 1313 is experiencing. There are no estimations of the time that NGC 1313 has been through the interaction, however, the pass of a companion galaxy close to the arms of NGC 1313 could induce an infall of gas to the center, to the bar.

5.5.1. Tidally disrupted satellite companion

The work done by Blackman (1981) and Peters et al. (1994) on the velocity fields of NGC 1313 suggested an interaction with a satellite companion at the south-west region of the galaxy. Larsen et al. (2007) observed an increase in the SFH at the same region. Our observations of this region have shown that the star formation (as a whole) presents lower levels compared to the ones obtain for the other two regions covered, however with an indication of an increase over time (see F1, F2, and F3 in table 5.1). Separating our field 3 into two different regions (U and D) we have shown that both are passing through an increase in their star formation history over the last 100 Myr, up to present times. This increase in the SFR may have been induce by tidal forces due to the interaction. We also note from Fig. 5.4 that the spatial distribution of the stars at young ages is not smooth, presenting a "ring" shape. Also, the fast increase in the number of stars in the first three panels in Fig. 5.4 (from left to right), suggests strong star formation activity in the past $\sim$ 80 Myr. However, the very last bin, which is close to 100 Myr, shows also a particular spatial distribution, with a very low number of stars, and a different spatial distribution when compared with the previous panels. This difference is observed on the CMD of the field 3 as a "gap" between the RSG and the RGB (see Fig. 5.3). The velocity fields presented by Peters et al. (1994) show a clear disturbance at the location of the satellite companion. We do not observe effects induce by the interaction (e.g. through tidal forces) on the CMDs/SFHs observed over NGC 1313, however our results are constrain up to $\sim$ 100 Myr due to incompleteness, which is a shorter time scale compared to the time needed to complete the orbit suggested by Peters et al. Our estimations only suggest a very fast increase in the star formation in the field 3 particularly (i.e. in the region no connected with NGC 1313), near NGC 1313. To fully understand what happened in the south-west region of NGC 1313, a numerical simulation will be needed.

In general, we do not see evidence of a pass of a satellite companion close to NGC 1313, based on our SFHs as suggested by Peters et al. (1994). We can, in general, say that the regions Bar, Hα, Arm (field 1), and R present the same levels

of SFRs (in the age range 10 to 100 Myr), meaning that we are observing a normal star formation activity in a spiral galaxy, with no indication of disturbance in the age range studied (i.e. fairly constant). The regions L, U, and D present similar levels in their SFH, which are low compared to the ones observed in the other regions (see table 5.1). The differences between the U and D in the field 3 and L in field 2 is that the former two present an increase in the last 100 Myr, while the later does not.

5.6. Summary and conclusions

Using HST/ACS observations in the bands V and I we have studied the stellar population of NGC 1313. Applying the synthetic CMD method (Tosi et al. 1991) we estimated the star formation histories over the past 100 Myr in three different regions of the galaxy.

We used the red and blue He burning phases as tracers of the star formation thanks to the well age-dated signatures based on theoretical isochrones, and observed different areas over the fields of NC 1313. Field 1 shows a roughly constant activity in the arm, the bar and the Hα region. The second field showed two separate group of stars, one of them (the L region) showing to be no connected with the bar or any of the arms of the galaxy. Field 3 showed a population that is not connected with the southern arm of the galaxy, but that has experienced a recent burst of star formation.

Observations of a large group of stars in the east region of the bar and in the bar itself suggest two different star formation histories, where the stars outside the bar suffered a rapid decrease in their star formation activity. The difference in the star formation history of these two groups (inside and outside the bar) is close to ~ 0.8 dex suggesting that a different population is present. For older ages, incompleteness constrain our results. High levels of O/H in the bar compared to the inner disk found by Walsh & Roy (1997) was suggested as an indication of recent enrichment. Also, the smaller values for the M/L estimated by Marcelin & Athanassoula (1982) were interpreted as two different populations across NGC 1313.

The SFHs obtain from the study of resolved stellar populations done in this work agree with the idea of an interaction process in the past of NGC 1313 with a tidally disrupted satellite companion.. The SFH in the region where the satellite companion is located shows an increase during the last 100 Myr, while the rest of the galaxy (i.e. the bar and the arms) present a constant SFH during the same time range.

This work was supported by an NWO VIDI grant to SL.

También esta noche, tierra, permanecsite firme.
Y ahora renaces de nuevo a mi alrededor.
Y alientas otra vez en mi la aspiración de luchar
sin descanso por una altísima existencia.

— Fausto

Bibliography

Adamo, A., Ostlin, G., Zackrisson, E., & Hayes, M. 2011, ArXiv e-prints (cited on pages 7, 8, and 84)

Anders, P., Bissantz, N., Fritze-v. Alvensleben, U., & de Grijs, R. 2004, MNRAS, 347, 196 (cited on pages 13, 45, 68, and 73)

Anders, P. & Fritze-v. Alvensleben, U. 2003, Astron. Astrophys., 401, 1063 (cited on pages 29 and 61)

Annibali, F., Tosi, M., Monelli, M., et al. 2009, Astron. J., 138, 169 (cited on page 20)

Aparicio, A. & Gallart, C. 2004, Astron. J., 128, 1465 (cited on page 35)

Aparicio, A., Gallart, C., & Bertelli, G. 1997, Astron. J., 114, 669 (cited on page 35)

Aparicio, A. & Hidalgo, S. L. 2009, Astron. J., 138, 558 (cited on page 35)

Barker, M. K., Sarajedini, A., Geisler, D., Harding, P., & Schommer, R. 2007, Astron. J., 133, 1138 (cited on page 20)

Barmby, P., Perina, S., Bellazzini, M., et al. 2009, Astron. J., 138, 1667 (cited on page 85)

Bastian, N. 2008, MNRAS, 390, 759 (cited on pages 7, 8, 21, 48, and 53)

Bastian, N. & Gieles, M. 2008, in Astronomical Society of the Pacific Conference Series, Vol. 388, Mass Loss from Stars and the Evolution of Stellar Clusters, ed. A. de Koter, L. J. Smith, & L. B. F. M. Waters, 353 (cited on page 20)

Baumgardt, H. 2009, Dissolution of Globular Clusters, ed. Richtler, T. & Larsen, S., 387 (cited on page 20)

Bertelli, G., Bressan, A., Chiosi, C., Fagotto, F., & Nasi, E. 1994, Astron. Astrophys. Suppl., 106, 275 (cited on page 29)

Bertin, E. & Arnouts, S. 1996, Astron. Astrophys. Suppl., 117, 393 (cited on pages 24 and 58)

Blackman, C. P. 1981, MNRAS, 195, 451 (cited on pages 108, 109, and 120)

Boutloukos, S. G. & Lamers, H. J. G. L. M. 2003, MNRAS, 338, 717 (cited on pages 7, 12, 20, 54, and 77)

Bresolin, F., Ryan-Weber, E., Kennicutt, R. C., & Goddard, Q. 2009, Astrophys. J., 695, 580 (cited on page 56)

Bressert, E., Bastian, N., Gutermuth, R., et al. 2010, MNRAS, 409, L54 (cited on pages 7, 8, and 53)

Brown, T. M., Beaton, R., Chiba, M., et al. 2008, Astrophys. J. Lett., 685, L121 (cited on pages 11, 20, and 55)

Buat, V. & Xu, C. 1996, Astron. Astrophys., 306, 61 (cited on page 45)

Calzetti, D., Wu, S., Hong, S., et al. 2010, ArXiv e-prints (cited on pages 56, 73, and 90)

Carroll, B. W. & Ostlie, D. A. 2006, An introduction to modern astrophysics and cosmology, ed. Carroll, B. W. & Ostlie, D. A. (cited on page 10)

Cepa, J. & Beckman, J. E. 1990, Astrophys. J., 349, 497 (cited on page 90)

Cerviño, M. & Luridiana, V. 2006, Astron. Astrophys., 451, 475 (cited on pages 29, 68, and 70)

Chandar, R., Fall, S. M., & Whitmore, B. C. 2006, Astrophys. J. Lett., 650, L111 (cited on page 13)

Chandar, R., Whitmore, B. C., Kim, H., et al. 2010, Astrophys. J., 719, 966 (cited on pages 13, 58, 78, and 85)

Cignoni, M. & Tosi, M. 2010, Advances in Astronomy, 2010, 3 (cited on page 39)

Cole, A. A., Skillman, E. D., Tolstoy, E., et al. 2007, Astrophys. J. Lett., 659, L17 (cited on page 20)

Craig, I. J. D. & Brown, J. C. 1986, Inverse problems in astronomy: A guide to inversion strategies for remotely sensed data, ed. Craig, I. J. D. & Brown, J. C. (cited on page 3)

Crosthwaite, L. P., Turner, J. L., Buchholz, L., Ho, P. T. P., & Martin, R. N. 2002, Astron. J., 123, 1892 (cited on pages 95 and 99)

de Grijs, R., Anders, P., Lamers, H. J. G. L. M., et al. 2005, MNRAS, 359, 874 (cited on page 70)

de Grijs, R. & Goodwin, S. P. 2008, MNRAS, 383, 1000 (cited on page 54)

Dobbs, C. L. & Pringle, J. E. 2010, MNRAS, 409, 396 (cited on page 7)

Dohm-Palmer, R. C., Skillman, E. D., Saha, A., et al. 1997, Astron. J., 114, 2527 (cited on pages 6 and 111)

Dolphin, A. 1997, New Astronomy, 2, 397 (cited on pages 11, 20, 35, and 54)

Dolphin, A. E. 2000, Publ. Astron. Soc. Pac., 112, 1397 (cited on page 27)

Edvardsson, B., Andersen, J., Gustafsson, B., et al. 1993, Astron. Astrophys., 275, 101 (cited on page 20)

Eldridge, J. J. & Stanway, E. R. 2009, MNRAS, 400, 1019 (cited on page 70)

Elmegreen, B. G. 2008, 388, 249 (cited on page 20)

Elmegreen, B. G. 2011a, ArXiv e-prints (cited on page 102)

Elmegreen, B. G. 2011b, ArXiv e-prints (cited on page 6)

Elmegreen, B. G. & Hunter, D. A. 2010, Astrophys. J., 712, 604 (cited on pages 11 and 13)

Elson, R. A. W., Freeman, K. C., & Lauer, T. R. 1989, Astrophys. J. Lett., 347, L69 (cited on page 85)

Fall, S. M. 2004, in Astronomical Society of the Pacific Conference Series, Vol. 322, The Formation and Evolution of Massive Young Star Clusters, ed. H. J. G. L. M. Lamers, L. J. Smith, & A. Nota, 399–+ (cited on pages 53, 54, 58, and 77)

Fall, S. M. 2006, Astrophys. J., 652, 1129 (cited on page 20)

Fall, S. M., Chandar, R., & Whitmore, B. C. 2005, Astrophys. J. Lett., 631, L133 (cited on pages 7, 11, 12, and 13)

Fall, S. M., Chandar, R., & Whitmore, B. C. 2009, Astrophys. J., 704, 453 (cited on page 77)

Filippenko, A. V. & Sargent, W. L. W. 1989, Astrophys. J. Lett., 342, L11 (cited on page 22)

Forbes, D. A., Brodie, J. P., & Huchra, J. 1997, Astron. J., 113, 887 (cited on page 28)

Fouesneau, M. & Lançon, A. 2010, Astron. Astrophys., 521, A22+ (cited on pages 13 and 68)

Foyle, K., Rix, H., Walter, F., & Leroy, A. K. 2010, Astrophys. J., 725, 534 (cited on page 90)

Gallart, C., Zoccali, M., & Aparicio, A. 2005, Annu. Rev. Astron. Astrophys., 43, 387 (cited on pages 6, 9, 10, and 111)

Gieles, M. 2010, in Astronomical Society of the Pacific Conference Series, Vol. 423, Astronomical Society of the Pacific Conference Series, ed. B. Smith, J. Higdon, S. Higdon, & N. Bastian, 123–+ (cited on pages 7, 8, 14, 21, 48, 53, 55, and 75)

Gieles, M., Athanassoula, E., & Portegies Zwart, S. F. 2007, MNRAS, 376, 809 (cited on page 54)

Gieles, M. & Bastian, N. 2008, Astron. Astrophys., 482, 165 (cited on pages 7, 14, 21, 48, and 53)

Gieles, M., Portegies Zwart, S. F., Baumgardt, H., et al. 2006, MNRAS, 371, 793 (cited on pages 11 and 54)

Girardi, L., Bertelli, G., Bressan, A., et al. 2002, Astron. Astrophys., 391, 195 (cited on page 74)

Girardi, L., Bressan, A., Bertelli, G., & Chiosi, C. 2000, Astron. Astrophys. Suppl., 141, 371 (cited on page 45)

Girardi, L., Chiosi, C., Bertelli, G., & Bressan, A. 1995, Astron. Astrophys., 298, 87 (cited on page 29)

Goddard, Q. E., Bastian, N., & Kennicutt, R. C. 2010, MNRAS, 405, 857 (cited on pages 7, 8, 14, 48, 49, 53, 55, 82, 83, 84, and 86)

Grevesse, N. & Sauval, A. J. 1998, Space Science Reviews, 85, 161 (cited on page 26)

Harris, J., Calzetti, D., Gallagher, III, J. S., Conselice, C. J., & Smith, D. A. 2001, Astron. J., 122, 3046 (cited on pages 56 and 90)

Harris, J. & Zaritsky, D. 2001, Astrophys. J. Suppl., 136, 25 (cited on pages 6, 11, 20, and 54)

Harris, J. & Zaritsky, D. 2002, in Astronomical Society of the Pacific Conference Series, Vol. 274, Observed HR Diagrams and Stellar Evolution, ed. T. Lejeune & J. Fernandes, 600 (cited on page 35)

Harris, J. & Zaritsky, D. 2004, Astron. J., 127, 1531 (cited on pages 11, 20, 48, and 54)

Harris, J. & Zaritsky, D. 2009, Astron. J., 138, 1243 (cited on pages 11, 20, and 55)

Kaltcheva, N. 2009, Publ. Astron. Soc. Pac., 121, 1326 (cited on pages 6 and 90)

Kennicutt, Jr., R. C. 1998, Astrophys. J., 498, 541 (cited on page 6)

King, I. 1962, Astron. J., 67, 471 (cited on pages 24, 31, and 64)

Knapen, J. H., Beckman, J. E., Cepa, J., & Nakai, N. 1996, Astron. Astrophys., 308, 27 (cited on page 90)

Koekemoer, A. M., Fruchter, A. S., Hook, R. N., & Hack, W. 2002, in The 2002 HST Calibration Workshop : Hubble after the Installation of the ACS and the NICMOS Cooling System, ed. S. Arribas, A. Koekemoer, & B. Whitmore, 337 (cited on pages 23, 58, 91, and 110)

Konstantopoulos, I. S., Bastian, N., Gieles, M., & Lamers, H. J. G. L. M. 2010, in IAU Symposium, Vol. 266, IAU Symposium, ed. R. de Grijs & J. R. D. Lépine, 433–437 (cited on page 13)

Kroupa, P. 2002, Science, 295, 82 (cited on pages 63, 72, and 73)

Kruijssen, J. M. D., Inti Pelupessy, F., Lamers, H. J. G. L. M., Portegies Zwart, S. F., & Icke, V. 2011, ArXiv e-prints (cited on pages 11 and 13)

Kruijssen, J. M. D. & Lamers, H. J. G. L. M. 2008, in Astronomical Society of the Pacific Conference Series, Vol. 396, Astronomical Society of the Pacific Conference Series, ed. J. G. Funes & E. M. Corsini, 149–+ (cited on page 7)

Lada, C. J. & Lada, E. A. 2003, Annu. Rev. Astron. Astrophys., 41, 57 (cited on pages 7, 8, 11, 20, 21, and 53)

Lamers, H. J. G. L. M. 2009, Astrophysics and Space Science, 132 (cited on pages 12, 13, and 54)

Lamers, H. J. G. L. M. & Gieles, M. 2008, in Astronomical Society of the Pacific Conference Series, Vol. 388, Mass Loss from Stars and the Evolution of Stellar Clusters, ed. A. de Koter, L. J. Smith, & L. B. F. M. Waters, 367 (cited on pages 21 and 53)

Lamers, H. J. G. L. M., Gieles, M., Bastian, N., et al. 2005, Astron. Astrophys., 441, 117 (cited on pages 7, 11, 12, 20, 54, 76, 77, and 79)

Larsen, S. S. 1999, Astron. Astrophys. Suppl., 139, 393 (cited on pages 24, 30, 59, 62, and 64)

Larsen, S. S. 2009, Astron. Astrophys., 503, 467 (cited on pages 47, 75, and 77)

Larsen, S. S., Efremov, Y. N., Elmegreen, B. G., et al. 2002, Astrophys. J., 567, 896 (cited on page 35)

Larsen, S. S., Forbes, D. A., & Brodie, J. P. 2001, MNRAS, 327, 1116 (cited on page 28)

Larsen, S. S., Mora, M. D., Brodie, J. P., & Richtler, T. 2007, in IAU Symposium, Vol. 241, IAU Symposium, ed. A. Vazdekis & R. F. Peletier, 435–439 (cited on pages 7, 11, 20, 55, 56, 109, 118, and 120)

Larsen, S. S. & Richtler, T. 1999, Astron. Astrophys., 345, 59 (cited on pages 22, 46, 56, and 58)

Larsen, S. S. & Richtler, T. 2000, Astron. Astrophys., 354, 836 (cited on pages 7, 8, 22, 45, 56, 58, 73, 83, 84, and 90)

Lejeune, T. & Schaerer, D. 2001, Astron. Astrophys., 366, 538 (cited on page 35)

Leroy, A. K., Walter, F., Brinks, E., et al. 2008, Astron. J., 136, 2782 (cited on page 90)

Lin, C. C. & Shu, F. H. 1964, Astrophys. J., 140, 646 (cited on pages 6, 90, and 102)

Lord, S. D. & Young, J. S. 1990, Astrophys. J., 356, 135 (cited on page 90)

Lundgren, A. A., Olofsson, H., Wiklind, T., & Beck, R. 2008, in Astronomical Society of the Pacific Conference Series, Vol. 390, Pathways Through an Eclectic Universe, ed. J. H. Knapen, T. J. Mahoney, & A. Vazdekis, 144–+ (cited on pages 91, 101, and 104)

Lundgren, A. A., Wiklind, T., Olofsson, H., & Rydbeck, G. 2004, Astron. Astrophys., 413, 505 (cited on pages 91, 93, 95, 96, 99, and 103)

Mackey, A. D. & Gilmore, G. F. 2003a, MNRAS, 338, 120 (cited on page 85)

Mackey, A. D. & Gilmore, G. F. 2003b, MNRAS, 338, 85 (cited on page 85)

Maeder, A. & Meynet, G. 2008, in Astronomical Society of the Pacific Conference Series, Vol. 388, Mass Loss from Stars and the Evolution of Stellar Clusters, ed. A. de Koter, L. J. Smith, & L. B. F. M. Waters, 3–+ (cited on page 70)

Maíz Apellániz, J. 2009, Astrophys. J., 699, 1938 (cited on pages 13, 29, 54, 68, 70, and 80)

Marcelin, M. 1979, Academie des Science Paris Comptes Rendus Serie B Sciences Physiques, 289, 29 (cited on pages 108 and 109)

Marcelin, M. & Athanassoula, E. 1982, Astron. Astrophys., 105, 76 (cited on pages 109, 120, and 121)

Marigo, P., Girardi, L., Bressan, A., et al. 2008, Astron. Astrophys., 482, 883 (cited on pages 6, 11, 26, 30, 35, 64, 68, 72, 113, 114, 115, 116, and 117)

Martínez-García, E. E., González-López lira, R. A., & Bruzual-A, G. 2009, Astrophys. J., 694, 512 (cited on pages 7, 90, 102, 103, and 104)

Mateo, M. L. 1998, Annu. Rev. Astron. Astrophys., 36, 435 (cited on page 20)

McGruder, III, C. H. 1975, Astron. Astrophys., 43, 51 (cited on page 90)

Méndez, B., Davis, M., Moustakas, J., et al. 2002, Astron. J., 124, 213 (cited on page 110)

Meurer, G. R., Hanish, D. J., Ferguson, H. C., et al. 2006, Astrophys. J. Suppl., 165, 307 (cited on pages 92 and 93)

Meurer, G. R., Heckman, T. M., Leitherer, C., et al. 1995, Astron. J., 110, 2665 (cited on pages 7 and 8)

Meyer, M. J., Zwaan, M. A., Webster, R. L., et al. 2004, MNRAS, 350, 1195 (cited on page 92)

Mollá, M. & Roy, J. 1999, Astrophys. J., 514, 781 (cited on page 109)

Mora, M. D., Larsen, S. S., & Kissler-Patig, M. 2007, Astron. Astrophys., 464, 495 (cited on pages 13, 27, 31, 56, 58, 65, and 66)

Mora, M. D., Larsen, S. S., & Kissler-Patig, M. 2008, Astron. Astrophys., 489, 1065 (cited on pages 58, 75, and 81)

Mora, M. D., Larsen, S. S., Kissler-Patig, M., Brodie, J. P., & Richtler, T. 2009, Astron. Astrophys., 501, 949 (cited on pages 13, 21, 22, 27, 29, 31, 32, 33, 46, 56, 58, 65, 66, 68, 78, and 84)

Morgan, W. W., Whitford, A. E., & Code, A. D. 1953, Astrophys. J., 118, 318 (cited on pages 5 and 90)

Muzzio, J. C. 1979, Astron. J., 84, 639 (cited on page 90)

Pellerin, A., Meyer, M., Harris, J., & Calzetti, D. 2007, Astrophys. J. Lett., 658, L87 (cited on pages 53 and 85)

Peters, W. L., Freeman, K. C., Forster, J. R., Manchester, R. N., & Ables, J. G. 1994, MNRAS, 269, 1025 (cited on pages 109, 118, and 120)

Piskunov, A. E., Kharchenko, N. V., Schilbach, E., et al. 2009, Astron. Astrophys., 507, L5 (cited on pages 13, 54, and 70)

Popescu, B. & Hanson, M. M. 2010a, ArXiv e-prints (cited on pages 68 and 70)

Popescu, B. & Hanson, M. M. 2010b, Astrophys. J. Lett., 713, L21 (cited on pages 13, 68, and 70)

Porras, A., Christopher, M., Allen, L., et al. 2003, Astron. J., 126, 1916 (cited on pages 7 and 53)

Rejkuba, M., Greggio, L., & Zoccali, M. 2004, Astron. Astrophys., 415, 915 (cited on page 20)

Roberts, W. W. 1969, Astrophys. J., 158, 123 (cited on pages 6, 90, and 102)

Roy, J., Belley, J., Dutil, Y., & Martin, P. 1996, Astrophys. J., 460, 284 (cited on page 26)

Ryder, S. D., Staveley-Smith, L., Malin, D., & Walsh, W. 1995, Astron. J., 109, 1592 (cited on page 108)

Salpeter, E. E. 1955, Astrophys. J., 121, 161 (cited on pages 29, 36, 45, and 102)

Sandage, A. & Brucato, R. 1979, Astron. J., 84, 472 (cited on pages 108 and 109)

Schechter, P. 1976, Astrophys. J., 203, 297 (cited on page 75)

Scheepmaker, R. A., Lamers, H. J. G. L. M., Anders, P., & Larsen, S. S. 2009, Astron. Astrophys., 494, 81 (cited on pages 70 and 94)

Schlegel, D. J., Finkbeiner, D. P., & Davis, M. 1998, Astrophys. J., 500, 525 (cited on pages 22 and 56)

Schmidt, M. 1959, Astrophys. J., 129, 243 (cited on page 6)

Schulz, J., Fritze-v. Alvensleben, U., Möller, C. S., & Fricke, K. J. 2002, Astron. Astrophys., 392, 1 (cited on pages 45 and 73)

Shapley, H. 1916, Contributions from the Mount Wilson Observatory / Carnegie Institution of Washington, 115, 1 (cited on page 6)

Silva-Villa, E. & Larsen, S. S. 2010, Astron. Astrophys., 516, A10+ (cited on pages 55, 93, 94, 96, 99, 100, 110, 112, 116, and 117)

Silva-Villa, E. & Larsen, S. S. 2011, Astron. Astrophys., 529, A25+ (cited on pages 7, 8, 13, 21, 90, 96, 110, 115, 116, and 117)

Sirianni, M., Jee, M. J., Benítez, N., et al. 2005, Publ. Astron. Soc. Pac., 117, 1049 (cited on pages 32, 33, 68, 93, and 110)

Skillman, E. D. & Gallart, C. 2002, in Astronomical Society of the Pacific Conference Series, Vol. 274, Observed HR Diagrams and Stellar Evolution, ed. T. Lejeune & J. Fernandes, 535 (cited on pages 11, 20, and 35)

Spitzer, L. 1987, Dynamical evolution of globular clusters, ed. L. Spitzer (cited on pages 7, 11, 20, and 53)

Thim, F., Tammann, G. A., Saha, A., et al. 2003, Astrophys. J., 590, 256 (cited on page 91)

Tosi, M., Greggio, L., Marconi, G., & Focardi, P. 1991, Astron. J., 102, 951 (cited on pages 11, 20, 35, 54, 71, 96, 104, 116, and 121)

Walsh, J. R. & Roy, J. 1997, MNRAS, 288, 726 (cited on pages 56, 109, 116, 120, and 121)

Whitmore, B. C. 2007, in IAU Symposium, Vol. 237, IAU Symposium, ed. B. G. Elmegreen & J. Palous, 222–229 (cited on pages 7, 11, 12, 13, and 20)

Whitmore, B. C., Chandar, R., & Fall, S. M. 2007, Astron. J., 133, 1067 (cited on pages 54 and 77)

Williams, B. F., Dalcanton, J. J., Seth, A. C., et al. 2009, Astron. J., 137, 419 (cited on page 20)

Young, L. M., Skillman, E. D., Weisz, D. R., & Dolphin, A. E. 2007, Astrophys. J., 659, 331 (cited on page 20)

Zaritsky, D., Kennicutt, Jr., R. C., & Huchra, J. P. 1994, Astrophys. J., 420, 87 (cited on page 56)

Zepf, S. E., Ashman, K. M., English, J., Freeman, K. C., & Sharples, R. M. 1999, Astron. J., 118, 752 (cited on page 7)

Zhang, Q. & Fall, S. M. 1999, Astrophys. J. Lett., 527, L81 (cited on page 77)

English Summary

Since astronomers have realized that the Milky Way is one galaxy among many, they have tried to understand how these particular systems are formed and how they evolve. However, this is not a straightforward task. To understand galaxy formation and evolution, we need to understand how the different parts of a galaxy are related (i.e. the stars and the gas that compose a galaxy) and how their interaction lead to the observable signatures that characterize them.

The structure of spiral galaxies was initially studied using the spatial distribution of field stars and star clusters in the Milky Way. Young field stars turned out to be concentrated in the arms of the Galaxy. Observations of star clusters showed that the young star clusters were located in the disk of the galaxy, while the old star clusters were distributed outside of the disk, in the halo of the galaxy. But our location inside the disk of the galaxy prevent us to have a full study over the Milky Way. For that reason, we also perform these studies in other galaxies.

Many studies on the structure and past activity of galaxies have used integrated light of stellar populations. As a new approach, we aim to use resolved stellar populations to study how the distribution of the stars are related with different parameters of the galaxy. We also present studies of star clusters, which combined with the resolved field star populations will improve the understanding on the processes that shape galaxies. In our case, spiral galaxies are the main target. As an illustrative example, Fig. A.1 shows a small field in the direction of the center of the Milky Way, with a number of field stars distributed over the image. In the same figure also a star cluster is shown, the globular star cluster M13.

The study of resolved stellar populations in extragalactic environments can be done thanks to our knowledge of the physical processes that govern stellar evolution. Some properties can be combined and compared in a diagram called the Color-Magnitude Diagram (CMD). The CMD indicates several properties of stellar populations, and is the main tool used here to understand the different aspects of the field stars in the studied galaxies. The power of the tool comes from the large amount of information that can be obtained when observed CMDs are compared with theoretical CMDs, through the use of a method named the *synthetic CMD method*.

In a similar way, the knowledge of star cluster evolution allows us to study the observed cluster populations in galaxies. To understand the properties of star clusters, we compare the observed properties of the clusters with theoretical models,

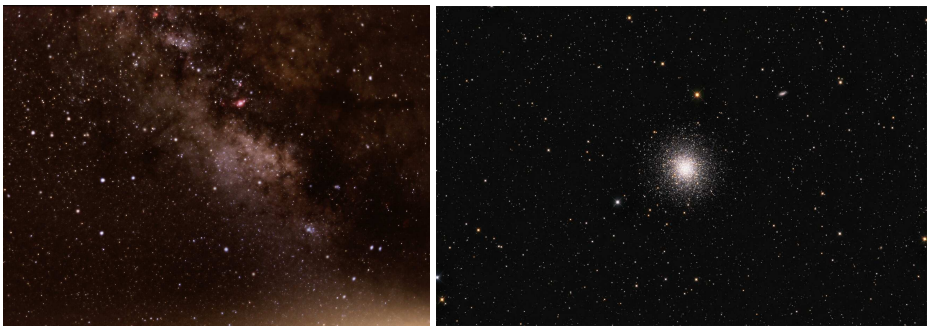

Figure A.1: *Left panel*: Field stars in the center of the Milky Way. Credits: P. van der Haar. *Right panel*: Star cluster M13. Credits: Thomas V. Davis

known as *Simple Stellar Population models* (SSP).

As described below, the use of star clusters and field stars will be a powerful tool to understand a number of different observed properties of spiral galaxies. We studied the nearby, face-on, spiral galaxies NGC 45, NGC 1313, NGC 4395, NGC 5236, and NGC 7793. The images used in this work were taken with the *Hubble Space Telescope* (HST). Two of the HST detectors were used, the Advanced Camera for Surveys and the Wide Field Planetary Camera 2, covering the optical wavelengths U, B, V and I.

Field stars and star clusters as indicators of past activity

During the last decades, astronomers followed the idea that most (if not all) stars are form in clusters. For that reason, star clusters have been used to trace back the formation history of galaxies. To understand how galaxies are formed and how they evolve, the use of field stars and star clusters can be employed, if we follow the idea that most stars were formed in clusters. To verify this, we need to find the (possible) correlations between field stars and star clusters. **Chapter 2** and **Chapter 3** are devoted to the study of resolved stellar populations and star clusters in the five galaxies studied in this thesis. The results show that the fraction of star formation that ends up in bound star clusters is below 10%. Studies of young stellar objects in the solar neighborhood indicate that some fraction of stars are in fact being formed in (bound) clusters, while some are no more than the low-mass end of a continuous smooth lognormal function distribution, where no different modes of star formation (i.e. field vs. clustered) were found. However, a relation between the amount of light coming from (young) star clusters and the fraction of stars formed in bound clusters showed to change between different environments, i.e. different galaxies. This suggests an underlying correlation between the host galaxy and the star clusters.

Field stars and the arms of a spiral galaxy

Spiral galaxies have always called our attention due to their spectacular shapes. At the end of the 1950s, it was found that young stars are concentrated in one of the arms of the Milky way, suggesting that the formation of stars might be enhanced in the arms. Also, previous studies of the spatial distribution of star clusters showed that young star clusters were preferentially located in the disk of the galaxy, while the old clusters were in the halo, suggesting larger activity in the disk. Theoretical models at the end of the 1960s explained how a propagation of a density wave was able to reproduce the spiral structure observed in galaxies. Using resolved stellar populations in the spiral galaxy NGC 5236 (M83) we studied in **Chapter 4** how the surface star formation rate density is connected with the arms of spiral galaxies. From the theoretical point, it is expected that when the density wave encounters the gas of the galaxy, star formation is trigged due to the compression of the gas. Previous studies suggested that the star formation efficiency is not directly correlated with the location inside a galaxy. However, the results we found showed that the surface star formation rate density changes with location, presenting higher levels in the arms of a galaxy compared to the inter-arm regions.

Field stars and the possible interaction between two galaxies

Many galaxies in the universe are isolated, some others have a companion with which they are interacting gravitationally. For example, the Milky Way is interacting with the Andromeda Galaxy. However, there are galaxies that, despite not showing a (visual) companion, present features that suggest the presence of a companion or an interaction with (an)other system(s). One of these special cases is the galaxy NGC 1313. We used the resolved stellar population of this galaxy and the possible satellite companion, to study the interaction between these two systems. In **Chapter 5** we found that the field stars in these galaxies suggest the possibility of an interaction, however, our results could not find a final answer due to observational uncertainties.

Throughout the studies made here, field stars and star clusters proved to be a powerful tool to understand galaxy formation and evolution. These two systems have unique and outstanding properties, and hold insightful information of long past and recent processes that shaped the galaxies as we see them today. Field stars and star clusters can guide to a better overview of galaxy formation and evolution, being used as fingerprints of a galaxy. However, a large effort still needs to be made.

Astronomers will always pursue for a full understanding of the processes that shape galaxies, and how these processes can be observed in a cosmological way, looking forward for their final objective, to understand the universe.

Nederlandse samenvatting

Vanaf het moment dat sterrenkundigen zich realiseerden dat de Melkweg slechts een van de vele sterrenstelsels in het heelal is, proberen ze te begrijpen hoe deze systemen zich gevormd hebben en hoe ze zich ontwikkelen. Dit is echter niet vanzelfsprekend. Om de vorming en ontwikkeling van sterrenstelsels te begrijpen, is het noodzakelijk om een beeld te hebben van hoe de verschillende delen van een sterrenstelsel samenhangen (zoals de sterren en het gas waaruit een sterrenstelsel is opgebouwd) en hoe hun interactie leidt tot de waarneembare eigenschappen waarmee ze gekarakteriseerd kunnen worden.

De structuur van spiraalsterrenstelsels werd in eerste instantie bestudeerd met behulp van de ruimtelijke verdeling van veldsterren en sterrenhopen in de Melkweg. Jonge veldsterren bleken zich in grote concentraties op te houden in de armen van de Melkweg. Waarnemingen van jonge sterrenhopen lieten zien dat ze zich in de schijf van het sterrenstelsel bevinden, terwijl de oude sterrenhopen verdeeld zijn buiten de schijf, in een halo rond de Melkweg. Het is echter zo dat onze plaats binnen de Melkweg ons ervan weerhoudt het gehele sterrenstelsel te bestuderen. Daarom worden ook sterrenstelsels buiten de Melkweg op een dergelijke manier bestudeerd.

Een groot deel van de onderzoeken naar de structuur en geschiedenis van sterrenstelsels hebben gebruik gemaakt van het geïntegreerde licht van sterpopulaties. In dit proefschrift kiezen we voor een nieuwe benadering, waarin de opgeloste sterpopulaties gebruikt worden om de verdeling van de sterren te relateren aan de verschillende eigenschappen van een sterrenstelsel. We doen tevens onderzoek naar sterrenhopen, die in combinatie met de opgeloste veldsterpopulaties leiden tot een beter begrip van de processen die sterrenstelsels hun vorm geven. Onze belangrijkste studieobjecten zijn spiraalsterrenstelsels. Een karakteristiek voorbeeld wordt gegeven in figuur B.1, waar een klein deel van de sterrenhemel in de richting van het Melkwegcentrum wordt getoond, met een aantal veldsterren verdeeld over de afbeelding. In dezelfde figuur wordt ook een sterrenhoop afgebeeld: de bolvormige sterrenhoop M13.

Het onderzoek naar opgeloste sterpopulaties in omgevingen buiten de Melkweg is mogelijk door onze kennis van de fysische processen die de ontwikkeling van sterren bepalen. Bepaalde eigenschappen van sterren kunnen gecombineerd en vergeleken in een diagram dat het kleur-helderheids diagram genoemd wordt (in het Engels 'color-magnitude diagram' en daarom 'CMD'). Het CMD wordt gebruikt om de verscheidene eigenschappen van sterpopulaties te identificeren, en is het

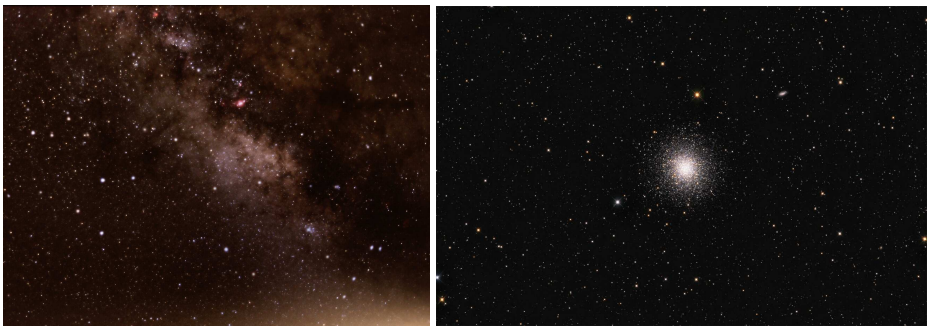

Figuur B.1: *Links*: Veldsterren in de richting van het Melkwegcentrum. Afbeelding: P. van der Haar. *Rechts*: Sterrenhoop M13. Afbeelding: Thomas V. Davis

belangrijkste middel dat in dit proefschrift gebruikt wordt om de eigenschappen van de veldsterren in de bestudeerde sterrenstelsels te bepalen. De kracht van deze methode komt voort uit de grote hoeveelheid informatie die verkregen kan worden wanneer waargenomen CMDs vergeleken worden met gemodelleerde CMDs – een methode die de *synthetische CMD methode* genoemd wordt.

Op een vergelijkbare manier stelt kennis van de ontwikkeling van sterrenhopen ons in staat om waargenomen sterrenhooppopulaties in sterrenstelsels te bestuderen. Om de eigenschappen van sterrenhopen te begrijpen, vergelijken we de waargenomen eigenschappen met theoretische modellen, die bekend staan als *eenvoudige sterpopulatie modellen* (Engels: 'simple stellar population models' of 'SSPs').

Zoals in het volgende wordt beschreven, is het gebruik van sterrenhopen en veldsterren een krachtige methode om een aantal verschillende waargenomen eigenschappen van spiraalsterrenstelsels te begrijpen. In dit proefschrift bestuderen we de nabije spiraalsterrenstelsels NGC 45, NGC 1313, NGC 4395, NGC 5236, en NGC 7793. De data waarop dit werk gebaseerd is, zijn verkregen met de *Hubble Space Telescope* (HST). Er is gebruik gemaakt van twee van de HST-detectoren: de Advanced Camera for Surveys en de Wide Field Planetary Camera 2, waarbij de optische golflengte-gebieden U, B, V en I gebruikt zijn.

Veldsterren en sterrenhopen als indicatoren van voorbije activiteit

Gedurende de afgelopen decennia hebben sterrenkundigen de gedachte gevolgd dat de meeste (zoniet alle) sterren in sterrenhopen geboren worden. Om die reden zijn sterrenhopen gebruikt om de vormingsgeschiedenis van sterrenstelsels te achterhalen. Het is mogelijk om veldsterren en sterrenhopen te gebruiken om te achterhalen hoe sterrenstelsels ontstaan zijn en hoe ze zich ontwikkelen, mits de meeste sterren inderdaad in sterrenhopen zijn gevormd. Om dit te verifiëren moe-

ten we de (mogelijke) samenhang tussen veldsterren en sterrenhopen achterhalen. **Hoofdstuk 2** en **Hoofdstuk 3** worden gewijd aan een studie van de opgeloste sterpopulaties en sterrenhopen in de vijf sterrenstelsels die in dit proefschrift bestudeerd worden. De resultaten laten zien dat de fractie van stervorming die resulteert in gravitationeel gebonden sterrenhopen minder dan 10% is. Onderzoek naar zeer jonge sterren in de Galactische omgeving van de zon toont aan dat een zekere fractie van de sterren inderdaad in (gebonden) sterrenhopen geboren wordt, terwijl andere sterren deel uit maken van de lage-dichtheid kant van een continue dichtheidsverdeling, waarin geen verschillende vormen van stervorming (i.e. veld of in sterrenhopen) gevonden zijn. Het is echter wel zo dat er een relatie bestaat tussen de hoeveelheid licht die uitgestraald wordt door (jonge) sterrenhopen en de fractie van stervorming die resulteert in gebonden sterrenhopen. Deze relatie varieert tussen verschillende sterrenstelsels. Dit suggereert dat er een onderliggend verband bestaat tussen een sterrenstelsel en zijn sterrenhopen.

Veldsterren en de armen van een spiraalsterrenstelsel

Spiraalsterrenstelsels zijn zeer opvallend door hun spectaculaire vormen. Tegen het eind van de jaren 50 werd ontdekt dat jonge sterren zich voornamelijk ophouden in de spiraalarmen van de Melkweg, wat suggereert dat de vorming van sterren sneller verloopt in spiraalarmen. Daarnaast tonen eerdere onderzoeken naar de ruimtelijke verdeling van sterrenhopen aan dat jonge sterrenhopen zich voornamelijk in de schijf van een sterrenstelsel bevinden, terwijl oude sterrenhopen verspreid zijn in een halo rond het sterrenstelsel. Dit duidt erop dat de stervormingsactiviteit groter is in de schijf dan erbuiten. Theoretische modellen van het eind van de jaren 60 lieten zien hoe het voortplantingpatroon van een dichtheidsgolf de spiraalstructuur in sterrenstelsels veroorzaakt. Door gebruik te maken van opgeloste sterpopulaties in het spiraalsterrenstelsel NGC 5236 (M83), bestuderen we in **Hoofdstuk 4** hoe de oppervlaktedichteid van stervorming samenhangt met de armen van spiraalsterrenstelsels. De theorie voorspelt dat stervorming wordt veroorzaakt door het samendrukken van het gas in een sterrenstelsel door een dichtheidsgolf. Eerdere onderzoeken hebben gesuggereerd dat de efficiëntie van het stervormingsproces niet gerelateerd is aan de locatie in een sterrenstelsel. Onze resultaten tonen echter aan dat de oppervlaktedichtheid van stervorming wel degelijk afhangt van de locatie, en hogere waarden heeft in de armen van een sterrenstelsel dan in de gebieden tussen de armen.

Veldsterren en de mogelijke interactie tussen twee sterrenstelsels

Veel sterrenstelsels in het heelal bestaan in isolatie, anderen hebben een begeleider waarmee zij gravitationeel interacteren. De Melkweg interacteert bijvoorbeeld

met het Andromedastelsel. Er zijn echter ook stelsels die geen (zichtbare) begeleider hebben, maar waarvan de eigenschappen wel duiden op de aanwezigheid van een begeleider of een interactie met (een) ander(e) syste(e)m(en). Een voorbeeld van een dergelijk sterrenstelsel is NGC 1313. We hebben gebruik gemaakt van de opgeloste sterpopulatie van dit sterrenstelsel en zijn mogelijke begeleider om de interactie tussen deze twee systemen te analyseren. In **Hoofdstuk 5** tonen we aan dat de veldsterren in deze sterrenstelsels de mogelijkheid van interactie suggereren, maar onze resultaten bieden geen definitief antwoord vanwege observationele onzekerheden.

In dit onderzoek komen veldsterren en sterrenhopen naar voren als krachtige middelen om de vorming en evolutie van sterrenstelsels te begrijpen. Deze twee systemen hebben unieke en opvallende eigenschappen, en bevatten inzichtelijke informatie over de lang voorbije en recente processen die de sterrenstelsels gevormd hebben tot hoe wij hen vandaag de dag zien. Veldsterren en sterrenhopen kunnen helpen om een beter overzicht van de vorming en evolutie van sterrenstelsels te krijgen, door hen te gebruiken als de vingerafdrukken van a sterrenstelsel. Hiervoor is het echter nog steeds nodig om veel werk te verzetten.

Astronomen zullen altijd een volledig begrip najagen van de processen die sterrenstelsels vormen, en hoe deze processen op een kosmologische manier kunnen worden waargenomen, terwijl ze uit kijken naar hun uiteindelijke doel - om het heelal te begrijpen.

Resumen en Español

Desde el momento en que los astrónomos observaron que la Vía Láctea era una galaxia entre otras muchas, hemos intentado entender como estos sistemas particulares se formaron y como fue su evolución. Sin embargo, ésta no es una tarea fácil. Para entender la formación y evolución de las galaxias, necesitamos entender cómo las diferentes partes están relacionadas (por ejemplo las estrellas y el gas que componen la galaxia) y cómo su interacción conlleva a observar las propiedades que las caracterizan.

La estructura de las galaxias espirales empezó a ser estudiada usando la distribución de las estrellas de campo y de los cúmulos estelares en la Vía Láctea. Estrellas jóvenes del campo aparecen concentradas en los brazos de la galaxia. Observaciones de cúmulos de estrellas muestran que los cúmulos jóvenes están localizados en el disco de la galaxia, mientras que los cumulos viejos estan distribuidos fuera del disco, en el halo de la galaxia. Pero nuestra ubicación en el disco de la galaxia evita que podamos tener un estudio completo sobre la Vía Láctea. Por esta razón, realizamos estos estudios en otras galaxias.

En general, los estudios de la estructura y la actividad pasada de las galalxias ha sido llevado a cabo integrando (sumando) el total de la luz de la población estelar. Como un nuevo acercamiento al problema, haremos uso de la población de estrellas resueltas individualmente para estudiar cómo su distribución está relacionada con diferentes parámetros de la galaxia. Presentaremos además estudios de cúmulos de estrellas, los cuales combinados con la población de estrellas resueltas, aumentará nuestro entendimiento sobre los procesos que dan forma a las galaxias, para nuestro caso, las galaxias espirales. Como un ejemplo ilustrativo, la Fig. C.1 muestra un pequeño campo de estrellas en la dirección del centro de la Vía Láctea, donde se puede observar un número de estrellas de campo distribuidas sobre la imagen. En la misma figura se muestra un cúmulo de estrellas, el cúmulo globular M13.

El estudio de la población de estrellas en entornos extragalácticos puede ser realizado gracias al conocimiento sobre los procesos físicos que gobiernan la evolución estelar. Algunas propiedades pueden ser combinadas y observadas en un diagrama llamado Diagrama Color-Magnitud (CMD, por sus siglas en inglés). El CMD indica diferentes propiedades de las poblaciones estelares, y es la herramienta principal usada aquí para entender los diferentes aspectos de las estrellas de campo en las galaxias estudidas. El poder de esta herramienta proviene de la gran cantidad de

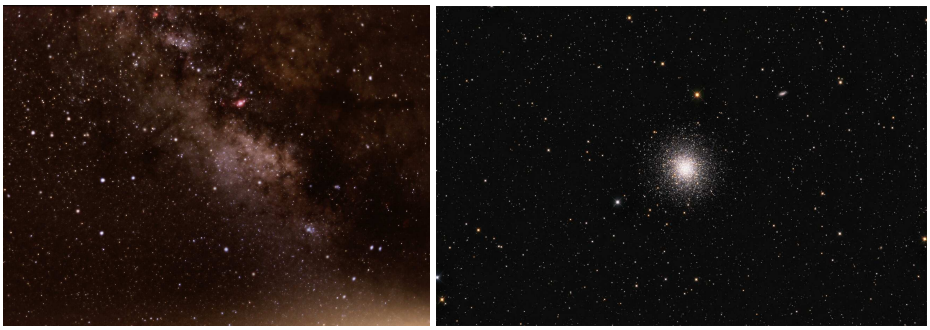

Figura C.1: *Panel izquierdo*: Estrellas de campo en la dirección del centro de la Vía Láctea. Créditos: P. van der Haar. *Panel derecho*: Cúmulo estelar M13. Créditos: Thomas V. Davis

información que puede ser obtenida cuando el CMD observado es comparado con un CMD teórico, a través de un método llamado *The synthetic CMD method*.

De una manera semejante, el conocimiento sobre la evolución de cúmulos estelares nos permite hacer un estudio de la población de cúmulos en las galaxias. Para entender y estudiar las propiedades de los cúmulos estelares, comparamos las propiedades observadas de los cúmulos con modelos teóricos, conocidos como *Simple Stellar Population models*.

Como será descrito más adelante, el uso de los cúmulos estelares y las estrellas de campo serán una poderosa herramienta para entender diferentes propiedades de las galaxias analizadas. Estudiaremos las galaxias espirales NGC 45, NGC 1313, NGC 4395, NGC 5236, y NGC 7793 ubicadas en el universo cercano. Las imágenes usadas en este trabajo fueron tomadas con el *Telescopio Espacial Hubble* (HST, por sus siglas en inglés). Dos de sus detectores fueron usados, la Advanced Camera for Surveys y la Wide Field Planetary Camera 2, cubriendo las longitudes de ondas en el optico U, B, V e I.

Estrellas de campo y los cúmulos como indicadores de actividad en el pasado

Durante las últimas décadas, los astrónomos han seguido la idea que la mayoría (si no todas) las estrellas se forman en cúmulos. Por esta razón, los cúmulos de estrellas han sido usados para reconstruir la historia de la formación de las galaxias. Para ese propósito necesitamos encontrar las (posibles) correlaciones entre las estrellas de campo y los cúmulos estelares. El **Capítulo 2** y el **Capítulo 3** están dedicados al estudio de las poblaciones de estrellas de campo y los cúmulos estelares en las cinco galaxias estudiadas en esta tesis. Los resultados mostraron que la fracción de estellas formadas que terminan en cúmulos es menor del 10 %. Estudios de objetos estelares jóvenes en el vecindario solar indican que una fracción de estrellas de hecho se forma

en cúmulos, mientras que la otra fracción no es más que el límite inferior de una función de distribución logarítmica, donde no hay diferentes modos de formación de estrellas (i.e. individual o en cúmulo). Sin embargo, se encontró una relación entre la cantidad de luz que llega de los cúmulos (jóvenes) y la fracción de estrellas que se forma en cúmulos, mostrando cambios en diferentes ambientes, i.e. en diferentes galaxias. Esto sugiere una correlación subyacente entre la galaxia y los cúmulos de esa galaxia.

Estrellas de campo y los brazos de una galaxia espiral

Las galaxias espirales siempre han llamado la atención debido a su espectacular estructura. A finales de los años 50, estudios mostraron que las estrellas jóvenes estaban concentradas en uno de los brazos de la Vía Láctea, sugiriendo que la formación de estrellas podría ser más intensa en los brazos. Además, previos estudios de la disrtibución espacial de cúmulos estelares mostraron que los cúmulos jóvenes estaban preferencialmente ubicados en el disco de la galaxia, mientras que los cúmulos viejos estaban en el halo, indicando mayor actividad en el disco. Modelos teóricos a finales de los años 60 lograron explicar como la propagación de una onda de densidad podía reproducir la estructura espiral observada en galaxias. Usando la población de estrellas de campo en la galaxia NGC 5236 (M83) estudiamos en el **Capítulo 4** como la densidad superficial de la rata de formación estelar está conectada con los brazos de las galaxias espirales. Desde un punto de vista teórico, es de esperarse que cuando una onda de densidad se encuentre con el gas de la galaxia, la formación de estrellas sea incrementada debido a la compresión del gas. Previos estudios sugirieron que la eficiencia con la que se forman estrellas no estaba relacionada con la ubicación dentro de la galaxia. Sin embargo, el resultado encontrado por nosotros mostró que la densidad superficial de la rata de formación estelar cambia con la ubicación, presentando niveles más elevados en los brazos en comparación con las regiones intermedias de los brazos.

Estrellas de campo y la posible interacción entre dos galaxias

Muchas galaxias en el universo están aisladas, otras presentan una compañera que está interactuando gravitacionalmente. La Vía Láctea, por ejemplo, esta interactuando con la galaxia de Andrómeda. Sin embargo, hay galaxias que, a pesar de no mostrar una compañera (visualmente), presentan características que sugieren la presencia de una compañera, o una interacción con algún (otro) sistema(s). Uno de estos casos especiales es la galaxia NGC 1313. Usando la población de estrellas de campo de esta galaxia y de la posible galaxia satélite, estudiamos la interacción entre estos dos sistemas. En el **Capítulo 5** encontramos que las estrellas de campo en estas dos galaxias sugieren la posibilidad de una interacción, sin embargo, nuestros resulta-

dos no pudieron dar una respuesta final debido a las incertidumbres observacionales.

A traves de los estudios realizados acá, las estrellas de campo y los cúmulos estelares mostraron ser una herramienta poderosa para entender la formación y evolucion de las galaxias. Estos dos sistemas tiene propiedades únicas y excepcionales, y guardan información detallada de procesos pasados y recientes que dan forma a las galaxias de la manera que las observamos hoy. Las estrellas de campo y los cúmulos estelares pueden servir de guía para tener una mejor visión sobre la formacion y la evolución de galaxias, siendo usados como huellas dactilares de éstas. Sin embargo, un gran esfuerzo es todavía necesario.

Los astrónomos siempre perseguirán un entendimiento total de los procesos que dan forma a las galaxias, y cómo estos procesos pueden ser observados de manera cosmológica, buscando siempre por su objetivo final, entender el universo.

Acknowledgments - Agradecimientos

Lets star stating that life has been more than good with me. I moved from far away, another continent(!), and still I feel like at home. And it is not because my family and friends from Colombia are here with me. It is easier than that, my friends here are not only friends, they became my family. Good and bad moments, they have been always there for me, either to shout at me, or to comfort me. Loneliness is the complete opposite of what I have felt during the last four years.

First of all, I want to thank my mentors throughout all the time I have been working in astronomy. In chronological order of appearance: Dr. Jorge Zuluaga. Parce, desde el principio siempre nos has apoyado, siempre has impulsado el que hagamos astronomia, y ademas has sido un gran amigo. Dr. Marco Sirianni, you invited me to work with you at STScI, twice. I learned a lot during my time there, and I think that working with you is what brought me to Utrecht to start my Ph.D. Dr. Søren Larsen, you have taken me through an amazing project, always making me be careful and wonder how to improve my work in many different ways. To Prof. Henny Lamers and Prof. Chrisptoh Keller I want to extend my acknowledgments, you are also mentors in this long way. I will include in this list another person, Dr. David Ardila. Profe David, creo que desde el primer momento, nos cojiste, nos diste una patada, y nos pusiste a hacer astronomia, empujandonos (a Juan y a mi) hacia Baltimore, y de ahi en adelane, cuidandonos como a niños chiquitos. I want to thank also the reading committee of my thesis Prof. Lamers, Prof. Portegies-Zwart, Prof. Kroupa, Prof. Östlin, and Dr. Bastian for the nice comments and the time to review my thesis.

It has been a pleasure to be part of the Star Clusters group here in Utrecht. I would like to acknowledge them for the interesting discussions, the travels and the drinks/laughs we did together. In no special order: Renier, Nick, Steven, Gregal, Jorien, Peter, Remco, and Elizabeth. Special thanks to my collaborators Dr. Nate Bastian, Dr. Mark Gieles and Dr. Angela Adamo, it has been a pleasure to work with you, and I hope we can keep going in that direction.

At the Utrecht University, where I have been working for the past four years, I have met many people that, in one way or another, have influenced me. In no special

order: Carlo, Helena, Sjorse, Alex, Joke, Andrei, Sander, Tim, Bob, Eveline, Jorit, Dasha, Frans, Sabina, Matteo, Catherine, Sandra, Frank, Bram, Maureen, Jaco, Onno. I want to extend a special acknowledgement to some people: Axel (fuiste el primero con el que pude hablar español a mi llegada y fueron muchos los momentos donde se puedo hablar mierda), Selma (tons and tons of dancing, travels, caipirinhas and laughs), Klara (for all the coffee times and the english corrections), Martijn (for all the laughs and insightful comments), Maria (sabes que si, y por siempre), Nikola (for all the great moments and discussions, all the drinking moments and the vegetarian dinners). Also, I want to express my gratitude to Marion, Sake and Ed, you were always helpful.

During the past four years I spend most of the time at my office. I want to dedicate this paragraph to thank my two office-mates: Ana Chies Santos and Diederijk Kruijssen. I learned a lot from both of you, not just scientifically speaking, but as a person, you are good friends. The time at the office was always very nice, and we were able to talk about everything. We also traveled to conferences and schools, and it was always a pleasure for me to have you there.

Este parrafo esta dedicado pa un amigo que llevo siempre conmigo, aunque nos veamos poquito: Juan Rafael Martinez Galarza. Por tu culpa (desgraciado!) es que me meti en este lio de 4 años, por vos es que termine haciendo una tesis doctoral en Holanda, algo que nunca se me hubiera ocurrido, y que claramente nunca olvidare. Por eso y cien mil cosas mas, parcero, muchisimas gracias.

And for the last, I want to thank my family. Even if is just one family in my heart, I will make three groups here:

- *Familia Europa/Colombia*. Parce, a todos los he llevado siempre en el corazón. Con todos he tratado de compartir algun momento de mi estadia por estos lados. A todos he podido dedicarles un poquito de tiempo, bien pa que nos desahoguemos, pa que nos riamos, pa que nos tomemos una polita, o pasiemos, o pa pasar una navidad y/o un año nuevo, un cumpleaños, o un simple chiste. A todos uds, mil gracias por todos los momentos, las risas, y por hacer parte de todos estos 4 años: Pili, Ana, Apaito, Sone, Gego, Maximo, Paula, Parra, Jaime F, Elena, Alejo, Ricardo, Juan Serna. Unos agradecimientos iran especialmente para dos personas con las que tuve contacto todo este tiempo y que me ayudaron en demasiadas cosas, no solo laborales, siempre estubieron ahi como amigos: Clara y Juank.

- *Utrecht Family*. Four years with me, I can imagine is not easy at all! Since I arrived you have been there, with me, no matter what I have done, smart or stupid, you were there for/with me. I can not imagine have been here with better people than you. Thanks for all the moments, for 'hit' me when needed, for make me laugh. Arjen, I think that, more than a friend, I consider you a brother (also a wife eh!), more than that is hard to say. Hector, parce, que seria de mi vida en Utrecht sin vos? No me la imagino, ejta'n mi corazón! Javi, parce, aunque suene raro, siempre te he tenido como mi polo a tierra, y no sabes que tan agradecido estoy por eso, sos el que me hace parar y pensar,

parce tambien estas en mi corazón por siempre! You three guys are the best! Monica y Juan, creo que, siendo un poquito pretencioso y hablando en nombre de mucha gente, Utrecht no es la misma ciudad si uds no estan aca. Siempre con una sonrisa, siempre dispuestos a dar un consejo, a ayudar. Parceros, no se ni como darles gracias por todo, los llevare siempre en mi corazón, y espero que nos veamos muchas mas veces en el futuro. Aunque no estuvo en Utrecht por largo tiempo, alguien mas dejo marca, y sigue siendo alguien que considero de mi familia. German, parce, han sido muchos los momentos, las risas, las discusiones, demasiadas cosas. Para vos, unos agradecimientos muy especiales, y que no te quepa la menor duda de que siempre estaras en mi corazón. The rest of my Utrecht family are the people that always shared with me a lot, for the good and for the bad, beers, travels, movies, dinners, everything: Sylvia, Ana Alastruey, Catalina, Belen, Vica, Clarisa, Valentina, Ele, Illaria, Elif, Dani, Jessica, Bea, Victor, Helen, Paola, Emma. But there is also some people that is not from Utrecht per se, however, have been there and shared with me as well, so here are some special thanks to Caro legui and Tamara.

- *Familia Colombia*. Espero que nunca hayan pensado que los deje y me fui. De hecho, simplemente quise salir y convertirme en una mejor persona, para que siempre estuvieran orgullosos, y espero haberlo logrado. A ninguno de los aqui mencionados les dire que los llevo en mi corazón, lo considero redundante. Pito y Uva, nunca habra tiempo suficiente en el universo pa agradecerlos por todo, el amor, las enseñanzas, los consejos, los castigos, todo. Sara, Santiago, Teresita y Tia, nunca hubo una queja del por que me fui, por el contrario siempre era una pregunta sobre el sitio, la gente, mi trabajo, mi salud, siempre fue apoyo, incondicional, no puedo pedirles nada mas en absoluto. A mis tios y mis primos, que siempre una palabra de aliento tuvieron. Y a mis amigos del alma: Andrew, Esteban y Cata, que de igual manera siempre se preocuparon, apoyaron, estuvieron ahi cuando me hizo falta un consejo o alguien con quien hablar, a cualquier hora, siempre los senti cerquita, aunque la distancia sea tan grande. A todos uds, que tanta falta me han hecho durante todo este tiempo, y con los cuales creci y he compartido tantas experiencias, unos agradecimientos infinitos, desde lo mas profundo de mi corazón.

I am sure I am forgetting people here, but don't take me wrong, it has been 4 years, and I am more than grateful with every single one of you.

Para todos uds, mi familia, dedico esta tesis. For all of you, my family, I dedicate this thesis.

"I have never met a man/woman so ignorant
that I couldn't learn something from him/her."
Galileo Galilei
Italian astronomer & physicist (1564 - 1642)

Curriculum vitae

Born in Medellín, Colombia, in 1979. In 2007 I finished my bachelor in Theoretical Physics at the University of Antioquia, in Colombia. My thesis research, entitled *'Determination of the IMF in the LMC stellar clusters NGC 2156'* received an special mention and was published on a refereed journal. Since 2007 I have been doing my Ph.D. in Astrophysics at the Utrecht university, in The Netherlands. My main interest has been always focused to understand stellar populations and star clusters, and their relation with galaxy formation and evolution. For that reason, I have been working with my supervisor Dr. Søren Larsen on the project *'Tracing galaxy evolution through resolved stellar populations and star clusters'*. The work done during the last four years as a Ph.D. student have been presented in national and international conferences and schools, with poster and oral presentations, and has been published in refereed journals.